

AD-A196 683

UNCLASSIFIED

SECURITY CLASSIFICATION OF THIS PAGE (When Data Entered)

DTIC FILE COPY
1

REPORT DOCUMENTATION PAGE		READ INSTRUCTIONS BEFORE COMPLETING FORM
1. REPORT NUMBER AFIT/CI/NR 88- 24	2. GOVT ACCESSION NO.	3. RECIPIENT'S CATALOG NUMBER
4. TITLE (and Subtitle) A TIME-DEPENDENT MODEL FOR THE LOW-LATITUDE IONOSPHERE		5. TYPE OF REPORT & PERIOD COVERED MS THESIS
7. AUTHOR(s) GARY DOUGLAS WELLS		6. PERFORMING ORG. REPORT NUMBER
9. PERFORMING ORGANIZATION NAME AND ADDRESS AFIT STUDENT AT: UTAH STATE UNIVERSITY		10. PROGRAM ELEMENT, PROJECT, TASK AREA & WORK UNIT NUMBERS
11. CONTROLLING OFFICE NAME AND ADDRESS		12. REPORT DATE 1988
		13. NUMBER OF PAGES 110
14. MONITORING AGENCY NAME & ADDRESS(if different from Controlling Office) AFIT/NR Wright-Patterson AFB OH 45433-6583		15. SECURITY CLASS. (of this report) UNCLASSIFIED
		15a. DECLASSIFICATION/DOWNGRADING SCHEDULE
16. DISTRIBUTION STATEMENT (of this Report) DISTRIBUTED UNLIMITED: APPROVED FOR PUBLIC RELEASE		
17. DISTRIBUTION STATEMENT (of the abstract entered in Block 20, If different from Report) SAME AS REPORT		
18. SUPPLEMENTARY NOTES Approved for Public Release: IAW AFR 190-1 LYNN E. WOLAYER Dean for Research and Professional Development Air Force Institute of Technology Wright-Patterson AFB OH 45433-6583		
19. KEY WORDS (Continue on reverse side if necessary and identify by block number)		
20. ABSTRACT (Continue on reverse side if necessary and identify by block number) ATTACHED		

DTIC
ELECTE
AUG 04 1988
S D
AD

A TIME-DEPENDENT MODEL FOR THE
LOW-LATITUDE IONOSPHERE

by

Gary Dougias Wells

A thesis submitted in partial fulfillment
of the requirements for the degree
of
MASTER OF SCIENCE
in
Soil Science and Biometeorology

Approved:

Robert W. Schubert
Major Professor
W. J. Raith
Committee Member

Laurence S. Hyppaz
Committee Member
Lawrence T. Pelle
Dean of Graduate Studies

UTAH STATE UNIVERSITY
Logan, Utah

1988

ACKNOWLEDGEMENTS

With deep gratitude, I would like to thank Dr. Robert W. Schunk for his patience and guidance in keeping me on the right track in my research efforts, and for sharing his abundant experience in ionospheric modelling. He was a source of inspiration and insight.

Special thanks to Ms. Jean Selzer and Ms. Sherry Thompson for putting up with my incessant questions and helping me put this thesis together.

Deepest appreciation goes to my wife, Tena, for her endless faith and encouragement without which I could not have continued; and to Chris and Haley for their support.

I would also like to collectively thank the Soil Science and Biometeorology Department, the Center for Atmospheric and Space Sciences, and the other AFIT students for their support and friendship.

Gary D. Wells

Accession For	
NTIS GRAAI	<input checked="" type="checkbox"/>
DTIC TAB	<input type="checkbox"/>
UNCLASSIFIED	<input type="checkbox"/>
STANDARD FORM	
By	
DRAFTED	
REVIEWED	
APPROVED	
DISTRIBUTION STATEMENT	
DRAFT	
DRAFT	
A-1	



TABLE OF CONTENTS

	Page
ACKNOWLEDGEMENTS	ii
LIST OF TABLES	iv
LIST OF FIGURES	v
ABSTRACT	vi
Chapter	
I. INTRODUCTION	1
The Terrestrial Equatorial Ionosphere	1
Historical Development	4
Model and Assumptions	10
II. CONTINUITY AND MOMENTUM EQUATIONS	14
An Orthogonal, Curvilinear Coordinate System	14
Transport Equations	15
Atmospheric Chemistry	16
Momentum Equation	19
Continuity Equation	21
III. ENERGY EQUATIONS FOR O ⁺ , H ⁺ , AND ELECTRONS	31
IV. RESULTS AND DISCUSSION	42
Boundary Conditions	42
Inputs	43
Results	45
V. SUMMARY AND CONCLUSIONS	65
REFERENCES	71
APPENDICES	75
Appendix A: Neutral Wind Model	76
Appendix B: An Empirical Model of the Magnetic Field	87
Appendix C: An Empirical Model of Electric Fields at Low Latitudes	88
Appendix D: A Comparison of the IRI, Chiu, and SLIM Models	97
Appendix E: Permission Letters	100

LIST OF TABLES

Table	Page
1. Zonal Neutral Wind Speeds for Equinox and Solar Maximum Conditions	78
2. Meridional Neutral Wind Speeds for Equinox and Solar Maximum Conditions	78
3. Zonal Neutral Wind Speeds for Winter Solstice and Solar Maximum Conditions	79
4. Zonal Neutral Wind Speeds for Winter Solstice and Solar Maximum Conditions	79
5. Zonal Neutral Wind Speeds for Winter Solstice and Solar Minimum Conditions	80
6. Meridional Neutral Wind Speeds for Winter Solstice and Solar Minimum Conditions	80

LIST OF FIGURES

Figure	Page
1. Schematic representation of interhemispheric plasma flow along geomagnetic field lines crossing the equator at plasmaspheric altitudes for solstice conditions	2
2. A schematic representation showing the vertical drift of the ionospheric plasma (W) due to a horizontal neutral wind along a magnetic meridian (U_θ)	3
3. A schematic illustration of the heights and densities of the various ionospheric regions	3
4. An illustration of the processes leading to the formation of the Appleton peaks in the daytime F -region at equatorial latitudes	4
5. A diagram showing the variation of q along a magnetic field line that crosses the equator at 3000 km altitude	15
6. Results from the MSIS86 empirical model for a dipole field line with an equatorial crossing altitude of 1000 km	44
7. Dipole field lines with equatorial crossing altitudes of 1000 km and 3000 km	45
8. Plasma (a) densities and (b) temperatures along a magnetic field line with an equatorial crossing altitude of 1000 km for equinox and solar minimum conditions and 0° magnetic longitude	47
9. Plasma (a) densities and (b) temperatures along a magnetic field line with an equatorial crossing altitude of 1000 km for solstice and solar minimum conditions and 0° magnetic longitude	50
10. Plasma (a) densities and (b) temperatures along a magnetic field line with an equatorial crossing altitude of 1000 km for equinox and solar minimum conditions and 0° magnetic longitude. Electrodynamic effects are included	52
11. Plasma (a) densities and (b) temperatures along a magnetic field line with an equatorial crossing altitude of 1000 km for solstice and solar minimum conditions and 0° magnetic longitude. Electrodynamic drifts included	54

12.	Plasma (a) densities and (b) temperatures along a magnetic field line with an equatorial crossing altitude of 3000 km for equinox and solar minimum conditions and 0° magnetic longitude	56
13.	Plasma (a) densities and (b) temperatures along a magnetic field line with an equatorial crossing altitude of 3000 km for solstice and solar minimum conditions and 0° magnetic longitude	59
14.	Plasma (a) densities and (b) temperatures along a magnetic field line with an equatorial crossing altitude of 3000 km for solstice and solar maximum conditions and 0° magnetic longitude	61
15.	Plasma densities along a magnetic field line with an equatorial crossing altitude of 3000 km for solstice and solar minimum conditions and 0° magnetic longitude. Neutral wind effects are included	63
16.	Meridional component of the neutral winds in meters/second along a magnetic field line. The winds are valid for 97°E magnetic longitude, equinox, solar maximum, and midnight local time	82
17.	Meridional component of the neutral winds in meters/second along a magnetic field line. The winds are valid for 97°E magnetic longitude, equinox, solar maximum, and 1200 LT	82
18.	Meridional component of the neutral winds in meters/second along a magnetic field line. The winds are valid for 179.8°E magnetic longitude, equinox, solar maximum, and midnight local time	83
19.	Meridional component of the neutral winds in meters/second along a magnetic field line. The winds are valid for 97°E magnetic longitude, June solstice, solar maximum, and midnight local time	83
20.	Meridional component of the neutral winds in meters/second along a magnetic field line. The winds are valid for 97°E magnetic longitude, June solstice, solar maximum, and 1200 LT	85
21.	Meridional component of the neutral winds in meters/second along a magnetic field line. The winds are valid for 179.8°E magnetic longitude, June solstice, solar maximum, and midnight local time	85

22.	Meridional component of the neutral winds in meters/second along a magnetic field line. The winds are valid for 358.6°E magnetic longitude, June solstice, solar maximum, and midnight local time	86
23.	Global magnetic field strengths from FIELDG for 200 km.	87
24.	Schematic representation of how the variation of pseudopotential with colatitude is determined for any point, P, along the magnetic field line	90
25.	Vertical component of the electrodynamic winds in meters/second at 300 km for equinox and 0° magnetic longitude as a function of magnetic latitude and universal time	91
26.	Vertical component of the electrodynamic winds in meters/second at 1000 km for equinox and 0° magnetic longitude as a function of magnetic latitude and universal time	91
27.	Vertical component of the electrodynamic winds in meters/second at 300 km for June solstice and 0° magnetic longitude as a function of magnetic latitude and universal time	93
28.	Vertical component of the electrodynamic winds in meters/second at 1000 km for June solstice and 0° magnetic longitude as a function of magnetic latitude and universal time	93
29.	Azimuthal component of the electrodynamic winds in meters/second at 300 km for equinox and 0° magnetic longitude as a function of magnetic latitude and universal time	94
30.	Azimuthal component of the electrodynamic winds in meters/second at 1000 km for equinox and 0° magnetic longitude as a function of magnetic latitude and universal time	94
31.	Azimuthal component of the electrodynamic winds in meters/second at 300 km for June solstice and 0° magnetic longitude as a function of magnetic latitude and universal time	96
32.	Azimuthal component of the electrodynamic winds in meters/second at 1000 km for June solstice and 0° magnetic longitude as a function of magnetic latitude and universal time	96
33.	A comparison of electron density profiles produced by the SLIM, Chiu, and IRI empirical models for 0° dip latitude and 324°E magnetic longitude for equinox and moderate solar activity	98
34.	A comparison of electron density profiles produced by the SLIM, Chiu, and IRI empirical models for 14° dip latitude and 324°E magnetic longitude for equinox and moderate solar activity	99

ABSTRACT

A Time-Dependent Model for the Low-Latitude Ionosphere

by

Gary D. Wells, Master of Science
Utah State University, 1988

Major Professor: Dr. Robert W. Schunk

Department: Soil Science and Biometeorology

The theoretical development of a time-dependent, self-consistent model of the low-latitude ionosphere between 200 and 3000 km is presented. This model solves the coupled continuity-momentum and energy equations for an ionosphere composed of two ion species (O^+ and H^+) and electrons in a quasi-simultaneous manner. Account is taken of effects due to the curvature of the field lines and the inclination of the field line to the vertical. This model allows for electrodynamic drift of the plasma during the day, effects due to the expansion and contraction of the neutral atmosphere, and ion-neutral drag effects, as well as the transfer of momentum through collisions. The energy equation allows for heating or cooling through collisions, conduction parallel to B , frictional heating/cooling due to the relative motion between the ions and the neutrals, and effects due to adiabatic expansion and contraction.

We have significantly improved modelling capabilities by including more realistic neutral winds and electric fields. We have also allowed for the offset in the geographic and geomagnetic poles by mapping the neutral winds and time (both organized in the geographic coordinate system) into the magnetic reference frame. By mapping the neutral winds into the magnetic coordinate system,

longitudinal variations in the density and temperature of the *F*-region are introduced in a consistent manner. The net result is a model that has applicability for a variety of local times, seasons, longitudes, and altitudes.

Results from this model are shown to reproduce the important physical processes that are unique to the low-latitude ionosphere, such as the depletion of plasma at the magnetic equator due to electrodynamic drifts and diffusion, and the seasonal anomaly.

(110 pages)

CHAPTER I

INTRODUCTION

The Terrestrial Equatorial Ionosphere

The terrestrial ionosphere is that portion of the earth's upper atmosphere in which ions and free electrons exist in significant numbers. This is not to say that ion densities exceed the neutral densities throughout the ionosphere for in the lowest regions of the ionosphere, the neutral concentration is still many orders of magnitude greater than the ion concentration. In fact, ion densities generally do not exceed neutral densities below 1000 km for moderate solar activity.

The upper extent of the ionosphere is often referred to as the plasmasphere. The plasmasphere is a torus-shaped region which encircles the earth at low and middle latitudes. It is composed of a cold, relatively dense plasma of ionospheric origin which corotates with the earth. In addition to corotating, the plasma can flow between conjugate hemispheres as depicted in Figure 1. The plasmasphere has a maximum vertical extent of 4 earth radii (R_E) at the equator. At even greater heights, a transition from plasmaspheric to the magnetospheric plasma occurs. This transition is called the plasmapause and is marked by a large decrease in electron density [Schunk, 1983]. Young *et al.*, [1979, 1980] and Richards *et al.* [1983] have developed time-dependent models valid for plasmaspheric field lines, along which the important variations are in the vertical direction. This makes this region somewhat easier to model than the lower ionosphere, where variations in the horizontal and the vertical are important [Schunk, 1988].

Our region of interest will be the low-latitude ionosphere where some unique transport effects occur due to the near horizontal nature of the field lines. The first effect is due to thermospheric winds blowing from the summer to winter hemisphere. These winds induce a drift in the ionospheric plasma; and since the ions and electrons are bound to the magnetic field lines, this drift is field-

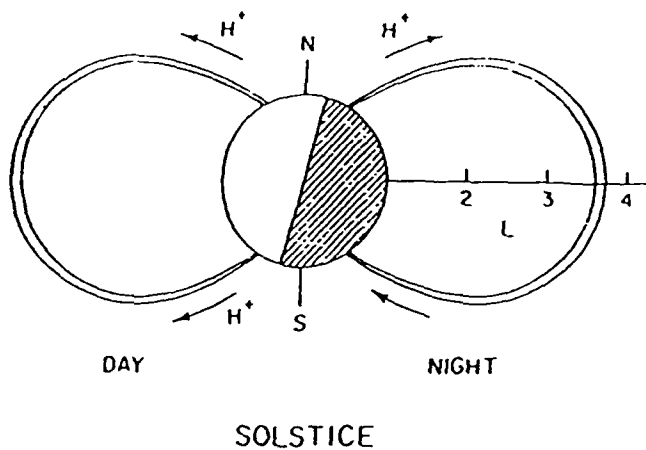


Figure 1. Schematic representation of interhemispheric plasma flow along geomagnetic field lines crossing the equator at plasmaspheric altitudes for solstice conditions (from *Evans and Holt, [1978]*). Reprinted by permission of D. Reidel Publishing Company.

aligned (This effect is shown schematically in Figure 2). As the plasma rises in the summer hemisphere, it expands and cools adiabatically; and, conversely, as it descends in the winter hemisphere, it is compressed and warmed.

Another feature is the equatorial fountain or Appleton anomaly which forms during the day on both sides of the magnetic equator. This feature consists of two peaks in the latitudinal profile of electron density centered on either side of the magnetic equator, and a "trough" in the electron density at the magnetic equator. In the day time *E*-region, thermospheric winds induce ionospheric currents, which induce an eastward electric field in the *F* region (See Figure 3 for the approximate altitudes of the various ionospheric regions). The combination of this eastward electric field and a northward magnetic field produces an upward drift of the plasma (ions and electrons) at the magnetic equator. As the plasma is being lifted, it is acted on by gravity, which causes it to drift away

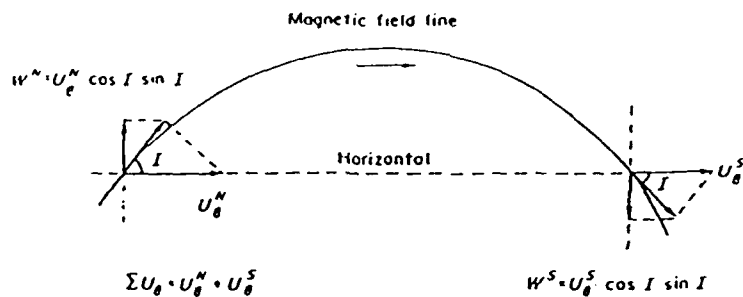


Figure 2. A schematic representation showing the vertical drift of the ionospheric plasma (W) due to a horizontal neutral wind along a magnetic meridian (U_θ). The inclination of the magnetic field to the horizontal is defined as I (from *Bittencourt and Sahai, [1978]*). Reprinted by permission of D. Reidel Publishing Company.

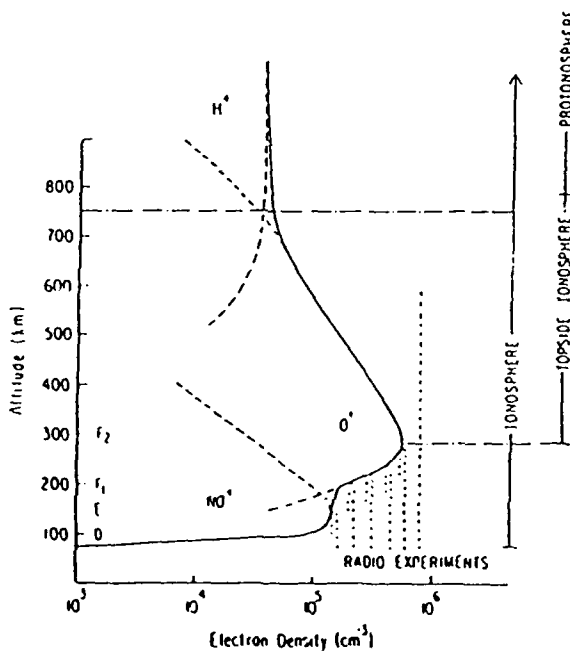


Figure 3. A schematic illustration of the heights and densities of the various ionospheric regions (from *Banks et al., [1976]*). Reprinted by permission of D. Reidel Publishing Company.

from the magnetic equator and diffuse down the magnetic field lines forming the regions of enhanced plasma density at $\pm 15^{\circ}$ magnetic latitude and depleting the plasma density at the magnetic equator. This process is shown in Figure 4.

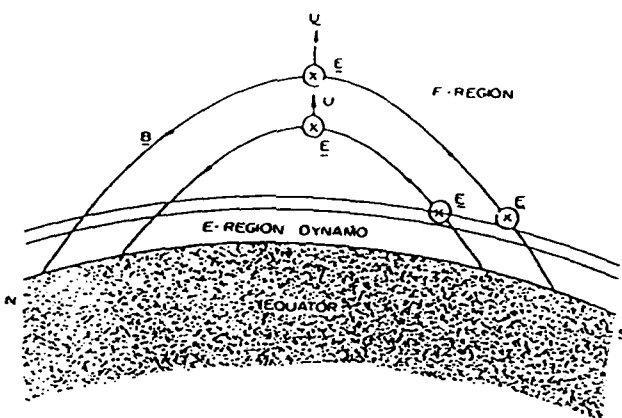


Figure 4. An illustration of the processes leading to the formation of the Appleton peaks in the daytime *F*-region at equatorial latitudes (from Schunk, [1983]). Reprinted by permission of D. Reidel Publishing Company.

Historical Development

Determination of the important factors controlling the formation, maintenance, and variation of the *F*-region and the topside ionosphere have resulted in the development of a number of theoretical models over the last 24 years. The decade of the 1960's was a period in which the primary focus was on establishing those processes which control the behavior of the *F*-region. Diffusion, while an important process in this region, was shown to be unable to account for the formation of the equatorial anomaly, the maintenance of the ionosphere at night, and the seasonal anomaly [Rishbeth *et al.*, 1963; Rishbeth, 1964, 1966]

even when the diurnal expansion and contraction of the neutral atmosphere and the ionosphere were taken into account [*Thomas*, 1966; *Thomas and Venables*, 1967; *Rishbeth*, 1964]. Their results did show that the peak in the *F*-region formed at the altitude where diffusion is balanced by photochemical loss, that diffusion was the dominant process above the *F*₂ peak, and that photochemistry was dominant below the *F*₂ peak [*Rishbeth et al.*, 1963]. Variations in the temperature were found to affect ion densities and the maximum height of the *F*₂-region [*Thomas and Venables*, 1967]; however, thermal expansion and contraction of the neutral atmosphere has little effect on ion densities during the day or night [*Schunk and Walker*, 1973].

In the early 1960's, the presence of an electric field within the *F*-region had yet to be confirmed – but was thought to exist – [*Bramley and Peart*, 1965] and some of the diffusion models being developed assumed the magnetic field lines were approximately vertical. *Baxter* [1964, 1967], *Sterling et al.* [1969], and *Kendall* [1962] were largely responsible for developing the appropriate equations and diffusion coefficients allowing for calculations along magnetic field lines where the coordinate system (or field line) was moving with the vertical $\mathbf{E} \times \mathbf{B}$ drift of the plasma. To an observer on the the field line, this would mean that all plasma motions appeared to be parallel to the magnetic field. By assuming a geocentric dipole in which the earth's rotational and magnetic axes are aligned and diffusion along the field line, it was demonstrated that even relatively small, upward vertical drifts (10 – 20 meters/second) at the equator combined with diffusion down the field lines away from the equator could account for the formation of the equatorial anomaly during the day [*Baxter*, 1964; *Bramley and Peart*, 1965]. The diurnal behavior of the equatorial anomaly was reproduced by assuming a sinusoidal variation of this electric field [*Baxter and Kendall*, 1968].

The processes controlling the asymmetrical distribution of the equatorial anomaly and the nighttime maintenance of the *F*-region had yet to be defined. Speculation concerning the nighttime, low-latitude *F*-region involved two processes.

The first considered an external source of ionization such as an influx of energetic particles or an influx of H⁺ ions from the protonosphere. The second proposed a change in the rate at which the ions recombine either by a change in the composition of the nighttime ionosphere or by vertical movement of the F-region into a region of lower atmospheric density. Computation of the daytime flux of H⁺ ions to the protonosphere showed that the protonosphere could not provide the necessary downward flux of H⁺ ions to maintain the F-region at night. In addition, rocket measurements indicated an upward motion of the F-region plasma [*Hanson and Patterson, 1964*]. This upward motion is the result of an equatorward, meridional neutral wind which because of drag between the neutrals and ions forces the plasma up the inclined magnetic field lines at low latitudes [*Rishbeth and Garriott, 1969*]. The meridional asymmetry of the equatorial anomaly was effectively modelled by the inclusion of a horizontal neutral wind blowing from the summer to winter hemispheres for solstice conditions into models containing diffusion and electrodynamic drifts [*Sterling et al., 1969; Abur-Robb and Windle, 1969; Bramley and Young, 1968*]. The longitudinal variation of the equatorial anomaly can be obtained by allowing for the offset of the magnetic and rotational axes. This offset shifts the neutral wind pattern – organized in geographic coordinates – in relation to the magnetic field lines and in conjunction with a longitudinal variation in the F-region electric field produces longitudinal variations in the equatorial anomaly [*Anderson, 1973a, 1973b; Chan and Walker, 1984a, 1984b*].

In 1975, Schunk [1975], noting that the basic transport equations used in aeronomical research had not generally been applied with a clear recognition of their limitations, developed a general system of transport equations valid for a multi-component gas mixture. This system of equations includes the continuity, momentum, internal energy, pressure tensor, and heat flow equations for each species of the gas. The basic problem for aeronomical studies is choosing the appropriate set of equations for the velocity distribution inherent to each

species in the gas. For undisturbed conditions, a Maxwellian distribution is appropriate, but the presence of various non-equilibrium processes often causes deviations from the Maxwellian distribution. Therefore, before the moments of the Boltzmann's equations can be obtained, the velocity distribution must be specified. Generally, the gas mixture has been assumed to be Maxwellian and the fluid equations have been applied. This general system of transport equations is developed using a 13-moment approximation and is valid for both the neutral atmosphere and the ionosphere. They can be applied to collision dominated and collisionless plasmas, and in the case of very frequent collisions, these equations give the usual Navier-Stokes expressions for the viscous stress tensor and the heat flow vector.

During the late 70's considerable attention was given to the problem of interhemispheric flows of plasma along dipole field lines. Time dependent and steady state solutions were obtained from the continuity and momentum equations between *F*-regions in the conjugate hemispheres. *Bailey et al.* [1977a] studied the interhemispheric flows of O⁺ and H⁺ ions for sunspot minimum conditions at equinox at L = 3. They found that counterstreaming between the O⁺ and H⁺ could indeed occur during the night at solar minimum, and to account for the differences between their calculated values and observed values, they concluded electrodynamic drift was important at the time the observations were made. They also studied the nighttime, field-aligned fluxes at solar maximum for L = 3 [*Bailey et al.*, 1977b]. They showed that the O⁺ flux was not related to the flux of H⁺ to or from the protonosphere; and, hence, nighttime *F*-region densities are not strongly affected by fluxes to or from the protonosphere.

In 1979, *Bailey and Moffett* [1979] extended the previous calculations to include the flux of He⁺ ions (in addition to H⁺ and O⁺) and thermal effects on field-aligned fluxes by performing steady state calculations of densities, temperatures, and flow velocities for each species. The ions were heated through collisions with the electrons, the neutrals, and each other; and the electrons were

heated through collisions with photoelectrons, and cooled due to the fine structure excitation of neutral O, and the vibrational and rotational excitation of O₂ and N₂. They assumed a geocentric dipole field line with an equatorial crossing altitude of 930 km and a north-to-south neutral wind. They concluded that the transequatorial O⁺ breeze is not significantly affected by elevated plasma temperatures, but the field-aligned velocities of H⁺ and He⁺ were strongly dependent on temperature gradients and the O⁺ field-aligned velocity. Therefore, for the light minor ions (H⁺ and He⁺) ion - ion drag cannot be ignored. It has also been reported that the H⁺ flux is upward throughout the day and not significantly affected by the H⁺ tube content; whereas, at night the H⁺ flux can be somewhat variable. The daytime, peak density in the F₂ region is reduced by about 15% by this upward flux of H⁺ and the nighttime peak density in the F-region is maintained by the neutral winds and the downward flux of H⁺ [Murphy *et al.*, 1976]. In a study of counterstreaming between O⁺ and H⁺, Young *et al.* [1979] considered the case of a dipole field tilted with respect to the earth's rotational axis under steady state conditions and found that counterstreaming must occur under these conditions as long as the neutral and ion temperatures are not the same.

A final area of investigation involves the effects of interhemispheric transport, electrodynamic drifts, and heating by photoelectrons on the plasma temperatures. Early studies by Bailey *et al.* [1973, 1975] involved the steady state solution of the energy equation with densities being supplied by the model of Moffet and Hanson [1973]. The ions were assumed to be heated through collisions with the electrons, cooled by collisions with the neutrals, and to have the same temperature ($T_{O+} = T_{H+}$). The electrons were heated through the excitation of neutral O, O₂, N₂, and the interaction with photoelectrons [Bailey *et al.*, 1975]. These solutions were valid for daytime and nighttime during equinox for low and moderate solar activity. Later studies [Bailey and Heelis, 1980; Bailey, 1980; Bailey, 1983; Moffett *et al.*, 1986] were performed with self-consistent,

time-dependent continuity, momentum, and energy equations with an empirical expression for the heat flow. The results for equinox, solar maximum with no interhemispheric transport and no electrodynamic drift above Arecibo ($L = 1.4$) indicated that for altitudes between 120 km and 2548 km O^+ was the dominant ion during the day, but was comparable to H^+ at night. During the night the ion temperatures are approximately the same, but during the day the H^+ temperature can exceed the O^+ temperature by 300°K [Bailey, 1980]. For the nighttime topside ionosphere at low and moderate solar activity, it was discovered that a meridional neutral wind could produce a trough in the ion temperatures that results in the ion temperature being cooler than the expected neutral temperature over portions of the field lines. This trough in the ion temperature was found not to form in the altitude region where there is strong interaction between the ions and neutrals because the neutrals act to quench any heating or cooling effects exerted on the ions. The latitudinal extent of this trough is determined by field line geometry and the characteristics of the *F*-region neutral winds [Bailey and Heelis, 1980].

Interhemispheric flow has been shown to significantly affect the plasma temperatures, and that for solstice conditions the flow of plasma is generally from the summer to the winter hemisphere. This interhemispheric flow results in warmer temperatures in the winter hemisphere due to adiabatic compression as the plasma descends along the field line [Bailey *et al.*, 1975; Bailey *et al.*, 1973]. The electrodynamic drift has little effect on plasma temperatures at night [Bailey, 1983; Bailey *et al.*, 1973], but is significant during the day [Bailey, 1983]. Using the coupled, time-dependent model of Bailey [1983], Moffett *et al.* [1986] demonstrated that for moderate solar activity and solstice conditions thermal coupling produces very strong upward flows of O^+ in the topside summer ionosphere at the time of sunrise in the winter hemisphere and a lesser, but opposite, effect at the time of winter sunset. For these conditions, counterstreaming between the H^+ and O^+ ions occurs with the total flux at 500 km being primarily

composed of H^+ ions. Additionally, the O^+ ions were found to exhibit strong upward and downward flows at sunrise and sunset, respectively.

Since the ions are primarily heated by the electrons, it is appropriate to now discuss some of the properties of the electron gas. Extreme ultraviolet radiation is the primary energy source for the electrons during the day. Energetic photoelectrons are created through the photoionization of the neutrals and these photoelectrons lose their energy in elastic collisions with the ambient electron gas and inelastic collisions with the neutrals and ions [Schunk and Nagy, 1980]. At the heights being considered by our model, the primary loss to the neutrals occurs through the fine structure excitation of O [Bailey and Heelis, 1980]. Below 250 – 300 km, photoelectrons lose their energy locally; above this height, they escape along magnetic field lines, heating the ambient electron gas at high altitudes. This results in the electron temperatures being greater than the ion temperatures during the day [Schunk and Nagy, 1980].

Model and Assumptions

This thesis presents the results of a time-dependent, self-consistent model of the equatorial ionosphere. This model is intended to be incorporated with other models covering other ionospheric regions (mid and high latitudes) to form a three-dimensional, global model of the terrestrial ionosphere. In this model, the continuity, momentum, and energy equations for O^+ , H^+ , and electrons are coupled and solved in a quasi-simultaneous manner by first solving for the coupled H^+ and O^+ densities and then solving for the electron temperature, the H^+ temperature, and the O^+ temperature at each time step. For the daytime case, we use an empirical expression for the heating rates due to photoelectrons which were obtained from the results of Swartz *et al.* [1975] (to be discussed in more depth in Chapter III). Our neutral atmosphere comes from the MSIS86 empirical model [Hedin, 1987].

In the formulation of this equatorial model, a number of assumptions were made which will now be commented on. The electron densities are calculated through the assumption of charge neutrality, and the field-aligned velocities for the electrons are obtained by assuming that there are no currents flowing parallel to \mathbf{B} . This assumption is supported by the results of *Kendall and Pickering* [1967] who found that for reasonable estimates of the parallel current in the low-latitude ionosphere, the effects of this parallel current on the field-aligned drift velocity is negligible and that the standard view of ambipolar diffusion along field lines is correct. We consider an ionosphere composed of two ion species, H^+ and O^+ , and electrons. This assumption is justified because O^+ and H^+ are the dominant ions between the F_2 peak and 3000 km, and NO^+ ceases to be the dominant ion between 150 and 250 km [*Banks and Kockarts*, 1973; *Anderson and Rusch*, 1980]. Additionally, *Schunk and Walker* [1973] have shown that the O^+ density is not significantly affected by E -region polarization electric fields and molecular ion densities in the region where O^+ is the dominant ion. Our use of the fluid equations assumes the ionospheric gas mixture has a Maxwellian velocity distribution and that along the field lines the mean-free-path for collisions between the H^+ (neutrals at low altitudes) and O^+ ions is smaller than the O^+ scale height; these are true in the equatorial ionosphere. The fluid behavior of the plasma is also enhanced by the presence of the magnetic field which acts to create plasma flows parallel to \mathbf{B} [*Chen*, 1984]. For diffusion parallel to \mathbf{B} to exist, the gyrofrequency of a species must be greater than the collision frequency for the species [*Banks and Kockarts*, 1973]. This condition is met at all altitudes being examined by our model, except at the very base of the field line where photochemistry is the dominant process.

For the last 10 years, a number of models of the low-latitude ionosphere have taken into account the electrodynamic drift of the plasma. However, these studies involved very "idealized" electric fields or assumed a value for the equatorial drift velocity [*Bailey*, 1983; *Bailey and Moffett*, 1979; *Sterling et al.*, 1969]. In

some cases, the electric field or the electrodynamic drift velocity was chosen to obtain the best fit to a set of observations [Anderson, 1973a, 1973b]. Only *Chan and Walker* [1984a, 1984b] used an electric field model that was based on observations over a variety of conditions at more than one observing site. Unfortunately, they assumed the vertical drift velocities were invariant along a given field line. This is probably an erroneous assumption, since field lines are generally considered to be equipotential [Richmond *et al.*, 1980] and dipole field lines converge as one moves downward in altitude along them. This should lead to a variation of the electric field along the field line, and, hence, a variation in the electrodynamic drift velocity. We, therefore, calculated the variation of electrodynamic drift velocity along a given field line by exploiting the equipotentiality of the field line (See Appendix C for details of our method). Using these techniques, we feel the variation of the electrodynamic drifts along the field line, with season, and with local time, avoid *a priori* assumptions concerning densities along the field line or electric field variations. This should increase the general accuracy and applicability of our model.

Additionally, few studies [Anderson, 1973a, 1973b; *Chan and Walker*, 1980a, 1980b; *Young et al.*, 1979] have treated the dipole field as having a tilt in relation to the earth's rotational axis, except perhaps through incorporating the effects in the "idealized" neutral winds that were assumed. Our model provides self-consistent values for the neutral winds as a function of latitude, altitude, season, solar activity (maximum or minimum), longitude, and local time. Details of our neutral wind model are included in Appendix A. It should be noted, however, that our neutral wind model is empirical and the coupling of both an ionospheric model and a neutral atmosphere model is required for truly consistent calculations. It is felt that, like the electric field model, this neutral wind model enhances the general applicability of our overall modelling efforts.

Finally, it should be noted that while the azimuthal component of the electrodynamic drift has been assumed negligible based on the results of *Sterling et*

al. [1969], most electric field models used up to this point are very "idealized" or simplistic (perhaps too much so). Therefore, a re-evaluation of this assumption should be undertaken, especially near sunrise and sunset where horizontal gradients become significant. Our model should be able to more realistically determine the validity of the assumption.

CHAPTER II

CONTINUITY AND MOMENTUM EQUATIONS

An Orthogonal, Curvilinear Coordinate System

We wish to model the variations of ion and electron temperature and density for a topside, low-latitude ionosphere composed of two ion species, O^+ and H^+ . To accomplish this, the plasma is assumed to diffuse parallel to the magnetic field line and drift normal to the field line due to $E \times B$ forces. For a magnetic dipole, it is convenient to adopt a curvilinear, orthogonal coordinate system which has one coordinate parallel to B and one coordinate normal to B . The coordinates in this system may be defined as p , q , and ϕ where ϕ is the magnetic longitude. The location of any point along a given field line may be uniquely defined in terms of p and q where the field lines are represented by a family of curves along which p is constant, and the equipotential surfaces are represented by the family of curves along which q is constant. Expressions relating the p-q coordinate system to spherical coordinates are

$$p = \frac{r}{r_e \sin^2 \theta} \quad (1)$$

and

$$q = \frac{r_e^2 \cos \theta}{r^2} \quad (2)$$

where r_e is the radius of the earth, r is the radius of any given point, and θ is the magnetic colatitude. The equation for a field line is

$$r = a \sin^2 \theta \quad (3)$$

where a is the radius of the field line at the equator. Since we are interested in parallel motion, the unit tangent to the field line is defined as

$$\hat{t} = (\sin I, \cos I, \phi) \quad (4)$$

with \hat{i} being defined positive above the horizontal and directed towards the geomagnetic equator in the northern hemisphere. If s is a unit arc length along the field line, then

$$\frac{\partial}{\partial s} = \sin I \frac{\partial}{\partial r} + \frac{\cos I}{r} \frac{\partial}{\partial \theta} = -\frac{\sigma^{1/2} r_e^2}{r^3} \frac{\partial}{\partial q} \quad (5)$$

where $\sigma = (1 + 3 \cos^2 \theta)$ [Kendall, 1962]. See Figure 1 for an example of how q varies along a field line.

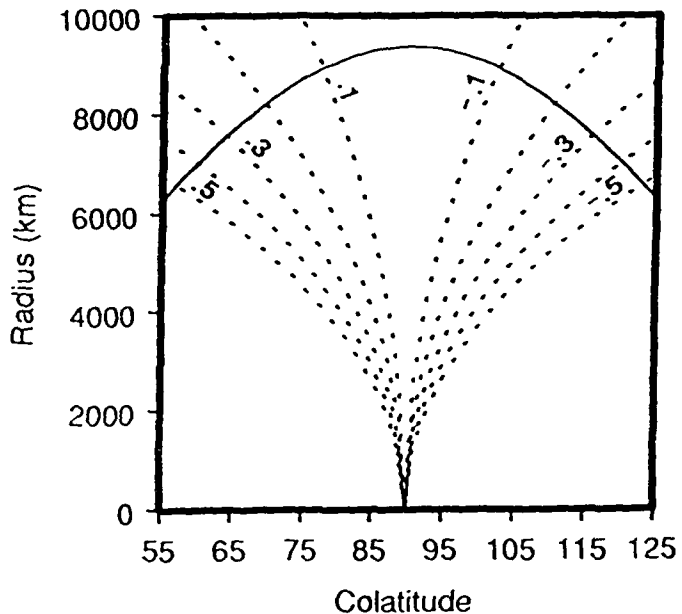


Figure 5. A diagram showing the variation of q along a magnetic field line that crosses the equator at 3000 km altitude. The solid curve represents the field line (or a curve of constant p) and the dashed curves show lines of constant q . Δq is chosen to be 0.1.

Transport Equations

At low and middle latitudes the ion or electron number density is determined by two main processes. These are atmospheric photochemistry and transport. Both processes can be effectively modelled using the equations for the conservation of mass and momentum so long as the plasma can be thought to behave as a fluid. These conservation equations are obtained by taking the moments of

the Boltzmann equation. The continuity equation can be written as

$$\frac{\partial n_s}{\partial t} + \operatorname{div}(n_s \mathbf{u}_s) = P_s - L_s n_s \quad (6)$$

where n_s is the number density, \mathbf{u}_s is the plasma drift velocity for the species, P_s is the photochemical production, and L_s is the chemical loss rate [s^{-1}]. The momentum equation is of the form

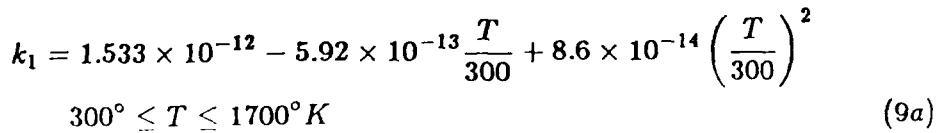
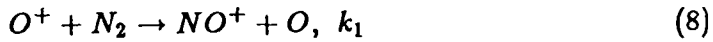
$$n_s m_s \left(\frac{D \mathbf{u}_s}{Dt} \right) + \nabla p_s + \nabla \cdot \tau_s - n_s m_s \mathbf{G} \\ - n_s e_s \left[\mathbf{E} + \left(\frac{1}{c} \right) \mathbf{u}_s \times \mathbf{B} \right] = \frac{\delta \mathbf{M}_s}{\delta t} \quad (7)$$

where m_s is the mass of species s , $p_s = n_s k T_s$ is the partial pressure for an ideal gas, e_s is the charge, T_s is the temperature, τ_s is the stress tensor, $\frac{D}{Dt} = \frac{\partial}{\partial t} + \mathbf{u}_s \cdot \nabla$ is the convective derivative, \mathbf{G} is the acceleration due to gravity, \mathbf{E} is the electric field, \mathbf{B} is the magnetic field, c is the speed of light, \mathbf{M}_s is the rate of momentum exchange due to collisions of s with other species, and k is Boltzmann's constant [Schunk, 1983].

Atmospheric Chemistry

Although this model is primarily valid for the diffusion dominated portion of the ionosphere where charge exchange between H^+ and O^+ are the dominant chemical reactions, the ion-atom interchange reaction, of O^+ with O_2 and N_2 , and the photoionization of atomic oxygen are also included.

Chemical reactions.



$$k_1 = 2.73 \times 10^{-12} - 1.155 \times 10^{-12} \frac{T}{300} + 1.483 \times 10^{-13} \left(\frac{T}{300} \right)^2$$

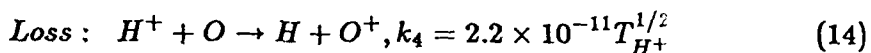
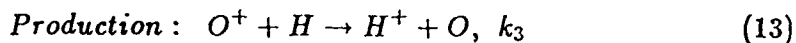
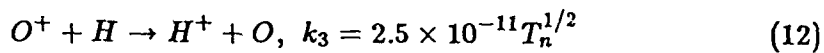
$$1700^\circ < T < 6000^\circ K \quad (9b)$$



$$k_2 = 2.82 \times 10^{-11} - 7.74 \times 10^{-12} \frac{T}{300} + 1.073 \times 10^{-12} \left(\frac{T}{300} \right)^2$$

$$- 5.17 \times 10^{-14} \left(\frac{T}{300} \right)^3 + 9.65 \times 10^{-16} \left(\frac{T}{300} \right)^4$$

$$300^\circ \leq T \leq 6000^\circ K \quad (11)$$



The reaction rates are in $cm^3 s^{-1}$ and the temperatures are in $^\circ K$ [Schunk, 1983].

Photoionization. At low altitudes, the primary source for O^+ is through the photoionization of neutral O. The Chapman production function describing this reaction is of the form

$$P(h, \chi) = P_\infty n(O) \exp(-\alpha(h, \chi)) \quad (15)$$

where P_∞ is the total production of ion-electron pairs for an overhead sun over all ionizing wavelengths of O, h is the altitude of the point, χ is the solar zenith angle, and α is the optical depth. P_∞ is based on the integrated solar flux values in seven bands from 165Å to 911Å and the average ionization cross-sections of O for each band assuming each absorbed photon produces an ion-electron pair.

The value of $1.1 \times 10^{-7} s^{-1}$ was adopted for solar minimum conditions [Banks and Kockarts, 1973]. The variation of P_∞ with sunspot number is given by

$$P_\infty (\bar{R}) = 1.1 \times 10^{-7} (1 + 0.0124\bar{R}) \quad (16)$$

where \bar{R} is the average sunspot number. The optical depth is given by

$$\begin{aligned} \alpha(h, \chi) &= \sigma_a(O) n(O) H(O) Ch\left(\frac{r}{H(O)}, \chi\right) + \sigma_a(N_2) \\ &\cdot n(N_2) H(N_2) Ch\left(\frac{r}{H(N_2)}, \chi\right) \end{aligned} \quad (17)$$

where σ_a is the ionization cross-section, H is the scale height, and $Ch\left(\frac{r}{H}, \chi\right)$ is the Chapman function. The adopted values for the ionization cross-section are $\sigma_a(O) = 0.9 \times 10^{-17}$ and $\sigma_a(N_2) = 1.5 \times 10^{-17}$ [Anderson, 1973b]. The equations for the Chapman function for any point p take into account grazing incidence and are as follows:

For $\chi_p \leq 90^\circ$

$$Ch(X_p, \chi_p) = \left(\frac{\pi}{2} X_p\right)^{\frac{1}{2}} \frac{a + by}{c + dy + y^2}; \quad 0 \leq y < 8 \quad (18)$$

$$Ch(X_p, \chi_p) = \left(\frac{\pi}{2} X_p\right)^{\frac{1}{2}} \frac{f}{g + y}; \quad 8 \leq y \leq 100 \quad (19)$$

For $\chi_p > 90^\circ$

$$\begin{aligned} Ch(X_p, \chi_p) &= (2\pi X_p)^{\frac{1}{2}} \left[\sin(\chi_p)^{\frac{1}{2}} \exp(X_p(1 - \sin \chi_p)) \right. \\ &\left. - \frac{1}{2} \frac{a + by}{c + dy + y^2} \right]; \quad 0 \leq y < 8 \end{aligned} \quad (20)$$

$$\begin{aligned} Ch(X_p, \chi_p) &= (2\pi X_p)^{\frac{1}{2}} \left[\sin(\chi_p)^{\frac{1}{2}} \exp(X_p(1 - \sin \chi_p)) \right. \\ &\left. - \frac{1}{2} \frac{f}{g + y} \right]; \quad 8 \leq y \leq 100 \end{aligned} \quad (21)$$

where

$$y = \left(\frac{X_p}{2} \right)^{\frac{1}{2}} |\cos \chi_p|, \quad (22)$$

$$X_p = \frac{r}{H}, \quad (23)$$

$a = 1.0606963$, $b = 0.55643831$, $c = 1.0619896$, $d = 1.7245609$, $f = 0.56498823$, and $g = 0.06651874$ [Smith and Smith, 1972]. The solar zenith angle was computed using the formula found in Schunk and Walker, [1973] which is

$$\cos \chi_p = \sin \xi \sin \varphi + \cos \xi \cos \varphi \cos \left(\frac{2\pi (HL - 12)}{24} \right) \quad (23)$$

where ξ is the solar declination angle, HL is the local solar time in hours, and φ is the geographic latitude. From the above equations, the dominant photochemical reactions can be accounted for with the exception of the reactions involving NO^+ which are only important at the lowest altitudes being considered.

Momentum Equation

The calculation of the time-varying ion and electron number densities along the field line requires the parallel component of the ion/electron drift to be specified. These parallel drift velocities can be obtained from equation (7). First, if the following assumptions are made: (a) steady state ($\frac{\partial}{\partial t} = 0$), (b) the parallel drifts are subsonic, therefore, the nonlinear terms in (7) can be neglected, (c) heat flow in the collision term ($\frac{\delta M_s}{\delta t}$) is negligible, (d) no field-aligned currents, (e) flow is parallel to \mathbf{B} ($\mathbf{u}_s'' \times \mathbf{B} = 0$), and (f) viscous effects can be neglected, equation (7) becomes

$$\nabla p_s - n_s m_s \mathbf{G} - n_s e_s \mathbf{E} = \frac{\delta M_s}{\delta t}. \quad (24)$$

Now, by assuming a perfect gas and realizing that along the field line $\mathbf{G} = g \sin I \hat{\mathbf{l}}$

where \hat{t} is a unit vector parallel to \mathbf{B} , equation (24) can be rewritten as

$$\frac{\partial}{\partial s} (n_s k T_s) \hat{t} + n_s m_s g \sin I \hat{t} - n_s e_s \mathbf{E} = \frac{\delta \mathbf{M}_s}{\delta t}. \quad (25)$$

The electric field in equation (25) can be obtained from the electron momentum equation by making the same assumptions as before and by neglecting gravity and the collisional terms due to the much smaller mass of the electrons. This gives

$$\mathbf{E} = -\frac{k}{e N_e} \left(N_e \frac{\partial T_e}{\partial s} + T_e \frac{\partial N_e}{\partial s} \right) \hat{t}. \quad (26)$$

Substituting equation (26) into (25) and assuming charge neutrality gives

$$\begin{aligned} k T_s \frac{\partial n_s}{\partial s} \hat{t} + n_s k \frac{\partial T_s}{\partial s} \hat{t} + n_s m_s g \sin I \hat{t} + k n_s \frac{\partial T_e}{\partial s} \hat{t} \\ + \frac{k T_e n_s}{N_e} \frac{\partial N_e}{\partial s} \hat{t} - \frac{\delta \mathbf{M}_s}{\delta t} = 0. \end{aligned} \quad (27)$$

Next, the rate of transfer of momentum due to collisions needs to be evaluated. Since general expressions for this quantity are only available for limited particle distributions, it becomes necessary to assume the ionosphere approximates a displaced Maxwellian distribution. This leads to the 5-moment approach since it involves density, temperature, and three components of velocity for each species. Ignoring the heat flow terms, as has already been assumed, the rate of momentum transfer can be expressed as

$$\frac{\delta \mathbf{M}_s}{\delta t} = - \sum_t n_s m_s \nu_{st} (\mathbf{u}_s'' - \mathbf{u}_t'') \quad (28)$$

where ν_{st} is the collision frequency for momentum transfer between species s and t [Schunk, 1983].

Substituting equation (28) into (27) and rewriting the resulting equation gives

$$\begin{aligned} \mathbf{u}_s'' = \mathbf{u}_t'' \frac{\nu_{st}}{\nu_{sn} + \nu_{st}} - \frac{k T_s}{m_s (\nu_{sn} + \nu_{st})} \left(\frac{1}{n_s} \frac{\partial n_s}{\partial s} + \frac{1}{T_s} \frac{\partial T_s}{\partial s} + \frac{m_s g \sin I}{k T_s} \right. \\ \left. + \frac{1}{T_s} \frac{\partial T_e}{\partial s} + \frac{T_e}{T_s N_e} \frac{\partial N_e}{\partial s} - \frac{\nu_{sn} U \cos I m_s}{k T_s} \right) \hat{t} \end{aligned} \quad (29)$$

where $U \cos I\hat{t}$ is the parallel (to \mathbf{B}) component of the meridional neutral winds.

If we define

$$\Delta_s \equiv \left(1 + \frac{\nu_{sn}}{\nu_{st}} \right)^{-1}, \quad (30)$$

then the diffusion coefficient becomes

$$D_s = \frac{kT_s}{m_s \nu_{st}} \Delta_s. \quad (31)$$

By also defining,

$$Q_s = \left(\frac{m_s g \sin I}{kT_s} + \frac{1}{T_s} \frac{\partial T_s}{\partial s} + \frac{1}{T_s} \frac{\partial T_e}{\partial s} - \frac{m_s \nu_{sn} U \cos I}{kT_s} \right) \hat{t}, \quad (32)$$

the momentum equation becomes

$$\mathbf{u}_s'' = \mathbf{u}_t'' \Delta_s - D_s \left(\frac{1}{n_s} \frac{\partial n_s}{\partial s} + \frac{T_e}{T_s N_e} \frac{\partial N_e}{\partial s} + Q_s \right) \hat{t}. \quad (33)$$

Equation (33) is now ready to be substituted into the continuity equation.

Continuity Equation

The continuity equation allows us to calculate the time-varying ion/electron densities along the field line. Using *Sterling et al.*'s [1969] technique, \mathbf{u}_s can be broken down into its components giving

$$\mathbf{u}_s = \mathbf{u}_{em} + \mathbf{u}_{th} + \mathbf{u}_s'' \quad (34)$$

where \mathbf{u}_{th} is the vertical velocity of the neutral air due to thermal expansion and contraction, and \mathbf{u}_{em} is the electrodynamic drift of the ionosphere. Equation (6) now becomes

$$\frac{\partial n_s}{\partial t} = P_s - L_s n_s - \operatorname{div}(n_s \mathbf{u}_{em}) - \operatorname{div}(n_s \mathbf{u}_s'') - \operatorname{div}(n_s u_{th} \sin I \hat{t}). \quad (35)$$

Now, using the following definitions:

$$-\operatorname{div} (n_s u_{th} \hat{t}) = \hat{t} \cdot \operatorname{grad} (-n_s u_{th}) - n_s u_{th} \operatorname{div} \hat{t} \quad (36)$$

[Sterling et al., 1969],

$$\operatorname{div} (\hat{t}) = \frac{9 \cos \theta + 15 \cos^3 \theta}{r \sigma^{3/2}}, \quad (37)$$

$$\hat{t} \cdot \operatorname{grad} \equiv \frac{\partial}{\partial s} \quad (38)$$

[Kendall, 1962], and equation (33), the various divergences can be expanded.

In general, the vertical velocity of a surface of constant pressure can be written as

$$u_{th} = \frac{\Omega}{T_\infty} \frac{\partial T_\infty}{\partial \phi} \frac{(z - z_0) r}{r_e + z_0} \quad (39)$$

assuming $T = T_\infty$ and T_∞ is independent of z where $z_0 \equiv 120$ km and Ω is the earth's rotation. Now, using equations (36) – (39)

$$\begin{aligned} \operatorname{div} (-n_s u_{th} \sin I \hat{t}) &= \frac{2 \cos \theta r_e^2 u_{th}}{r^3} \frac{\partial n_s}{\partial q} + n_s A_2 \frac{\partial (u_{th} \sin I)}{\partial q} \\ &\quad - n_s u_{th} \sin I \left(\frac{9 \cos \theta + 15 \cos^3 \theta}{r \sigma^{3/2}} \right). \end{aligned} \quad (40)$$

The electrodynamic drift can also be separated into its components giving

$$\mathbf{u}_{em} = \mathbf{u}_\perp + \mathbf{u}_\phi + \Omega r \sin \theta \hat{\phi}. \quad (41)$$

Since the $\operatorname{div} (-n_s \Omega r \sin \theta \hat{\phi}) = 0$,

$$\operatorname{div} (-n_s \mathbf{u}_{em}) = \operatorname{div} (-n_s \mathbf{u}_\perp) + \operatorname{div} (-n_s \mathbf{u}_\phi). \quad (42)$$

Recall, that we are interested in the drifts and densities along a given field line, and that it is convenient to allow the coordinate system to move with velocity,

\mathbf{u}_{em} . Using the definition for the convective derivative, we get

$$\frac{Dn_s}{Dt} = \frac{\partial n_s}{\partial t} + \mathbf{u}_{\text{em}} \cdot \nabla n_s. \quad (43)$$

The divergences of the electrodynamic drifts are

$$\text{div}(\mathbf{u}_\perp) = \frac{\partial u_{\perp 0}}{\partial r_e} + \frac{4u_{\perp 0}}{r\sigma^2} (6\cos^6\theta - 3\cos^4\theta - 4\cos^2\theta + 1) \quad (44)$$

and

$$\text{div}(\mathbf{u}_\phi) = \frac{1}{r\sin\theta} \frac{\partial u_\phi}{\partial\phi} \quad (45)$$

where $u_{\perp 0}$ is the value of \mathbf{u}_\perp at the equator.

Substituting equation (33) into (35) and using previous assumptions give

$$\begin{aligned} \text{div}(-n_s \mathbf{u}_s'') &= \frac{\partial(D'_s A_2)}{\partial q} \frac{A_2}{n_t} \frac{\partial n_s}{\partial q} + D'_s \left(-\frac{A_2^2}{n_t^2} \frac{\partial n_t}{\partial q} \frac{\partial n_s}{\partial q} + \frac{A_2^2}{n_t} \frac{\partial^2 n_s}{\partial q^2} \right. \\ &\quad \left. - \frac{A_2 A_3}{n_t} \frac{\partial n_s}{\partial q} \right) + \frac{\partial W_s}{\partial q} \frac{n_s A_2}{n_t N_e} \frac{\partial N_e}{\partial q} + W_s \left(\frac{A_2 n_s}{n_t N_e} \frac{\partial^2 N_e}{\partial q^2} \right. \\ &\quad \left. + \frac{A_2}{N_e n_t} \frac{\partial N_e}{\partial q} \frac{\partial n_s}{\partial q} - \frac{A_2 n_s}{N_e n_t^2} \frac{\partial N_e}{\partial q} \frac{\partial n_t}{\partial q} - \frac{A_2 n_s}{n_t N_e^2} \left(\frac{\partial N_e}{\partial q} \right)^2 \right. \\ &\quad \left. - \frac{A_3 n_s}{n_t N_e} \frac{\partial N_e}{\partial q} \right) - \frac{\partial V_s}{\partial q} \frac{A_2 n_s}{n_t} - V_s \left(\frac{A_2}{n_t} \frac{\partial n_s}{\partial q} \right. \\ &\quad \left. - \frac{A_2 n_s}{n_t^2} \frac{\partial n_t}{\partial q} - A_3 \frac{n_s}{n_t} \right) \end{aligned} \quad (46)$$

where n_t is the number density of the other ion, $D'_s = D_s n_t$, $V_s = D'_s Q_s$,

$$A_2 = -\frac{\sigma^{1/2} r_e^2}{r^3}, \quad (47)$$

$$W_s = \frac{A_2 T_e D'_s}{T_s}, \quad (48)$$

and

$$A_3 = \frac{9\cos\theta + 15\cos^3\theta}{r\sigma^{3/2}}. \quad (49)$$

Now, by combining equations (35), (40), (42), and (44) – (46) we can write the general form of the nonlinear, second-order partial differential equation which couples both ions and gives the time-varying ion densities along a field line as

$$\begin{aligned}
 \frac{Dn_s}{Dt} = & P_s - L_s n_s - n_s \left[\frac{\partial u_{\perp o}}{\partial r_e} + \frac{4u_{\perp o}}{r\sigma^2} (6\cos^6\theta - 3\cos^4\theta - 4\cos^2\theta + 1) \right] \\
 & - n_s \left(\frac{1}{r\sin\theta} \frac{\partial u_\phi}{\partial\phi} \right) + \frac{2\cos\theta r_e^2 u_{th}}{r^3} \frac{\partial n_s}{\partial q} + n_s A_2 \frac{\partial (u_{th} \sin I)}{\partial q} \\
 & - A_3 n_s u_{th} \sin I + A_2 u_t'' \Delta_s \frac{\partial n_s}{\partial q} + A_2 n_s \frac{\partial (u_t'' \Delta_s)}{\partial q} - A_3 u_t'' \Delta_s n_s \\
 & + \frac{A_2}{n_t} \frac{\partial (A_2 D'_s)}{\partial q} \frac{\partial n_s}{\partial q} + D'_s \left(-\frac{A_2^2}{n_t^2} \frac{\partial n_t}{\partial q} \frac{\partial n_s}{\partial q} + \frac{A_2^2}{n_t} \frac{\partial^2 n_s}{\partial q^2} - \frac{A_2 A_3}{n_t} \frac{\partial n_s}{\partial q} \right) \\
 & + \frac{\partial W_s}{\partial q} \frac{A_2 n_s}{N_e n_t} \frac{\partial N_e}{\partial q} - \frac{\partial V_s}{\partial q} \frac{A_2 n_s}{n_t} - V_s \left(\frac{A_2}{n_t} \frac{\partial n_s}{\partial q} - \frac{A_2 n_s}{n_t^2} \frac{\partial n_t}{\partial q} \right. \\
 & \left. - A_3 \frac{n_s}{n_t} \right) + W_s \left(\frac{A_2 n_s}{n_t N_e} \frac{\partial^2 N_e}{\partial q^2} + \frac{A_2}{N_e n_t} \frac{\partial N_e}{\partial q} \frac{\partial n_s}{\partial q} - \frac{A_2 n_s}{N_e n_t^2} \frac{\partial N_e}{\partial q} \frac{\partial n_t}{\partial q} \right. \\
 & \left. - \frac{A_2 n_s}{n_t N_e^2} \left(\frac{\partial N_e}{\partial q} \right)^2 - \frac{A_3 n_s}{n_t N_e} \frac{\partial N_e}{\partial q} \right). \tag{50}
 \end{aligned}$$

To solve this equation numerically, it becomes necessary to linearize all terms. This is accomplished by performing a time-varying Taylor's expansion on the nonlinear terms and then substituting them back into equation (50). After linearization, a second-order differential equation for the ions of the form

$$\frac{Dn_s}{Dt} = C_1 \frac{\partial^2 n_s}{\partial q^2} + C_2 \frac{\partial n_s}{\partial q} + C_3 n_s + C_4 \frac{\partial^2 n_t}{\partial q^2} + C_5 \frac{\partial n_t}{\partial q} + C_6 n_t + C_7 \tag{51}$$

results. The various coefficients for each species are presented below.

O^+

$$C_1 = A_2^2 D'_2 \left(\frac{1}{N_{H^+}} \right)^\circ + W_2 A_2 \left(\frac{N_{O^+}}{N_{H^+} N_e} \right)^\circ \tag{52}$$

$$C_2 = A_2 u_{H^+}'' \Delta_2 + A_2 \frac{\partial}{\partial q} (A_2 D'_2) \left(\frac{1}{N_{H^+}} \right)^\circ - A_2 A_3 D'_2 \left(\frac{1}{N_{H^+}} \right)^\circ$$

$$\begin{aligned}
& + A_2 \frac{\partial W_2}{\partial q} \left(\frac{N_{O^+}}{N_{H^+} + N_e} \right)^\circ - A_2 V_2 \left(\frac{1}{N_{H^+}} \right)^\circ + W_2 A_2 \left(\frac{1}{N_{H^+} + N_e} \frac{\partial N_{O^+}}{\partial q} \right. \\
& \left. + \frac{1}{N_{H^+} + N_e} \frac{\partial N_e}{\partial q} \right)^\circ - A_2 W_2 \left(\frac{N_{O^+}}{N_e N_{H^+}^2} \frac{\partial N_{H^+}}{\partial q} \right)^\circ - A_2 W_2 \left(\frac{2N_{O^+}}{N_{H^+} + N_e^2} \frac{\partial N_e}{\partial q} \right)^\circ \\
& - A_3 W_2 \left(\frac{N_{O^+}}{N_{H^+} + N_e} \right)^\circ + \frac{2 \cos \theta r_e^2 u_{th}}{r^3} - A_2^2 D'_2 \left(\frac{1}{N_{H^+}^2} \frac{\partial N_{H^+}}{\partial q} \right)^\circ
\end{aligned} \quad (53)$$

$$\begin{aligned}
C_3 = & -2.5 \times 10^{-11} T_n^{1/2} n(H) - k_2 n(O_2) - k_1 n(N_2) - \frac{\partial u_{\perp o}}{\partial r_e} \\
& - \frac{4u_{\perp o}}{r\sigma^2} \left(6 \cos^6 \theta - 3 \cos^4 \theta - 4 \cos^2 \theta + 1 \right) - \left(\frac{1}{r \sin \theta} \frac{\partial u_\phi}{\partial \phi} \right) \\
& + A_2 \frac{\partial}{\partial q} (u''_{H^+} \Delta_2) + A_2 \frac{\partial W_2}{\partial q} \left(\frac{1}{N_{H^+} + N_e} \frac{\partial N_e}{\partial q} - \frac{N_{O^+}}{N_{H^+} + N_e^2} \frac{\partial N_e}{\partial q} \right)^\circ \\
& - A_2 \frac{\partial V_2}{\partial q} \left(\frac{1}{N_{H^+}} \right)^\circ + A_2 V_2 \left(\frac{1}{N_{H^+}^2} \frac{\partial N_{H^+}}{\partial q} \right)^\circ + A_3 V_2 \left(\frac{1}{N_{H^+}} \right)^\circ \\
& + A_2 W_2 \left(\frac{1}{N_{H^+} + N_e} \frac{\partial^2 N_e}{\partial q^2} - \frac{N_{O^+}}{N_{H^+} + N_e^2} \frac{\partial^2 N_e}{\partial q^2} \right)^\circ \\
& - A_2 W_2 \left(\frac{1}{N_{H^+} + N_e^2} \frac{\partial N_{O^+}}{\partial q} \frac{\partial N_e}{\partial q} \right)^\circ - A_2 W_2 \left(\frac{1}{N_e N_{H^+}^2} \frac{\partial N_{H^+}}{\partial q} \frac{\partial N_e}{\partial q} \right. \\
& \left. - \frac{N_{O^+}}{N_{H^+} + N_e^2} \frac{\partial N_{H^+}}{\partial q} \frac{\partial N_e}{\partial q} \right)^\circ - A_2 W_2 \left(\frac{1}{N_{H^+} + N_e^2} \left(\frac{\partial N_e}{\partial q} \right)^2 \right. \\
& \left. - \frac{2N_{O^+}}{N_{H^+} + N_e^3} \left(\frac{\partial N_e}{\partial q} \right)^2 \right)^\circ - A_3 W_2 \left(\frac{1}{N_{H^+} + N_e} \frac{\partial N_e}{\partial q} \right. \\
& \left. - \frac{N_{O^+}}{N_{H^+} + N_e^2} \frac{\partial N_e}{\partial q} \right)^\circ + A_2 \frac{\partial}{\partial q} (u_{th} \sin I) - A_3 u_{th} \sin I \\
& - u''_{H^+} \Delta_2 A_3
\end{aligned} \quad (54)$$

$$C_4 = W_2 A_2 \left(\frac{N_{O^+}}{N_{H^+} + N_e} \right)^\circ \quad (55)$$

$$\begin{aligned}
C_5 = & -A_2^2 D'_2 \left(\frac{1}{N_{H^+}^2} \frac{\partial N_{O^+}}{\partial q} \right)^\circ + A_2 \frac{\partial W_2}{\partial q} \left(\frac{N_{O^+}}{N_{H^+} + N_e} \right)^\circ + A_2 V_2 \left(\frac{N_{O^+}}{N_{H^+}^2} \right)^\circ \\
& + A_2 W_2 \left(\frac{1}{N_{H^+} + N_e} \frac{\partial N_{O^+}}{\partial q} \right)^\circ - A_2 W_2 \left(\frac{N_{O^+}}{N_e N_{H^+}^2} \frac{\partial N_{H^+}}{\partial q} + \frac{N_{O^+}}{N_e N_{H^+}^2} \frac{\partial N_e}{\partial q} \right)^\circ \\
& - A_2 W_2 \left(\frac{2N_{O^+}}{N_{H^+} + N_e^2} \frac{\partial N_e}{\partial q} \right)^\circ - A_3 W_2 \left(\frac{N_{O^+}}{N_{H^+} + N_e} \right)^\circ
\end{aligned} \quad (56)$$

$$\begin{aligned}
C_6 = & 2.2 \times 10^{-11} T_{H^+}^{1/2} n(O) - A_2 \frac{\partial}{\partial q} (A_2 D'_2) \left(\frac{1}{N_{H^+}^2} \frac{\partial N_{O^+}}{\partial q} \right)^\circ \\
& + A_2^2 D'_2 \left(\frac{2}{N_{H^+}^3} \frac{\partial N_{O^+}}{\partial q} \frac{\partial N_{H^+}}{\partial q} \right)^\circ - A_2^2 D'_2 \left(\frac{1}{N_{H^+}^2} \frac{\partial^2 N_{O^+}}{\partial q^2} \right)^\circ \\
& + A_2 A_3 D'_2 \left(\frac{1}{N_{H^+}^2} \frac{\partial N_{O^+}}{\partial q} \right)^\circ - A_2 \frac{\partial W_2}{\partial q} \left(\frac{N_{O^+}}{N_{H^+} N_e^2} \frac{\partial N_e}{\partial q} \right. \\
& \left. + \frac{N_{O^+}}{N_e N_{H^+}^2} \frac{\partial N_e}{\partial q} \right)^\circ + A_2 \frac{\partial V_2}{\partial q} \left(\frac{N_{O^+}}{N_{H^+}^2} \right)^\circ + A_2 V_2 \left(\frac{1}{N_{H^+}^2} \frac{\partial N_{O^+}}{\partial q} \right)^\circ \\
& - A_2 V_2 \left(\frac{2 N_{O^+} \partial N_{H^+}}{N_{H^+}^3 \partial q} \right)^\circ - A_3 V_2 \left(\frac{N_{O^+}}{N_{H^+}^2} \right)^\circ - A_2 W_2 \left(\frac{N_{O^+}}{N_e N_{H^+}^2} \frac{\partial^2 N_e}{\partial q^2} \right. \\
& \left. + \frac{N_{O^+}}{N_{H^+} N_e^2} \frac{\partial^2 N_e}{\partial q^2} \right)^\circ - A_2 W_2 \left(\frac{1}{N_e N_{H^+}^2} \frac{\partial N_{O^+}}{\partial q} \frac{\partial N_e}{\partial q} \right. \\
& \left. + \frac{1}{N_{H^+} N_e^2} \frac{\partial N_{O^+}}{\partial q} \frac{\partial N_e}{\partial q} \right)^\circ + A_2 W_2 \left(\frac{N_{O^+}}{N_{H^+}^2 N_e^2} \frac{\partial N_{H^+}}{\partial q} \frac{\partial N_e}{\partial q} \right. \\
& \left. + \frac{2 N_{O^+}}{N_e N_{H^+}^3} \frac{\partial N_{H^+}}{\partial q} \frac{\partial N_e}{\partial q} \right)^\circ + A_2 W_2 \left(\frac{N_{O^+}}{N_{H^+}^2 N_e^2} \left(\frac{\partial N_e}{\partial q} \right)^2 \right. \\
& \left. + \frac{2 N_{O^+}}{N_{H^+} N_e^3} \left(\frac{\partial N_e}{\partial q} \right)^2 \right)^\circ + A_3 W_2 \left(\frac{N_{O^+}}{N_{H^+} N_e^2} \frac{\partial N_e}{\partial q} + \frac{N_{O^+}}{N_e N_{H^+}^2} \frac{\partial N_e}{\partial q} \right)^\circ \quad (57)
\end{aligned}$$

$$\begin{aligned}
C_7 = & A_2 \frac{\partial}{\partial q} (A_2 D'_2) \left(\frac{1}{N_{H^+}} \frac{\partial N_{O^+}}{\partial q} \right)^\circ - A_2^2 D'_2 \left(\frac{1}{N_{H^+}^2} \frac{\partial N_{O^+}}{\partial q} \frac{\partial N_{H^+}}{\partial q} \right)^\circ \\
& + A_2^2 D'_2 \left(\frac{1}{N_{H^+}} \frac{\partial^2 N_{O^+}}{\partial q^2} \right)^\circ - A_2 A_3 D'_2 \left(\frac{1}{N_{H^+}} \frac{\partial N_{O^+}}{\partial q} \right)^\circ \\
& + A_2 \frac{\partial W_2}{\partial q} \left(\frac{N_{O^+}}{N_{H^+} N_e} \frac{\partial N_e}{\partial q} \right)^\circ - A_2 \frac{\partial V_2}{\partial q} \left(\frac{N_{O^+}}{N_{H^+}} \right)^\circ - A_2 V_2 \left(\frac{1}{N_{H^+}} \frac{\partial N_{O^+}}{\partial q} \right)^\circ \\
& + A_2 V_2 \left(\frac{N_{O^+}}{N_{H^+}^2} \frac{\partial N_{H^+}}{\partial q} \right)^\circ + A_3 V_2 \left(\frac{N_{O^+}}{N_{H^+}} \right)^\circ + A_2 W_2 \left(\frac{N_{O^+}}{N_{H^+} N_e} \frac{\partial^2 N_e}{\partial q^2} \right)^\circ \\
& + A_2 W_2 \left(\frac{1}{N_{H^+} N_e} \frac{\partial N_{O^+}}{\partial q} \frac{\partial N_e}{\partial q} \right)^\circ - A_2 W_2 \left(\frac{N_{O^+}}{N_e N_{H^+}^2} \frac{\partial N_{H^+}}{\partial q} \frac{\partial N_e}{\partial q} \right)^\circ \\
& - A_2 W_2 \left(\frac{N_{O^+}}{N_{H^+} N_e^2} \left(\frac{\partial N_e}{\partial q} \right)^2 \right)^\circ - A_3 W_2 \left(\frac{N_{O^+}}{N_{H^+} N_e} \frac{\partial N_e}{\partial q} \right)^\circ \\
& + P_\infty n(O) \exp(-\alpha(h, \chi)) \quad (58)
\end{aligned}$$

$$\nu_{O^+H^+} = \frac{0.077N_{H^+}}{T_{O^+H^+}^{3/2}} \quad (59)$$

$$\begin{aligned} \nu_{O^+n} = & 6.61 \times 10^{-11} n(H) T_{H^+}^{1/2} (1 - 0.047 \log_{10} T_{H^+})^2 + 1.32 \times 10^{-10} n(He) \\ & + 3.67 \times 10^{-11} n(O) T_r^{1/2} (1 - 0.064 \log_{10} T_r)^2 \\ & + 6.82 \times 10^{-10} n(N_2) + 6.64 \times 10^{-10} n(O_2) \end{aligned} \quad (60)$$

H^+

$$C_1 = A_2^2 D'_1 \left(\frac{1}{N_{O^+}} \right)^\circ + W_1 A_2 \left(\frac{N_{H^+}}{N_{O^+} N_e} \right)^\circ \quad (61)$$

$$\begin{aligned} C_2 = & A_2 u''_{O^+} \Delta_1 + A_2 \frac{\partial}{\partial q} (A_2 D'_1) \left(\frac{1}{N_{O^+}} \right)^\circ - A_2 A_3 D'_1 \left(\frac{1}{N_{O^+}} \right)^\circ \\ & + A_2 \frac{\partial W_1}{\partial q} \left(\frac{N_{H^+}}{N_{O^+} N_e} \right)^\circ - A_2 V_1 \frac{1}{N_{O^+}^\circ} + W_1 A_2 \left(\frac{1}{N_{O^+} N_e} \frac{\partial N_{H^+}}{\partial q} \right. \\ & \left. + \frac{1}{N_{O^+} N_e} \frac{\partial N_e}{\partial q} \right)^\circ - A_2 W_1 \left(\frac{N_{H^+}}{N_e N_{O^+}^2} \frac{\partial N_{O^+}}{\partial q} \right)^\circ - A_2 W_1 \left(\frac{2N_{H^+}}{N_{O^+} N_e^2} \frac{\partial N_e}{\partial q} \right)^\circ \\ & - A_3 W_1 \left(\frac{N_{H^+}}{N_{O^+} N_e} \right)^\circ + \frac{2 \cos \theta r_e^2 u_{th}}{r^3} - A_2^2 D'_1 \left(\frac{1}{N_{O^+}^2} \frac{\partial N_{O^+}}{\partial q} \right)^\circ \end{aligned} \quad (62)$$

$$\begin{aligned} C_3 = & -2.2 \times 10^{-11} T_{H^+}^{1/2} n(O) - \frac{\partial u_{\perp o}}{\partial r_e} \\ & - \frac{4u_{\perp o}}{r \sigma^2} (6 \cos^6 \theta - 3 \cos^4 \theta - 4 \cos^2 \theta + 1) - \left(\frac{1}{r \sin \theta} \frac{\partial u_\phi}{\partial \phi} \right)^\circ \\ & + A_2 \frac{\partial}{\partial q} (u''_{O^+} \Delta_1) + A_2 \frac{\partial W_1}{\partial q} \left(\frac{1}{N_{O^+} N_e} \frac{\partial N_e}{\partial q} - \frac{N_{H^+}}{N_{O^+} N_e^2} \frac{\partial N_e}{\partial q} \right)^\circ \\ & - A_2 \frac{\partial V_1}{\partial q} \left(\frac{1}{N_{O^+}} \right)^\circ + A_2 V_1 \left(\frac{1}{N_{O^+}^2} \frac{\partial N_{O^+}}{\partial q} \right)^\circ + A_3 V_1 \left(\frac{1}{N_{O^+}} \right)^\circ \\ & + A_2 W_1 \left(\frac{1}{N_{O^+} N_e} \frac{\partial^2 N_e}{\partial q^2} - \frac{N_{H^+}}{N_{O^+} N_e^2} \frac{\partial^2 N_e}{\partial q^2} \right)^\circ \\ & - A_2 W_1 \left(\frac{1}{N_{O^+} N_e^2} \frac{\partial N_{H^+}}{\partial q} \frac{\partial N_e}{\partial q} \right)^\circ - A_2 W_1 \left(\frac{1}{N_e N_{O^+}^2} \frac{\partial N_{O^+}}{\partial q} \frac{\partial N_e}{\partial q} \right)^\circ \end{aligned}$$

$$\begin{aligned}
& - \frac{N_{H^+}}{N_{O^+}^2 N_e^2} \frac{\partial N_{O^+}}{\partial q} \frac{\partial N_e}{\partial q} \Big)^\circ - A_2 W_1 \left(\frac{1}{N_{O^+} N_e^2} \left(\frac{\partial N_e}{\partial q} \right)^2 \right. \\
& \left. - \frac{2N_{H^+}}{N_{O^+} N_e^3} \left(\frac{\partial N_e}{\partial q} \right)^2 \right)^\circ - A_3 W_1 \left(\frac{1}{N_{O^+} N_e} \frac{\partial N_e}{\partial q} \right. \\
& \left. - \frac{N_{H^+}}{N_{O^+} N_e^2} \frac{\partial N_e}{\partial q} \right)^\circ + A_2 \frac{\partial}{\partial q} (u_{th} \sin I) - A_3 u_{th} \sin I \\
& - u''_{O^+} \Delta_1 A_3
\end{aligned} \tag{63}$$

$$C_4 = W_1 A_2 \left(\frac{N_{H^+}}{N_{O^+} N_e} \right)^\circ \tag{64}$$

$$\begin{aligned}
C_5 = & -A_2^2 D'_1 \left(\frac{1}{N_{O^+}^2} \frac{\partial N_{H^+}}{\partial q} \right)^\circ + A_2 \frac{\partial W_1}{\partial q} \left(\frac{N_{H^+}}{N_{O^+} N_e} \right)^\circ + A_2 V_1 \left(\frac{N_{H^+}}{N_{O^+}^2} \right)^\circ \\
& + A_2 W_1 \left(\frac{1}{N_{O^+} N_e} \frac{\partial N_{H^+}}{\partial q} \right)^\circ - A_2 W_1 \left(\frac{N_{H^+}}{N_e N_{O^+}^2} \frac{\partial N_{O^+}}{\partial q} + \frac{N_{H^+}}{N_e N_{O^+}^2} \frac{\partial N_e}{\partial q} \right)^\circ \\
& - A_2 W_1 \left(\frac{2N_{H^+}}{N_{O^+} N_e^2} \frac{\partial N_e}{\partial q} \right)^\circ - A_3 W_1 \left(\frac{N_{H^+}}{N_{O^+} N_e} \right)^\circ
\end{aligned} \tag{65}$$

$$\begin{aligned}
C_6 = & 2.5 \times 10^{-11} T_n^{1/2} n(H) - A_2 \frac{\partial}{\partial q} (A_2 D'_1) \left(\frac{1}{N_{O^+}^2} \frac{\partial N_{H^+}}{\partial q} \right)^\circ \\
& + A_2^2 D'_1 \left(\frac{2}{N_{O^+}^3} \frac{\partial N_{H^+}}{\partial q} \frac{\partial N_{O^+}}{\partial q} \right)^\circ - A_2^2 D'_1 \left(\frac{1}{N_{O^+}^2} \frac{\partial^2 N_{H^+}}{\partial q^2} \right)^\circ \\
& + A_2 A_3 D'_1 \left(\frac{1}{N_{O^+}^2} \frac{\partial N_{H^+}}{\partial q} \right)^\circ - A_2 \frac{\partial W_1}{\partial q} \left(\frac{N_{H^+}}{N_{O^+} N_e^2} \frac{\partial N_e}{\partial q} \right. \\
& \left. + \frac{N_{H^+}}{N_e N_{O^+}^2} \frac{\partial N_e}{\partial q} \right)^\circ + A_2 \frac{\partial V_1}{\partial q} \left(\frac{N_{H^+}}{N_{O^+}^2} \right)^\circ + A_2 V_1 \left(\frac{1}{N_{O^+}^2} \frac{\partial N_{H^+}}{\partial q} \right)^\circ \\
& - A_2 V_1 \left(\frac{2N_{H^+}}{N_{O^+}^3} \frac{\partial N_{O^+}}{\partial q} \right)^\circ - A_3 V_1 \left(\frac{N_{H^+}}{N_{O^+}^2} \right)^\circ - A_2 W_1 \left(\frac{N_{H^+}}{N_e N_{O^+}^2} \frac{\partial^2 N_e}{\partial q^2} \right. \\
& \left. + \frac{N_{H^+}}{N_{O^+} N_e^2} \frac{\partial^2 N_e}{\partial q^2} \right)^\circ - A_2 W_1 \left(\frac{1}{N_e N_{O^+}^2} \frac{\partial N_{H^+}}{\partial q} \frac{\partial N_e}{\partial q} \right. \\
& \left. + \frac{1}{N_{O^+} N_e^2} \frac{\partial N_{H^+}}{\partial q} \frac{\partial N_e}{\partial q} \right)^\circ + A_2 W_1 \left(\frac{N_{H^+}}{N_{O^+}^2 N_e^2} \frac{\partial N_{O^+}}{\partial q} \frac{\partial N_e}{\partial q} \right. \\
& \left. + \frac{2N_{H^+}}{N_e N_{O^+}^3} \frac{\partial N_{O^+}}{\partial q} \frac{\partial N_e}{\partial q} \right)^\circ + A_2 W_1 \left(\frac{N_{H^+}}{N_{O^+}^2 N_e^2} \left(\frac{\partial N_e}{\partial q} \right)^2 \right)
\end{aligned}$$

$$+ \frac{2N_{H^+}}{N_{O^+}N_e^3} \left(\frac{\partial N_e}{\partial q} \right)^2 \Big)^\circ + A_3 W_1 \left(\frac{N_{H^+}}{N_{O^+}N_e^2} \frac{\partial N_e}{\partial q} + \frac{N_{H^+}}{N_e N_{O^+}^2} \frac{\partial N_e}{\partial q} \right)^\circ \quad (66)$$

$$\begin{aligned} C_7 = & A_2 \frac{\partial}{\partial q} (A_2 D'_1) \left(\frac{1}{N_{O^+}} \frac{\partial N_{H^+}}{\partial q} \right)^\circ - A_2^2 D'_1 \left(\frac{1}{N_{O^+}^2} \frac{\partial N_{H^+}}{\partial q} \frac{\partial N_{O^+}}{\partial q} \right)^\circ \\ & + A_2^2 D'_1 \left(\frac{1}{N_{O^+}} \frac{\partial^2 N_{H^+}}{\partial q^2} \right)^\circ - A_2 A_3 D'_1 \left(\frac{1}{N_{O^+}} \frac{\partial N_{H^+}}{\partial q} \right)^\circ \\ & + A_2 \frac{\partial W_1}{\partial q} \left(\frac{N_{H^+}}{N_{O^+}N_e} \frac{\partial N_e}{\partial q} \right)^\circ - A_2 \frac{\partial V_1}{\partial q} \left(\frac{N_{H^+}}{N_{O^+}} \right)^\circ - A_2 V_1 \left(\frac{1}{N_{O^+}} \frac{\partial N_{H^+}}{\partial q} \right)^\circ \\ & + A_2 V_1 \left(\frac{N_{H^+}}{N_{O^+}^2} \frac{\partial N_{O^+}}{\partial q} \right)^\circ + A_3 V_1 \left(\frac{N_{H^+}}{N_{O^+}} \right)^\circ + A_2 W_1 \left(\frac{N_{H^+}}{N_{O^+}N_e} \frac{\partial^2 N_e}{\partial q^2} \right)^\circ \\ & + A_2 W_1 \left(\frac{1}{N_{O^+}N_e} \frac{\partial N_{H^+}}{\partial q} \frac{\partial N_e}{\partial q} \right)^\circ - A_2 W_1 \left(\frac{N_{H^+}}{N_e N_{O^+}^2} \frac{\partial N_{O^+}}{\partial q} \frac{\partial N_e}{\partial q} \right)^\circ \\ & - A_2 W_1 \left(\frac{N_{H^+}}{N_{O^+}N_e^2} \left(\frac{\partial N_e}{\partial q} \right)^2 \right)^\circ - A_3 W_1 \left(\frac{N_{H^+}}{N_{O^+}N_e} \frac{\partial N_e}{\partial q} \right)^\circ \end{aligned} \quad (67)$$

$$\nu_{H^+O^+} = \frac{1.23 N_{O^+}}{T_{O^+H^+}^{3/2}} \quad (68)$$

$$\begin{aligned} \nu_{H^+n} = & 2.65 \times 10^{-10} n(H) T_r^{1/2} (1 - 0.0831 \log_{10} T_r)^2 + 10.6 \times 10^{-10} n(He) \\ & + 6.61 \times 10^{-11} n(O) T_{H^+}^{1/2} (1 - 0.047 \log_{10} T_{H^+})^2 \\ & + 33.6 \times 10^{-10} n(N_2) + 32.0 \times 10^{-10} n(O_2) \end{aligned} \quad (69)$$

Electrons

Assuming charge neutrality, the electron number density is given by

$$N_e = N_{O^+} + N_{H^+}. \quad (70)$$

In addition, the assumption that there are no currents flowing parallel to B allows the parallel drift velocity for the electrons to be calculated from the drift velocities and number densities of the ions. The expression for the parallel,

electron drift velocity is

$$u_e'' = \frac{N_{O^+} u_{O^+}'' + N_{H^+} u_{H^+}''}{N_e}. \quad (71)$$

CHAPTER III

ENERGY EQUATIONS FOR O⁺, H⁺, AND ELECTRONS

The plasma heat balance equation for O⁺, H⁺, and electrons can be derived from the general form of the energy equation,

$$\frac{D}{Dt} \left(\frac{3p_s}{2} \right) + \frac{5}{2} p_s (\nabla \cdot \mathbf{u}_s) + \nabla \cdot \mathbf{q}_s + \boldsymbol{\tau}_s : \nabla \mathbf{u}_s = \frac{\delta \mathbf{E}_s}{\delta t} + \mathbf{Q}_s - \mathbf{L}_s \quad (72)$$

where $\frac{D}{Dt} = \frac{\partial}{\partial t} + \mathbf{u}_s \cdot \nabla$, the convective derivative of species, s; $p_s = n_s k T_s$, the partial pressure of species, s; n_s is the number density; k is Boltzmann's constant; T_s is the temperature; \mathbf{u}_s is the drift velocity; \mathbf{q}_s is the heat flow vector; $\boldsymbol{\tau}_s$ is the stress tensor; \mathbf{Q}_s is the heating rate; \mathbf{L}_s is the cooling rate; ∇ is the coordinate-space gradient; and $\frac{\delta \mathbf{E}_s}{\delta t}$ is the rate of energy exchange due to collisions. As in the continuity-momentum equation, we assume a displaced Maxwellian for the plasma. The approximate expression for the rate of energy exchange due to collisions for the 5-moment approach takes the form

$$\frac{\delta \mathbf{E}_s}{\delta t} = n_s m_s \sum_t \nu_{st} \frac{3k(T_t - T_s) \Psi_{st} + m_t (\mathbf{u}_s - \mathbf{u}_s)^2 \Phi_{st}}{m_s + m_t} \quad (73)$$

where Ψ_{st} and Φ_{st} are velocity dependent, correction factors and ν_{st} is the collision frequency for momentum transfer for species s and t.

Neglecting viscous effects and using the continuity equation in the form

$$\frac{\partial n_s}{\partial t} = -\text{div}(\mathbf{n}_s \mathbf{u}_s), \quad (74)$$

which is valid in a diffusion dominated region, and the definition of \mathbf{q}_s ,

$$\mathbf{q}_s = -\lambda_s \nabla T_s, \quad (75)$$

where λ_s is the thermal conductivity [Schunk, 1983], allows equation (72) to be

written in the form

$$\frac{3}{2} k n_s \frac{DT_s}{Dt} = Q'_s - k n_s T_s \operatorname{div} \mathbf{u}_s + \operatorname{div} (\lambda_s \nabla T_s) + F_{s,O} \quad (76)$$

where Q'_s is the net rate of heat gain due to collisions and $F_{s,O}$ is the frictional heating due to relative field-aligned motion between an ion and the neutral gas [Bailey et al., 1973]. The drift for a given species is again divided into its parallel and perpendicular components such that

$$\mathbf{u}_s = \mathbf{u}_s'' + \mathbf{u}_{em} \quad (77)$$

where \mathbf{u}_s'' is the parallel drift and \mathbf{u}_{em} is the electrodynamic drift [Sterling et al., 1969]. This frictional heating term has the form

$$F_{s,O} = \frac{m_O m_s}{m_O + m_s} n_s \nu_{s,O} (u_s'' - U \cos I)^2 \quad (78)$$

where $\nu_{s,O}$ is the collision frequency for momentum transfer between the ion and neutral species, U is the meridional component of the neutral wind velocity, and I is the magnetic dip angle. The collision term for O^+ is

$$\nu_{O+O} = 3.42 \times 10^{-11} n(O) T_r^{1/2} (1.04 - 0.064 \log_{10} T_r)^2 [s^{-1}] \quad (79)$$

and for H^+ it is

$$\nu_{H+O} = 6.61 \times 10^{-11} n(O) T_r^{1/2} (1 - 0.047 \log_{10} T_r)^2 [s^{-1}] \quad (80)$$

[Bailey and Heelis, 1980] where $T_r \approx \frac{1}{2} (T_{O+} + T_n)$ [Raitt et al., 1975]. Since the primary conduction of heat is parallel to \mathbf{B} ,

$$\operatorname{div} (\lambda_s \nabla T_s) = B \frac{\partial}{\partial s} \left(\frac{\lambda_s}{B} \frac{\partial}{\partial s} T_s \right) \quad (81)$$

where B is the earth's magnetic induction and s is the distance along the field line [Bailey et al., 1973]. Now,

$$\operatorname{div} (\mathbf{u}_s) = B \frac{\partial}{\partial s} \left(\frac{u_s''}{B} \right) + \operatorname{div} (\mathbf{u}_{em}) \quad (82)$$

and $\text{div}(\mathbf{u}_{em})$ is given by equations (44) and (45). We again assume the coordinate system is drifting at \mathbf{u}_{em} . Now, the time-dependent form of equation (76) is

$$\begin{aligned} \frac{3}{2}kn_s \left(\frac{DT_s}{Dt} + u_s'' \frac{\partial T_s}{\partial s} \right) &= Q'_s - kn_s T_s \left[B \frac{\partial}{\partial s} \frac{u_s''}{B} + \frac{\partial u_{\perp o}}{\partial r_e} + \frac{4u_{\perp o}}{r\sigma^2} \right. \\ &\quad \cdot \left(6\cos^6\theta - 3\cos^4\theta - 4\cos^2\theta + 1 \right) \\ &\quad \left. + \frac{1}{r\sin\theta} \frac{\partial u_\varphi}{\partial\varphi} \right] + B \frac{\partial}{\partial s} \frac{\lambda_s}{B} \frac{\partial T_s}{\partial s} \end{aligned} \quad (83)$$

[Bailey et al., 1973; Bailey and Heelis, 1980]. Using the definitions for \mathbf{B} ,

$$B(r, \theta) = \frac{B_o}{R^3} \sigma^{1/2}, \quad (84)$$

where B_o is 0.32×10^{-4} Teslas and $R = \frac{r}{r_e}$ [Hargreaves, 1979], $\frac{\partial}{\partial\theta}$,

$$\frac{\partial}{\partial s} = \sin I \frac{\partial}{\partial r} + \frac{\cos I}{r} \frac{\partial}{\partial\theta}, \quad (85)$$

[Baxter, 1964], and by realizing variations in the temperature of a given species in the r -direction are incorporated into the variations in the θ -direction, equation (80) can be expressed as

$$\begin{aligned} B \frac{\partial}{\partial s} \left(\frac{\lambda_s}{B} \frac{\partial T_s}{\partial s} \right) &= \frac{C_s T_s^{5/2}}{r_e^2 \sin^2\theta \sigma} \frac{\partial^2 T_s}{\partial\theta^2} + \frac{C_s T_s^{5/2}}{r_e^2 \sin^2\theta \sigma} \left(\frac{1}{C_s} \frac{\partial C_s}{\partial\theta} \right. \\ &\quad \left. + \frac{5}{2T_s} \frac{\partial T_s}{\partial\theta} + \frac{3\sin 2\theta}{\sigma} + 5\cot\theta \right) \frac{\partial T_s}{\partial\theta} \end{aligned} \quad (86)$$

where $\lambda_s = C_s T_s^{5/2}$ [Bailey et al., 1973]. Next, using the definition of a dipole field line, $r = r_e \sin^2\theta$ and previous assumptions, the field-aligned component of the second term on the right-hand side of equation (83) becomes

$$-kn_s T_s B \frac{\partial}{\partial s} \frac{u_s''}{B} = -\frac{kn_s T_s}{r_e \sin\theta \sigma^{1/2}} \left(\frac{\partial u_s''}{\partial\theta} + \frac{3\sin 2\theta u_s''}{2\sigma} + 6\cot\theta u_s'' \right). \quad (87)$$

Substituting (84) – (87) into equation (83), produces a nonlinear, second-order differential equation of the form

$$\frac{DT_s}{Dt} = A \frac{\partial^2 T_s}{\partial\theta^2} + B \frac{\partial T_s}{\partial\theta} + CT_s + D \quad (88)$$

where

$$A = \frac{2}{3kn_s} \left(\frac{C_s T_s^{5/2}}{r_e^2 \sin^2 \theta \sigma} \right), \quad (89)$$

$$B = \frac{2}{3kn_s} \frac{C_s T_s^{5/2}}{r_e^2 \sin^2 \theta \sigma} \left[\frac{5}{2T_s} \frac{\partial T_s}{\partial \theta} + \frac{3 \sin 2\theta}{\sigma} + 5 \cot \theta + \frac{1}{C_s} \frac{\partial C_s}{\partial \theta} - \left(\frac{r_e^2 \sin^2 \theta \sigma}{C_s T_s^{5/2}} \frac{3kn_s u_s''}{2r_e \sin \theta \sigma^{1/2}} \right) \right], \quad (90)$$

$$C = -\frac{2}{3} \left[\frac{1}{r_e \sin \theta \sigma^{1/2}} \left[\frac{\partial u_s''}{\partial \theta} + 6 \cot \theta u_s'' + \frac{3 \sin 2\theta}{2\sigma} u_s'' \right] + \frac{\partial u_{\perp o}}{\partial r_e} + \frac{4u_{\perp o}}{r_e \sin^2 \theta \sigma^2} (6 \cos^6 \theta - 3 \cos^4 \theta - 4 \cos^2 \theta + 1) + \frac{1}{r \sin \theta} \frac{\partial u_{\varphi}}{\partial \varphi} \right], \quad (91)$$

and for ions

$$D = (Q'_i + F_{s,O}) \frac{2}{3kn_s} \quad (92)$$

or for the electrons

$$D = Q'_e \frac{2}{3kn_s}. \quad (93)$$

Frictional heating due to collisions with the neutrals is ignored for the electrons. The expressions for the heat transfer terms are given below. For the ions, this expression is

$$Q'_{O^+} = Q_{O^+e} + Q_{O^+,H^+} + Q_{O^+,n}^{el} + Q_{O^+,H}^{in} \quad (94)$$

and

$$Q'_{H^+} = Q_{H^+e} + Q_{H^+,O^+} + Q_{H^+,n}^{el} + Q_{H^+,O}^{in}, \quad (95)$$

where Q_{se} is the heating rate due to elastic collisions of ion species, s , with the electrons, Q_{st} is the heating rate due to elastic collisions between ion species s and t , Q_{sn}^{el} is the heating rate due to elastic collisions with the neutrals, and

Q_{sn}^{in} is the heating rate due to inelastic collisions with the neutral oxygen or hydrogen. For the electrons, Q'_e is

$$Q'_e = Q_{eO^+} + Q_{eH^+} + Q_{f,st,O} + Q_h \quad (96)$$

where Q_{eO^+} is the electron heating rate due to collisions with O^+ , Q_{eH^+} is the electron heating rate due to collisions with H^+ , $Q_{f,st,O}$ is the electron heating rate due to fine structure excitation of neutral oxygen, and Q_h is the heating of the electron gas due to interactions with photoelectrons.

The collisional heating rate expressions for each species is presented below:

O^+

$$Q_{O^+e} = 4.8 \times 10^{-7} \frac{N_{O^+} N_e (T_e - T_{O^+})}{T_e^{3/2}} \quad (97)$$

$$Q_{O^+H^+} = 1.3 \times 10^{-3} \frac{N_{O^+} N_{H^+} (T_{H^+} - T_{O^+})}{(T_{O^+} + 16T_{H^+})^{3/2}} \quad (98)$$

$$Q_{O^+n}^{el} = N_{O^+} (T_n - T_{O^+}) \left[2.1 \times 10^{-15} (T_{O^+} + T_n)^{1/2} n(O) + 3.3 \times 10^{-14} n(H) + 6.6 \times 10^{-14} n(N_2) + 5.8 \times 10^{-14} n(O_2) + 2.8 \times 10^{-14} n(He) \right] \quad (99)$$

$$Q_{O^+H}^{in} = 3.8 \times 10^{-15} T_n^{1/2} n(H) N_{O^+} \left(\frac{8n(O) N_{H^+}}{9n(H) N_{O^+}} T_n^{1/2} T_{H^+}^{1/2} - T_{O^+} \right) \quad (100)$$

H^+

$$Q_{H^+e} = 4.8 \times 10^{-7} \cdot 16 N_{H^+} N_e \frac{T_e - T_{H^+}}{T_e^{3/2}} \quad (101)$$

$$Q_{H^+O^+} = 1.3 \times 10^{-3} N_{H^+} N_{O^+} \frac{T_{O^+} - T_{H^+}}{(T_{O^+} + 16T_{H^+})^{3/2}} \quad (102)$$

$$Q_{H^+n}^{el} = N_{H^+} (T_n - T_{H^+}) \left[1.4 \times 10^{-14} (T_{H^+} + T_n)^{1/2} n(H) + 3.5 \times 10^{-12} n(O) + 3.1 \times 10^{-14} n(N_2) + 2.8 \times 10^{-14} n(O_2) + 5.5 \times 10^{-14} n(He) \right] \quad (103)$$

$$Q_{H^+O}^{in} = \frac{8}{9} \cdot 3.8 \times 10^{-15} T_{H^+}^{1/2} n(O) N_{H^+} \left(\frac{9n(H) N_{O^+} T_n^{3/2}}{8n(O) N_{H^+} T_{H^+}^{1/2}} - T_{H^+} \right) \quad (104)$$

Electrons

$$Q_{eO^+} = 4.8 \times 10^{-7} \frac{N_{O^+} N_e (T_{O^+} - T_e)}{T_e^{3/2}} \quad (105)$$

$$Q_{eH^+} = 4.8 \times 10^{-7} \frac{16 N_{H^+} N_e (T_{H^+} - T_e)}{(T_e^{3/2})} \quad (106)$$

$$Q_{f,st,O} = 3 \times 10^{-12} n(O) \frac{T_n - T_e}{T_n} \quad (107)$$

[Bailey and Heelis, 1980]

The heating due to photoelectrons is obtained from an empirical representation of the heating rates obtained by Swartz *et al.* [1975].

$$Q_h = 10 ** (k_3 |\sin \lambda| Q_{eq} \epsilon) \quad (108)$$

where ϵ is the heating efficiency, λ is the geographic latitude,

$$k_3 = (r_e - h) k_4 + k_5, \quad (109)$$

and

$$Q_{eq} = (r_e - h) k_6 + k_7. \quad (110)$$

The constants are $k_4 = 6.64158 \times 10^{-3}$, $k_5 = 6.201753$, $k_6 = 2.44626 \times 10^{-3}$, and $k_7 = 2.1153846$.

The final step is to convert T_s to a variable γ_s , which is defined as

$$\gamma_s \equiv T_s^{5/2}, \quad (111)$$

and perform a time-varying Taylor's expansion to produce a linear (in terms of γ_s), second-order differential equation of the form,

$$\frac{D\gamma_s}{Dt} = A'' \frac{\partial^2 \gamma_s}{\partial \theta^2} + B'' \frac{\partial \gamma_s}{\partial \theta} + C'' \gamma_s + D'' \quad (112)$$

where for

O^+

$$A'' = \frac{2C_{O^+}}{3kN_{O^+}r_e^2 \sin^2 \theta \sigma} (\gamma_{O^+})_o^{5/7}, \quad (113)$$

$$B'' = -\frac{10}{7} \frac{A'}{(\gamma_{O^+})_o^{2/7}} \left(\frac{\partial \gamma_{O^+}}{\partial \theta} \right)_o + 7 \frac{C_2}{(\gamma_{O^+})_o^{2/7}} \left(\frac{\partial \gamma_{O^+}}{\partial \theta} \right)_o + C_1 (\gamma_{O^+})_o^{5/7} - \frac{7}{2} C_8 \quad (114)$$

$$C'' = \frac{5A'}{7(\gamma_{O^+})_o^{9/7}} \left(\frac{\partial \gamma_{O^+}}{\partial \theta} \right)_o^2 - \frac{7C_2}{2(\gamma_{O^+})_o^{9/7}} \left(\frac{\partial \gamma_{O^+}}{\partial \theta} \right)_o^2 + \frac{5C_8}{2(\gamma_{O^+})_o} \left(\frac{\partial \gamma_{O^+}}{\partial \theta} \right)_o \\ + C - C_9 - C_{10} - \frac{2C_3}{3k} - C_5 \quad (115)$$

$$D'' = \frac{5C}{2} (\gamma_{O^+})_o - \frac{5C_9}{2} (\gamma_{O^+})_o - \frac{5C_{10}}{2} (\gamma_{O^+})_o - \frac{5C_3}{3k} (\gamma_{O^+})_o \\ - \frac{5C_5}{2} (\gamma_{O^+})_o + C_{11} - \frac{5C_8}{2} \left(\frac{\partial \gamma_{O^+}}{\partial \theta} \right)_o \quad (116)$$

$$A' = \frac{2C_{O^+}}{3kN_{O^+}r_e^2 \sin^2 \theta \sigma} \quad (117)$$

$$C_1 = \frac{2C_{O^+}}{3kN_{O^+}r_e^2 \sin^2 \theta \sigma} \left(\frac{3 \sin 2\theta}{\sigma} + 5 \cot \theta + \frac{1}{C_{O^+}} \frac{\partial C_{O^+}}{\partial \theta} \right) \quad (118)$$

$$C_2 = \frac{20C_{O^+}}{147kN_{O^+}r_e^2 \sin^2 \theta \sigma} \quad (119)$$

$$C_3 = 2.1 \times 10^{-15} ((T_{O^+})_o + T_n)^{1/2} n(O) + 3.3 \times 10^{-14} n(H) + 6.6 \times 10^{-14} n(N_2) \\ + 5.8 \times 10^{-14} n(O_2) + 2.8 \times 10^{-14} n(He) \quad (120)$$

$$C_4 = \frac{8}{9} \left(\frac{7.6 \times 10^{-15} T_n N_{H^+} n(O) T_{H^+}^{1/2}}{3kN_{O^+}} \right) \quad (121)$$

$$C_5 = \frac{7.6 \times 10^{-15} T_n^{1/2} n(H)}{3k} \quad (122)$$

$$C_6 = \frac{m_O m_{O+} (u''_{O+} - U \cos I)^2}{k (m_O + m_{O+})} - 2.28 \times 10^{-11} n(O) T_r^{1/2} (1.04 - 0.064 \log_{10} T_r)^2 \quad (123)$$

$$C_7 = C_4 + \frac{3.2 \times 10^{-7} N_e}{k T_e^{1/2}} + \frac{2.6 \times 10^{-3} N_{H+} T_{H+}}{3k [(T_{O+})_o + 16T_{H+}]^{3/2}} + \frac{3C_3 T_n}{3k} + C_6 \quad (124)$$

$$C_8 = \frac{2u''_{O+}}{7r_e \sin \theta \sigma^{1/2}} \quad (125)$$

$$C_9 = \frac{3.2 \times 10^{-7} N_e}{k T_e^{3/2}} \quad (126)$$

$$C_{10} = \frac{2.6 \times 10^{-3} N_{H+}}{3k [(T_{O+})_o + 16T_{H+}]^{3/2}} \quad (127)$$

$$C_{11} = \frac{7}{2} (\gamma_{O+})_o^{5/7} C_7 \quad (128)$$

$$\lambda_{O+} = \frac{1.2 \times 10^4 N_{O+} T_{O+}^{5/2}}{N_e} \left[\frac{eV}{cm - sec - ^\circ K} \right] \quad (129)$$

H⁺

$$A'' = \frac{2C_{H+}}{3k N_{H+} r_e^2 \sin^2 \theta \sigma} (\gamma_{H+})_o^{5/7}, \quad (130)$$

$$B'' = -\frac{10}{7} \frac{A'}{(\gamma_{H+})_o^{2/7}} \left(\frac{\partial \gamma_{H+}}{\partial \theta} \right)_o + 7 \frac{C_2}{(\gamma_{H+})_o^{2/7}} \left(\frac{\partial \gamma_{H+}}{\partial \theta} \right)_o + C_1 (\gamma_{H+})_o^{5/7} - \frac{7}{2} C_8 \quad (131)$$

$$C'' = \frac{5A'}{7(\gamma_{H+})_o^{9/7}} \left(\frac{\partial \gamma_{H+}}{\partial \theta} \right)_o^2 - \frac{7C_2}{2(\gamma_{H+})_o^{9/7}} \left(\frac{\partial \gamma_{H+}}{\partial \theta} \right)_o^2 + \frac{5C_8}{2(\gamma_{H+})_o} \left(\frac{\partial \gamma_{H+}}{\partial \theta} \right)_o + C - 16C_9 - C_{10} - \frac{2C_3}{3k} + \frac{3C_5}{2} (\gamma_{H+})_o^{1/7} \quad (132)$$

$$D'' = -\frac{5C_8}{2} \left(\frac{\partial \gamma_{H+}}{\partial \theta} \right)_o + \frac{5C}{2} (\gamma_{H+})_o - \frac{5C_{10}}{2} (\gamma_{H+})_o - \frac{5C_3}{3k} (\gamma_{H+})_o + 2C_5 (\gamma_{H+})_o^{8/7} + C_{11} - 40C_9 (\gamma_{H+})_o \quad (133)$$

$$A' = \frac{2C_{H^+}}{3kN_{H^+}r_e^2 \sin^2 \theta \sigma} \quad (134)$$

$$C_1 = \frac{2C_{H^+}}{3kN_{H^+}r_e^2 \sin^2 \theta \sigma} \left(\frac{3 \sin 2\theta}{\sigma} + 5 \cot \theta + \frac{1}{C_{H^+}} \frac{\partial C_{H^+}}{\partial \theta} \right) \quad (135)$$

$$C_2 = \frac{20C_{H^+}}{147kN_{H^+}r_e^2 \sin^2 \theta \sigma} \quad (136)$$

$$\begin{aligned} C_3 = & 1.4 \times 10^{-14} ((T_{H^+})_o + T_n)^{1/2} n(H) + 3.5 \times 10^{-12} n(O) + 3.1 \times 10^{-14} n(N_2) \\ & + 2.8 \times 10^{-14} n(O_2) + 5.5 \times 10^{-14} n(He) \end{aligned} \quad (137)$$

$$C_4 = \frac{7.6 \times 10^{-15} T_n^{3/2} N_{O^+} n(H)}{3kN_{H^+}} \quad (138)$$

$$C_5 = -\frac{8}{9} \left(\frac{7.6 \times 10^{-15} n(O)}{3k} \right) \quad (139)$$

$$\begin{aligned} C_6 = & \frac{2}{3} \left(\frac{m_O m_{H^+} (u''_{H^+} - U \cos I)^2}{k(m_O + m_{H^+})} \right) 6.61 \times 10^{-11} n(O) T_r^{1/2} \\ & \cdot (1.0 - 0.047 \log_{10} T_r)^2 \end{aligned} \quad (140)$$

$$C_7 = C_4 + 16 \frac{3.2 \times 10^{-7} N_e}{kT_e^{1/2}} + \frac{2.6 \times 10^{-3} N_{O^+} T_{O^+}}{3k [(T_{O^+})_o + 16T_{H^+}]^{3/2}} + C_6 + \frac{2C_3 T_n}{3k} \quad (141)$$

$$C_8 = \frac{2u''_{H^+}}{7r_e \sin \theta \sigma^{1/2}} \quad (142)$$

$$C_9 = \frac{3.2 \times 10^{-7} N_e}{kT_e^{3/2}} \quad (143)$$

$$C_{10} = \frac{2.6 \times 10^{-3} N_{O^+}}{3k [T_{O^+} + 16(T_{H^+})_o]^{3/2}} \quad (144)$$

$$C_{11} = \frac{7}{2} (\gamma_{H^+})_o^{5/7} C_7 \quad (145)$$

$$\lambda_{H^+} = \frac{4.8 \times 10^4 N_{H^+} T_{H^+}^{5/2}}{N_e} \left[\frac{eV}{cm - sec - ^\circ K} \right] \quad (146)$$

Electrons

$$A'' = \frac{2C_e}{3kN_e r_e^2 \sin^2 \theta \sigma} (\gamma_e)_o^{5/7}, \quad (147)$$

$$B'' = -\frac{10}{7} \frac{A'}{(\gamma_e)_o^{2/7}} \left(\frac{\partial \gamma_e}{\partial \theta} \right)_o + 7 \frac{C_2}{(\gamma_e)_o^{2/7}} \left(\frac{\partial \gamma_e}{\partial \theta} \right)_o + C_1 (\gamma_e)_o^{5/7} - \frac{7}{2} C_8 \quad (148)$$

$$\begin{aligned} C'' = & \frac{5A'}{7(\gamma_e)_o^{9/7}} \left(\frac{\partial \gamma_e}{\partial \theta} \right)_o^2 - \frac{7C_2}{2(\gamma_e)_o^{9/7}} \left(\frac{\partial \gamma_e}{\partial \theta} \right)_o^2 + \frac{5C_8}{2(\gamma_e)_o} \left(\frac{\partial \gamma_e}{\partial \theta} \right)_o \\ & + C - \frac{3C_3 T_{O^+}}{2(\gamma_e)_o^{5/7}} + \frac{C_3}{2(\gamma_e)_o^{3/7}} - \frac{3C_4 T_{H^+}}{2(\gamma_e)_o^{5/7}} + \frac{C_4}{2(\gamma_e)_o^{3/7}} - \frac{C_5}{T_n} \end{aligned} \quad (149)$$

$$\begin{aligned} D'' = & -\frac{5C_8}{2} \left(\frac{\partial \gamma_e}{\partial \theta} \right)_o + \frac{5C}{2} (\gamma_e)_o + 5C_3 T_{O^+} (\gamma_e)_o^{2/7} - 4C_3 (\gamma_e)_o^{4/7} \\ & + 5C_4 T_{H^+} (\gamma_e)_o^{2/7} - 4C_4 (\gamma_e)_o^{4/7} + \frac{7C_5}{2} (\gamma_e)_o^{5/7} - \frac{5C_5}{2T_n} (\gamma_e)_o \\ & + \frac{7Q_h}{3kN_e} (\gamma_e)_o^{5/7} \end{aligned} \quad (150)$$

$$A' = \frac{2C_e}{3kN_e r_e^2 \sin^2 \theta \sigma} \quad (151)$$

$$C_1 = \frac{2C_e}{3kN_e r_e^2 \sin^2 \theta \sigma} \left(\frac{3 \sin 2\theta}{\sigma} + 5 \cot \theta + \frac{1}{C_e} \frac{\partial C_e}{\partial \theta} \right) \quad (152)$$

$$C_2 = \frac{20C_e}{147kN_e r_e^2 \sin^2 \theta \sigma} \quad (153)$$

$$C_3 = \frac{3.2 \times 10^{-7} N_{O^+}}{k} \quad (154)$$

$$C_4 = \frac{3.2 \times 10^{-7} \cdot 16 N_{H^+}}{k} \quad (155)$$

$$C_5 = \frac{2 \times 10^{-12} n(O)}{k} \quad (156)$$

$$C_8 = \frac{2u_e''}{7r_e \sin \theta \sigma^{1/2}} \quad (157)$$

$$\lambda_e = 7.5 \times 10^5 T_e^{5/2} \left[\frac{eV}{cm - sec - ^\circ K} \right]. \quad (158)$$

CHAPTER IV

RESULTS AND DISCUSSION

Boundary Conditions

Before the continuity-momentum equation or the energy equation can be solved numerically, appropriate boundary conditions must be specified. For our model, these boundary conditions are the number densities for H^+ and O^+ , and the temperatures of H^+ , O^+ , and the electrons at the ends of the field line in conjugate hemispheres. This is fortuitous since densities at and below the F_2 peak have been measured and studied for over 40 years through the use of ionosondes. In addition, ion and electron temperatures in the F -region have been measured using incoherent backscatter radars for over 30 years [Raitt, 1988]. Incoherent radar facilities at Arecibo, Puerto Rico (dip latitude = $30^\circ N$) and Jicamarca, Peru (dip latitude = $1^\circ N$) regularly monitor the low-latitude ionosphere [Schunk and Nagy, 1980]. At high latitudes, the field line can be assumed to be nearly vertical, and the appropriate boundary conditions are the density/temperature at the base of the field line and a flux at the top of the field line. Because these fluxes are not well known, we feel our model both includes the important physical processes and utilizes boundary conditions that can be more accurately specified.

Our boundary conditions are: (a) $T(O^+)$, $T(H^+) = T_n$ at both ends, (b) $T_e = 1525^\circ K$, (c) $N(O^+) = 1 \times 10^4$, and (d) $N(H^+) = 10$. Our values for T_e are based on a synthesis of previous model results, results from IRI, and published observations. Boundary values are somewhat arbitrary since they only affect the exterior points in the array.

Inputs

To specify the neutral atmosphere, the electric field, and the neutral winds for varying levels of solar activity, several inputs are required by the MSIS model, the electric field model [Richmond *et al.*, 1980], and our neutral wind model. The geographic equivalents of the points along a given field line are determined using subroutine GGM from the International Reference Ionosphere (IRI) model. Since our calculations are organized in magnetic coordinates and time is organized in geographic coordinates, we assume the input time (local or universal) is valid for the northernmost point on the field line and allow time to vary along the field line. This variation is in accordance with the change in geographic longitude as magnetic colatitude increases. In addition, we assume quiet magnetic conditions. For sunspot minimum conditions, the sunspot number utilized in equation (16) is zero ($P_\infty = 1.1 \times 10^{-7}$) and the 10.7 cm flux is 70; for solar maximum conditions, the sunspot number would be 161, corresponding to $P_\infty = 3.3 \times 10^{-7}$, and the 10.7 cm flux is assumed to be 200. See Figure 6 for results from MSIS86 for sunspot minimum conditions along a field line with an equatorial crossing altitude of 1000 km. Figure 6a shows densities for the northern hemisphere portion of the field line for equinox conditions (Julian day = 80). The southern hemisphere profile (not shown) exhibits little variation from the results in the northern hemisphere. Figure 6b is valid for June solstice (Julian day = 171) conditions, but once again there is little variation between hemispheres or between solstice and equinox densities.

Based on previous calculations, estimates from IRI, and observations, our chosen value for ϵ in equation (109) is $\epsilon = .22$. It should be emphasized that ϵ is multiplied times the logarithm of the Q_h . Since our expression for heating due to the photoelectrons is highly empirical, no physical significance is attached to this choice.

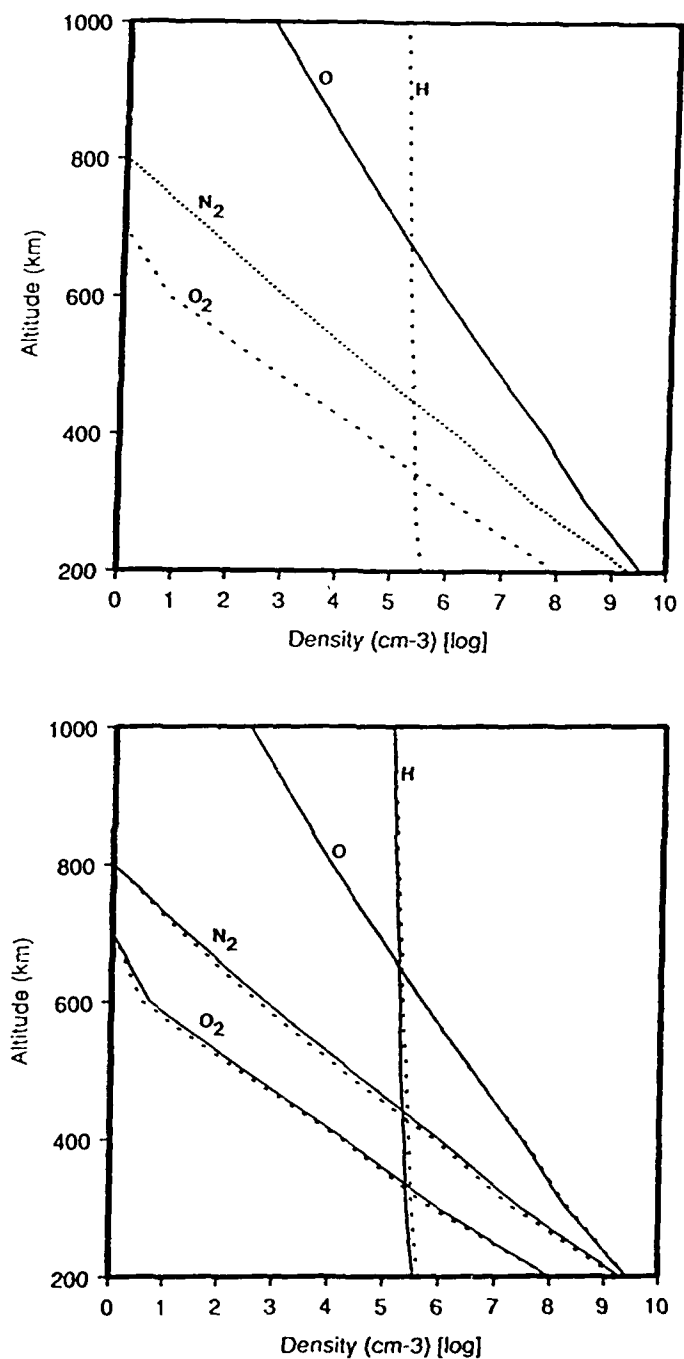


Figure 6. Results from the MSIS86 empirical model for a dipole field line with an equatorial crossing altitude of 1000 km. The profiles are valid for solar minimum conditions at 0° magnetic longitude at noon for quiet magnetic conditions. The profiles show densities along the field line for: (a) equinox, northern hemisphere only and (b) June solstice. The dashed lines are southern hemisphere profiles and the solid lines are northern hemisphere profiles.

Results

Since the focus of this thesis is the development of a theoretical model of the topside, low-latitude ionosphere, presentation of results will be confined to demonstrating the model's ability to reproduce physical processes in a reasonable manner. It is assumed that if the physical processes are handled correctly, global or regional modelling of the low-latitude ionosphere is a straightforward application.

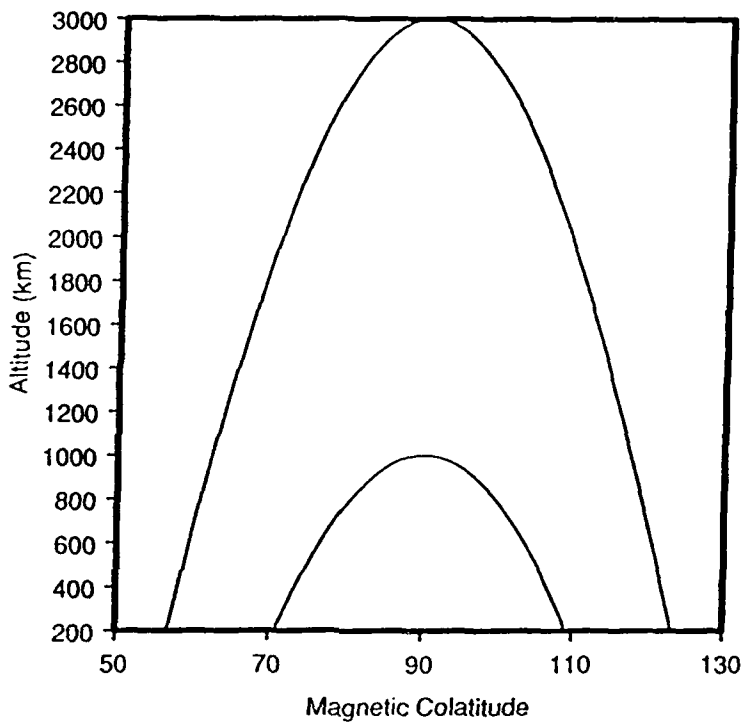


Figure 7. Dipole field lines with equatorial crossing altitudes of 1000 km and 3000 km.

Figure 7 shows the two field lines being considered. As previously noted, field lines at these latitudes are inclined to the vertical and become horizontal at the magnetic equator. It is this inclination of the field lines that contributes to the behavior of the low-latitude ionosphere. Note that the field line with

an equatorial altitude of 1000 km intersects 200 km at $\pm 18^\circ$ magnetic latitude, and the field line crossing the equator at 3000 km intersects 200 km at $\pm 33^\circ$ magnetic latitude.

As a test of the model, solar minimum conditions for March equinox and June solstice were chosen. Most results are for the field line with an equatorial crossing altitude of 1000 km ($1.16 R_e$) at 0° magnetic longitude. However, results for a field line with an equatorial crossing altitude of 3000 km are also shown for comparison. All profiles represent a steady state solution of the model for local noon (at the northernmost point) during quiet magnetic conditions.

Figure 8 shows model calculations for equinox when neutral wind effects, electrodynamic drift, and adiabatic effects are ignored. The F_2 peak occurs at an altitude of about 300 km with a peak density of $2.5 \times 10^5 \text{ cm}^{-3}$. O^+ remains the dominant ion up to an altitude of 720 km, which is the approximate O-H transition height. The profiles are fairly symmetric about the equator with the minimum in O^+ density being displaced slightly into the northern hemisphere due, perhaps, to the slight asymmetry in the neutral atmosphere. At the magnetic equator, O^+ densities drop to $5 \times 10^3 \text{ cm}^{-3}$ and the H^+ density increases to $1 \times 10^4 \text{ cm}^{-3}$. The temperatures of the ions and electrons increase with height above the F_2 peak and reach maxima of 2750°K for the electrons, 2500°K for the H^+ ions, and 2472°K for the O^+ ions. Below the F_2 peak, the ions cool to the neutral temperature due to the frequent collisions with the neutrals, which act as a heat sink. The electron temperature shows a minimum at the F_2 peak because there exists a direct relationship between the electron density and electron temperature. The more numerous the ambient electron density, the less heat an individual electron receives from the photoelectrons. This case will serve as a reference for comparison.

Figure 9 shows model calculations for solstice conditions. Although, it's not readily apparent, careful examination reveals that densities have decreased

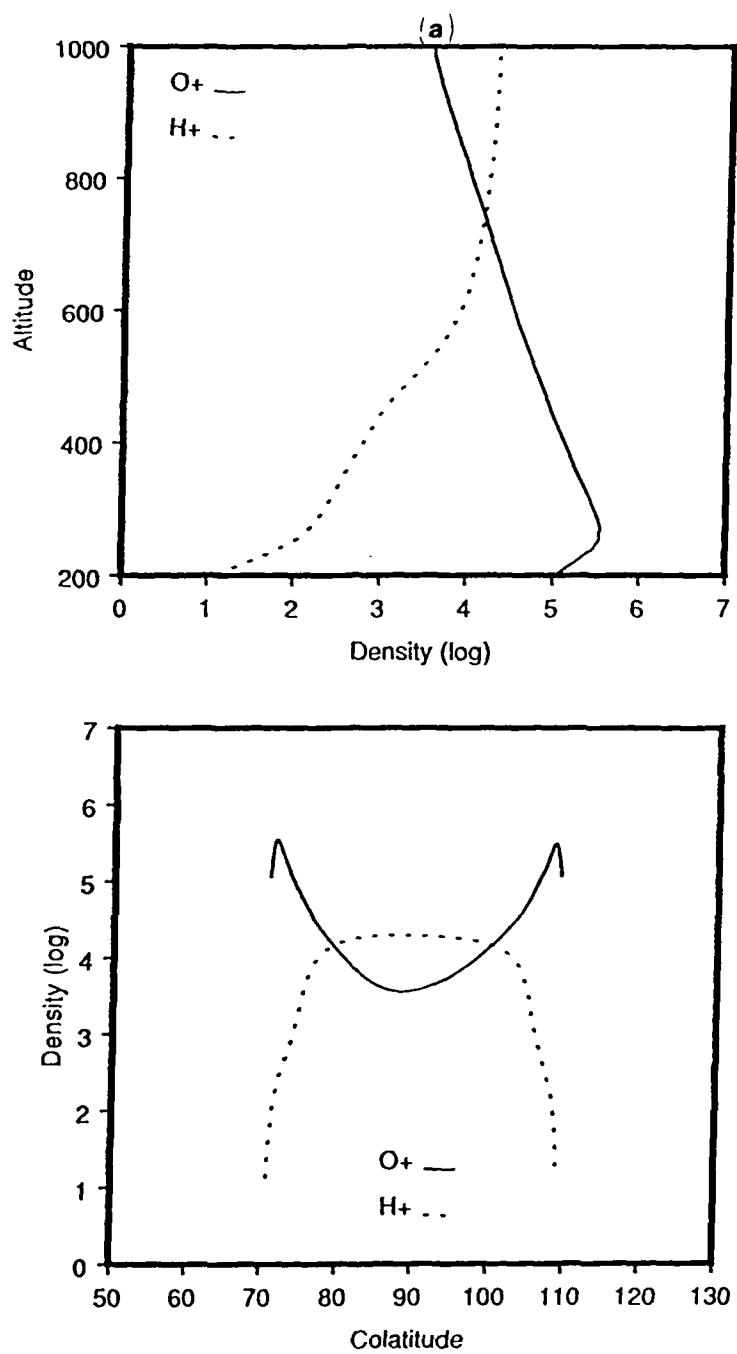


Figure 8. Plasma (a) densities and (b) temperatures along a magnetic field line with an equatorial crossing altitude of 1000 km for equinox and solar minimum conditions and 0° magnetic longitude. Electrodynamic, neutral wind, and adiabatic effects are neglected.

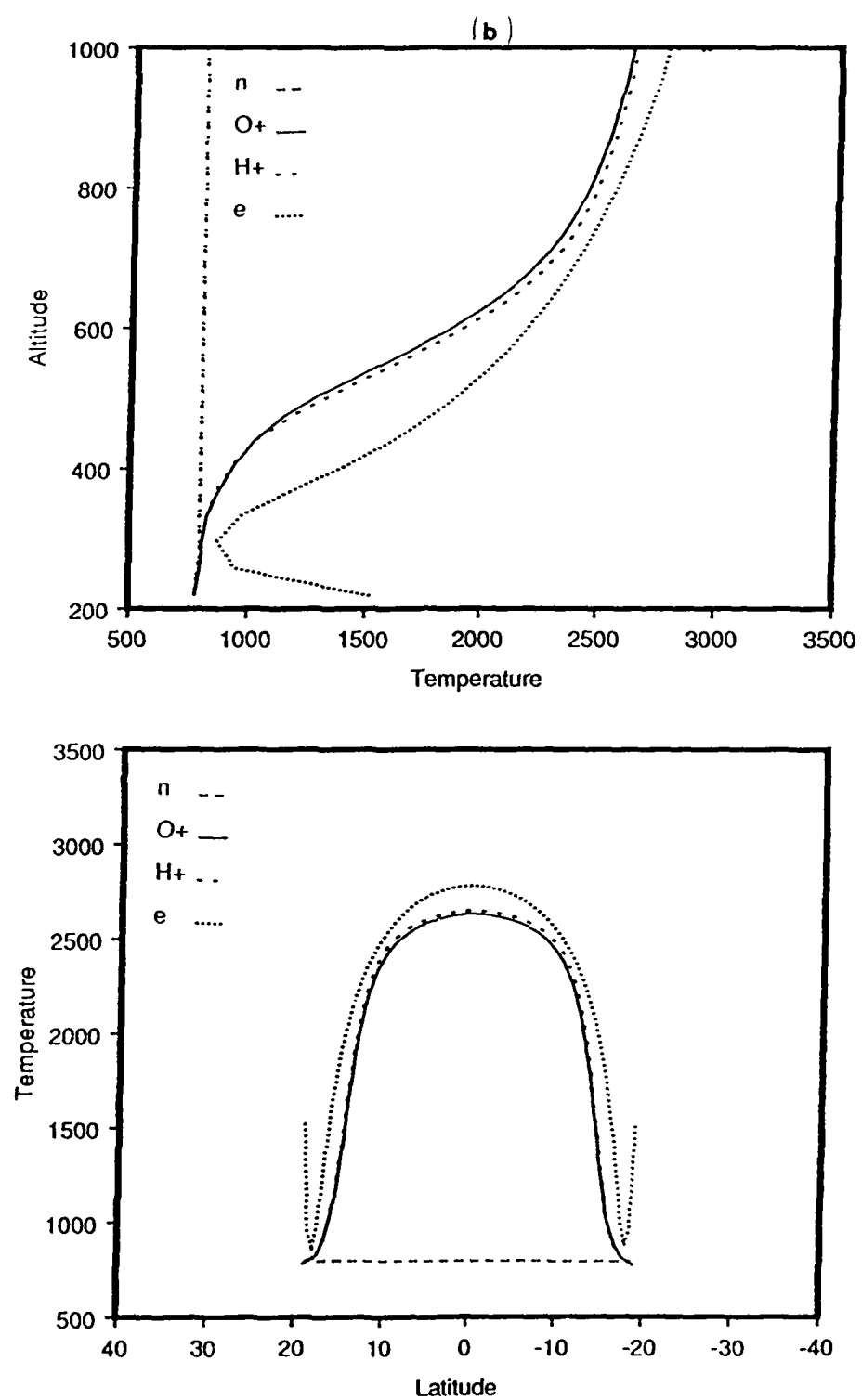


Figure 8. (cont.)

slightly along the bulk of the field line when compared to the equinox case. Densities in the southern hemisphere F_2 peak have decreased considerably less than in the northern hemisphere. H^+ densities remained unchanged in the northern hemisphere, but increased along the field line in the southern hemisphere. Associated with this decrease in density, ion and electron temperatures have increased in both hemispheres below 600 km. The increase in ion temperature results directly from the increase in electron temperature and indirectly as a result of the density change. The $O^+ - H^+$ transition height has decreased about 50 km for solstice conditions. This comparison between Figures 8 and 9 demonstrate that the asymmetry between northern and southern hemisphere F -regions is not due to asymmetries in the neutral atmosphere or differing solar zenith angles.

Now that the characteristics of the reference profiles have been established, it is possible to evaluate the relative effects of other processes. The first process to be considered is the electrodynamic drift, which is about 2 meters/second at the equator (They are assumed to decrease with distance away from the equator.). Results from our model with these effects included are shown in Figure 10 for equinox conditions and Figure 11 for solstice conditions. Neutral wind effects and adiabatic effects due to field-aligned flow are neglected. When $E \times B$ effects are included, the O^+ and H^+ densities are decreased above 340 km, but increase slightly between the F_2 peak and 340 km. Depletions in plasma density are greatest at the magnetic equator. This effect is consistent with models of the formation of the Appleton anomaly where plasma drifts upward at the equator due to electrodynamic forces and then diffuses down the field lines forming regions of enhanced plasma density at $\pm 16^\circ$ [Anderson, 1973b]. The $O^+ - H^+$ transition height is raised about 65 km. The electron and ion temperatures decrease 30–50°K due to adiabatic expansion of the plasma.

Figure 12 contains profiles of density and temperature from the field line with an equatorial crossing altitude of 3000 km ($1.47 R_e$) at 0° magnetic longitude

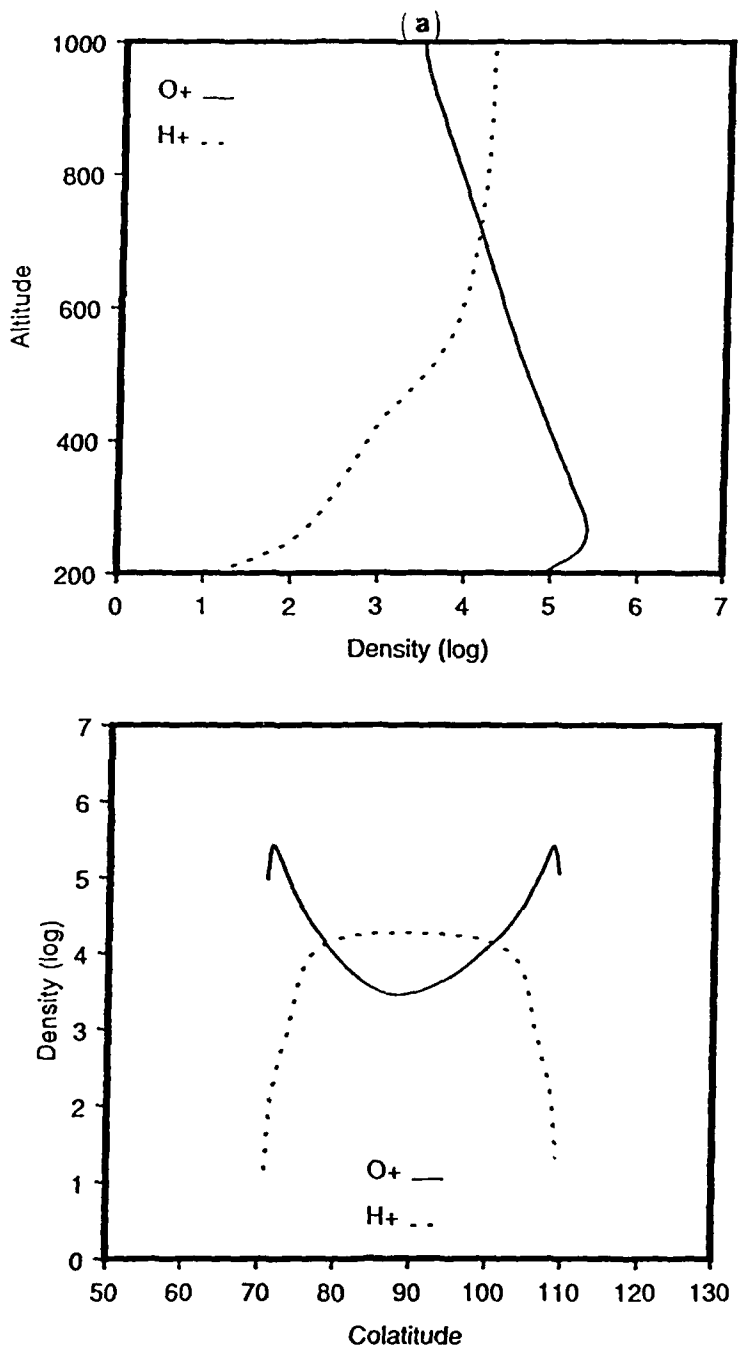


Figure 9. Plasma (a) densities and (b) temperatures along a magnetic field line with an equatorial crossing altitude of 1000 km for solstice and solar minimum conditions and 0° magnetic longitude. Electrodynamic, neutral wind, and adiabatic effects are neglected.

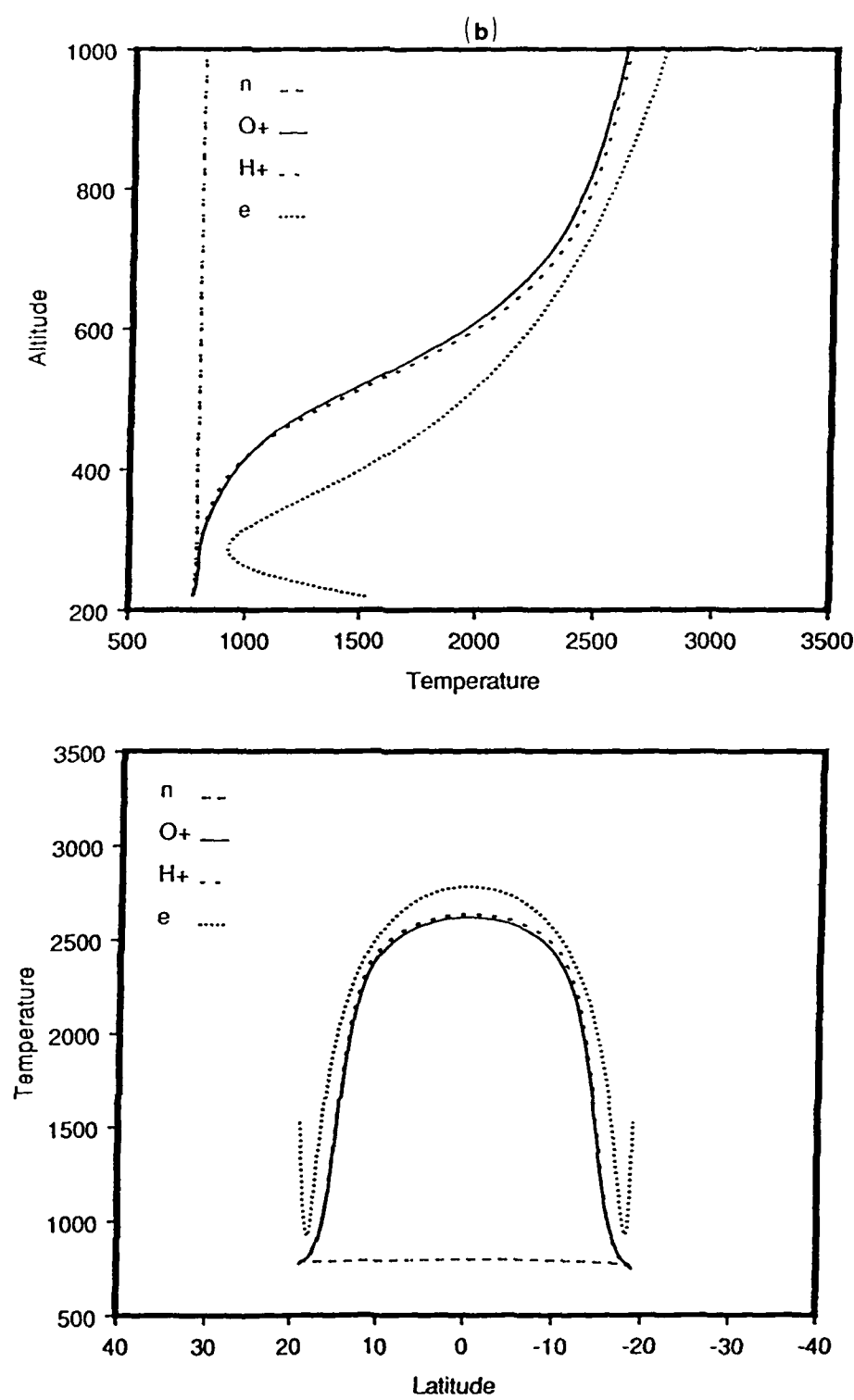


Figure 9. (cont.)

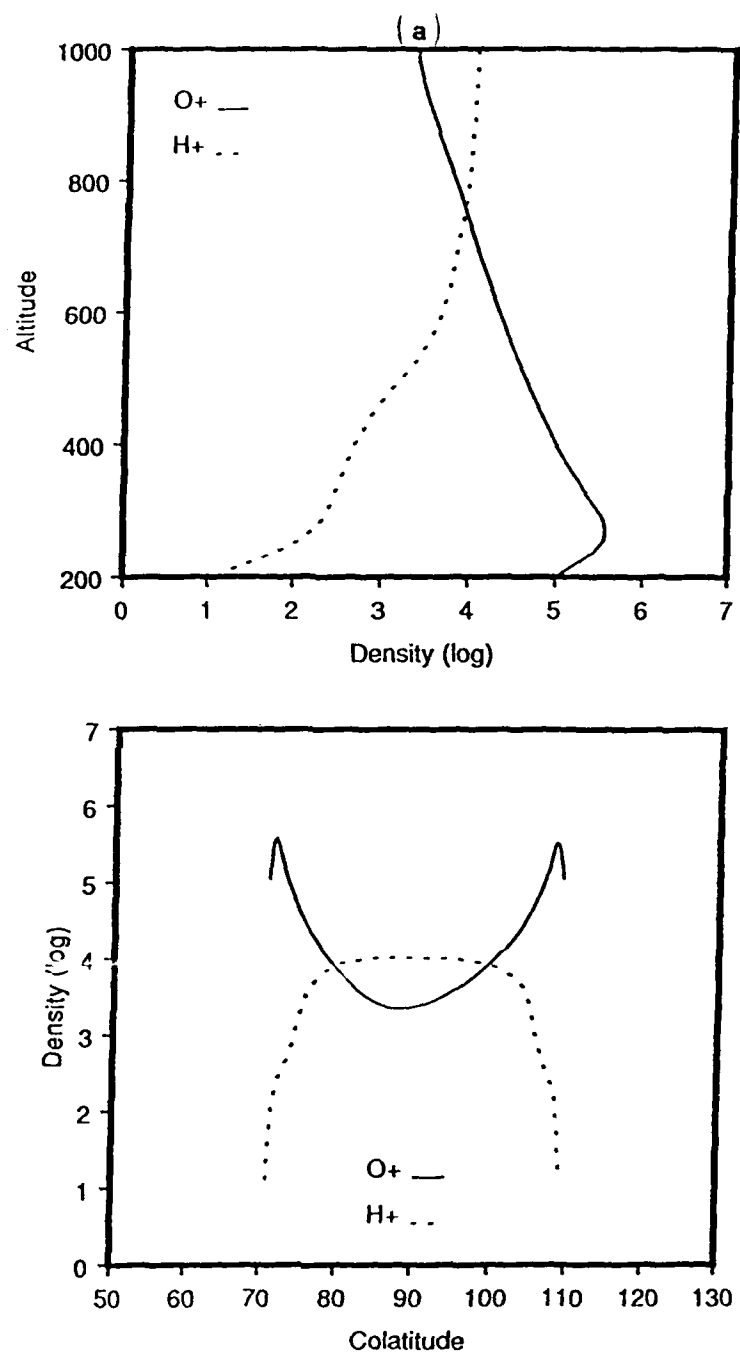


Figure 10. Plasma (a) densities and (b) temperatures along a magnetic field line with an equatorial crossing altitude of 1000 km for equinox and solar minimum conditions and 0° magnetic longitude. Neutral wind and adiabatic effects are neglected. Electrodynamic effects are included.

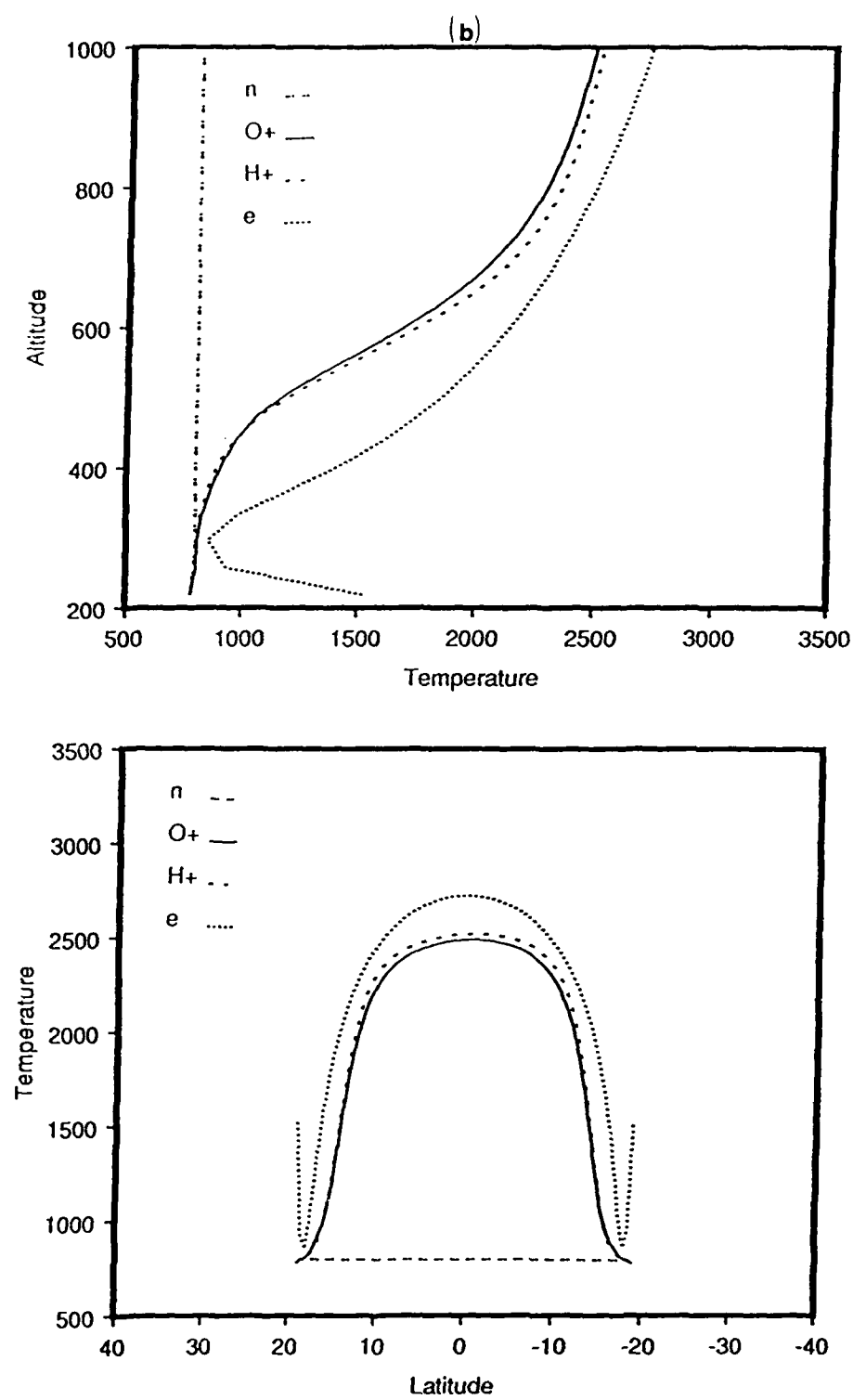


Figure 10. (cont.)

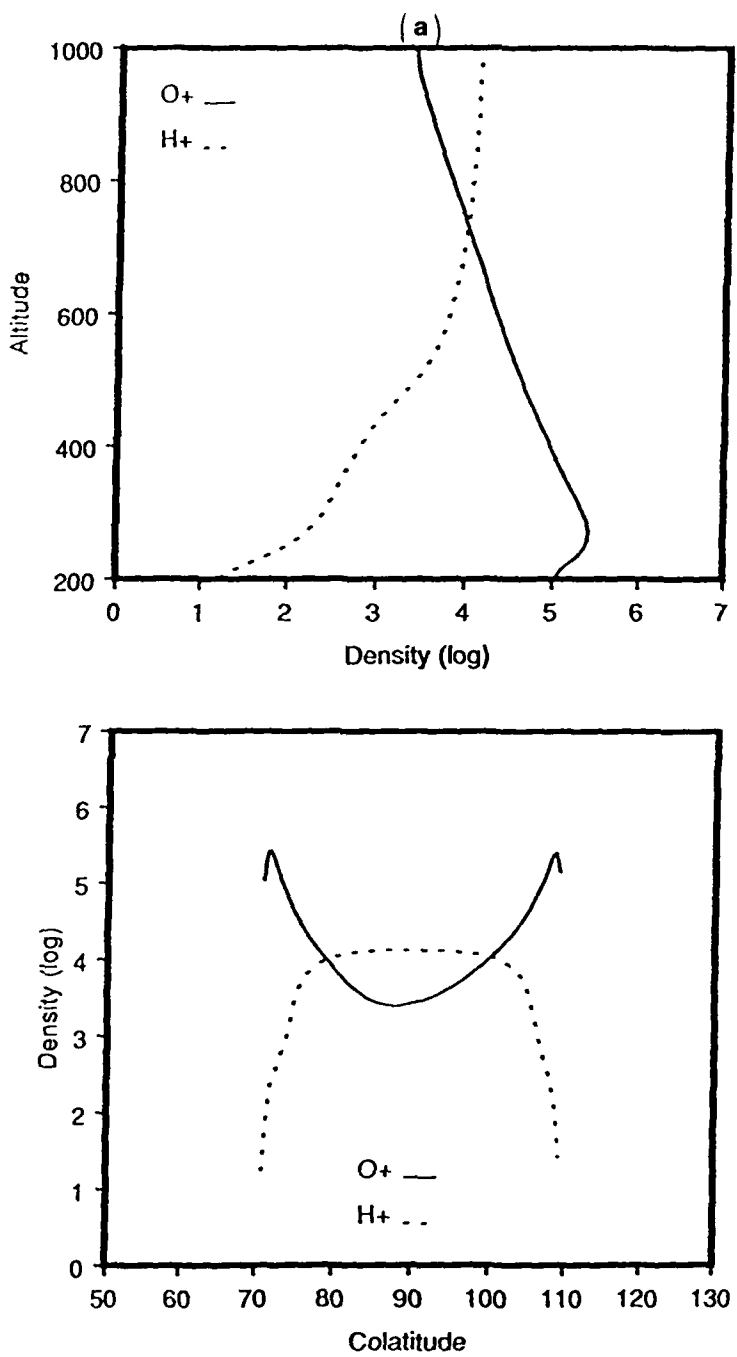


Figure 11. Plasma (a) densities and (b) temperatures along a magnetic field line with an equatorial crossing altitude of 1000 km for solstice and solar minimum conditions and 0° magnetic longitude. Neutral wind and adiabatic effects are neglected. Electrodynamic drifts included.

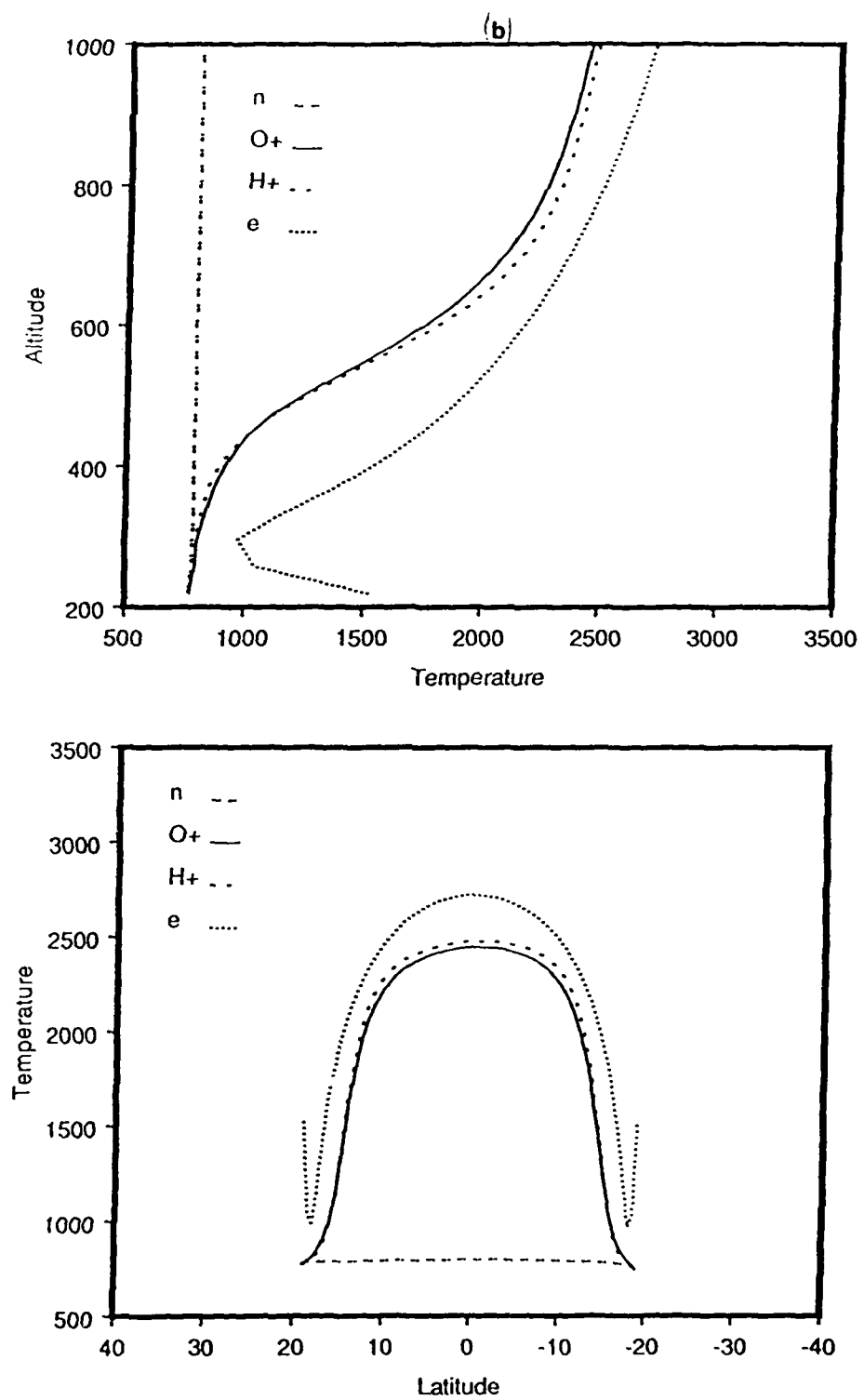


Figure 11. (cont.)

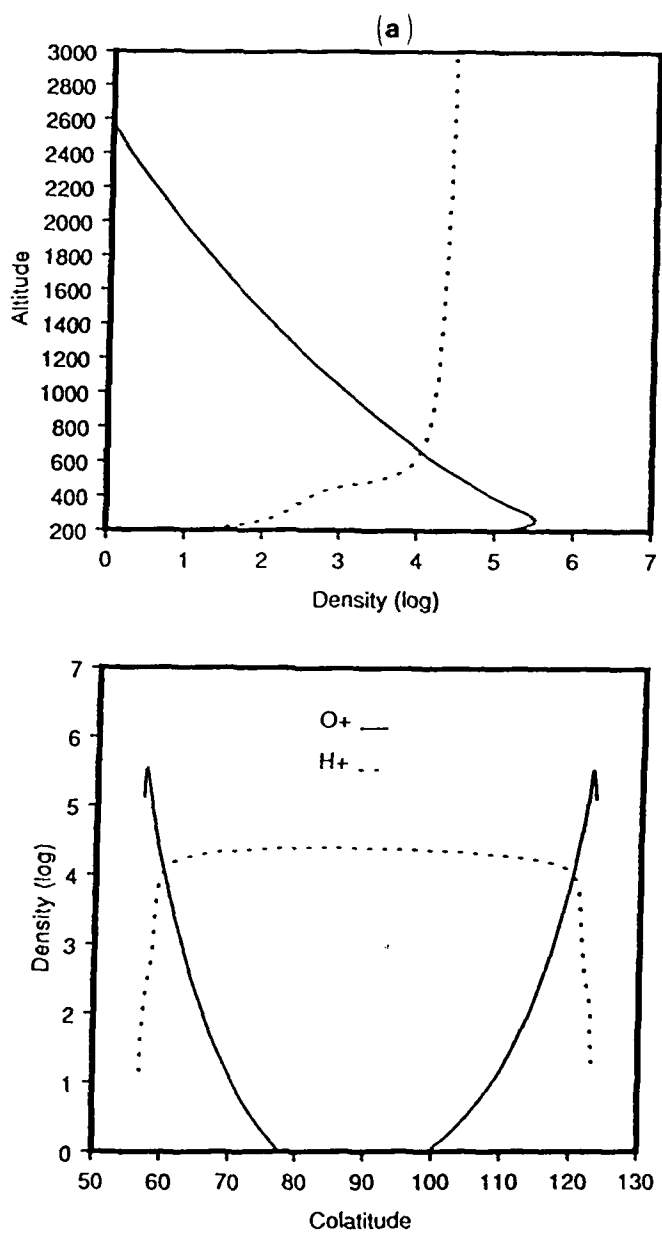


Figure 12. Plasma (a) densities and (b) temperatures along a magnetic field line with an equatorial crossing altitude of 3000 km for equinox and solar minimum conditions and 0° magnetic longitude. Electrodynamic, neutral wind, and adiabatic effects are neglected.

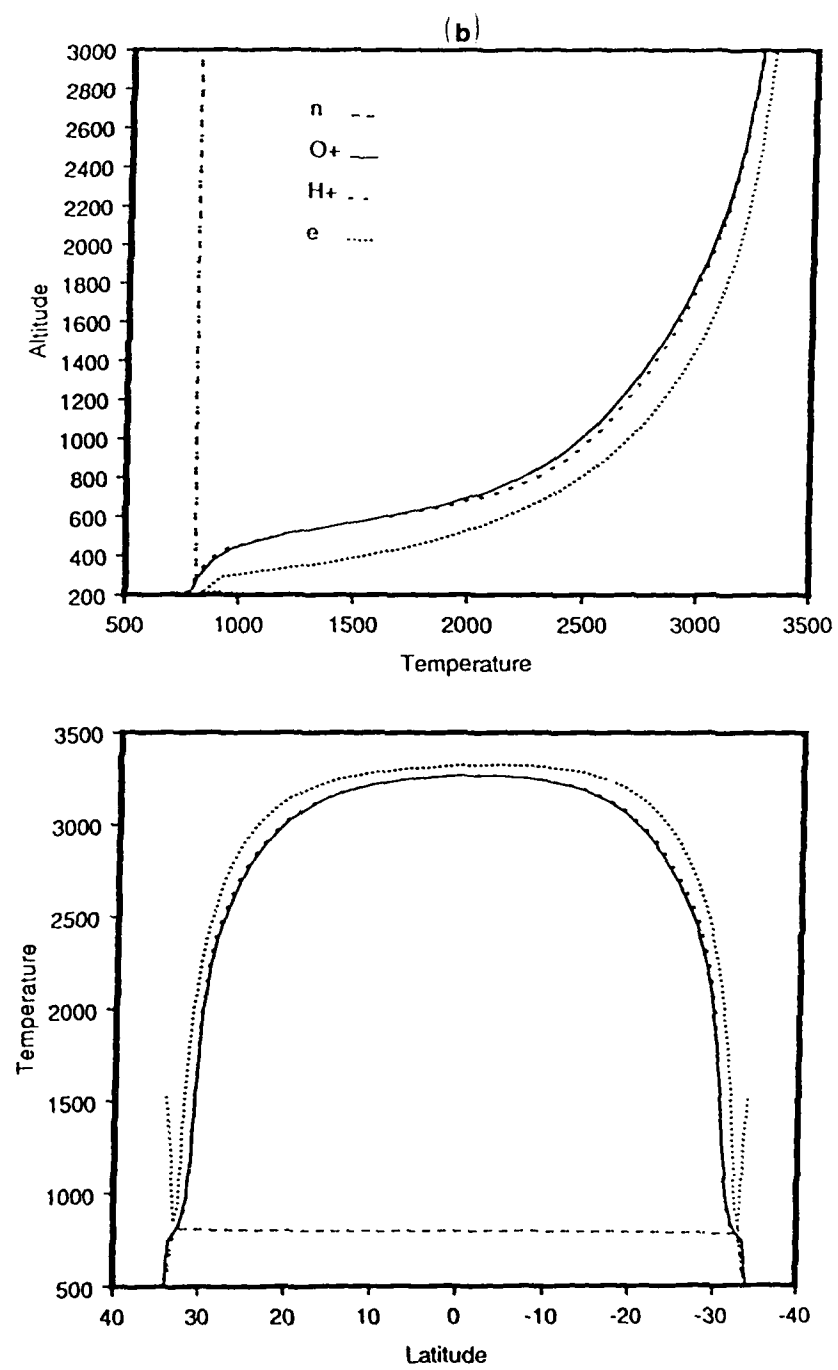


Figure 12. (cont.)

and equinox conditions. As with Figure 8, effects due to electrodynamic drift, neutral winds, and adiabatic effects due to field-aligned flow are neglected. For this field line, peak F_2 region densities are $5.2 \times 10^5 \text{ cm}^{-3}$ and the height of the F_2 peak is 265 km. At 3000 km, the O^+ density drops below 1 cm^{-3} and the H^+ density is $3 \times 10^4 \text{ cm}^{-3}$. The ion temperatures are nearly equal at 3000 km. The electron temperature is about 50° warmer than the ion temperature.

Figure 13 is also valid at solar minimum for a field line with an equatorial altitude of 3000 km, but is valid for northern hemisphere summer. Once again neutral wind effects and electrodynamic drifts are neglected. The peak densities in the F_2 region now exhibit a slight asymmetry between hemispheres. The peak density in the southern hemisphere becomes the larger peak and the northern hemisphere peak density has actually decreased in magnitude from the equinox case. Temperatures of all species have increased slightly in the northern hemisphere and decreased slightly in the southern hemisphere.

Figure 14 is valid for the same conditions as Figure 13 except that Figure 14 is valid for sunspot maximum. Most evident is the increase in F_2 peak densities from about $5 \times 10^5 \text{ cm}^{-3}$ to over $1 \times 10^6 \text{ cm}^{-3}$. O^+ densities have increased by two orders of magnitude at the top of the field line. H^+ densities increased slightly at the equator, but dropped sharply between 200 – 1200 km. Temperatures within the F_2 peak drop to the neutral temperature due to strong coupling between the ions and the neutrals and the marked increase in electron density. Temperatures of all species at the magnetic equator have increased from over 3000°K to over 4500°K .

Next, the effects of a field-aligned plasma flow (induced by a horizontal, meridional neutral wind) on the plasma densities along the field line will be considered. Figure 15 shows the effects of a summer to winter hemisphere neutral wind on plasma densities. As plasma is pushed up the field line in the northern hemisphere, it enters a region of lower recombination rates and so plasma densities are increased along the northern half of the field line. The downward flow of

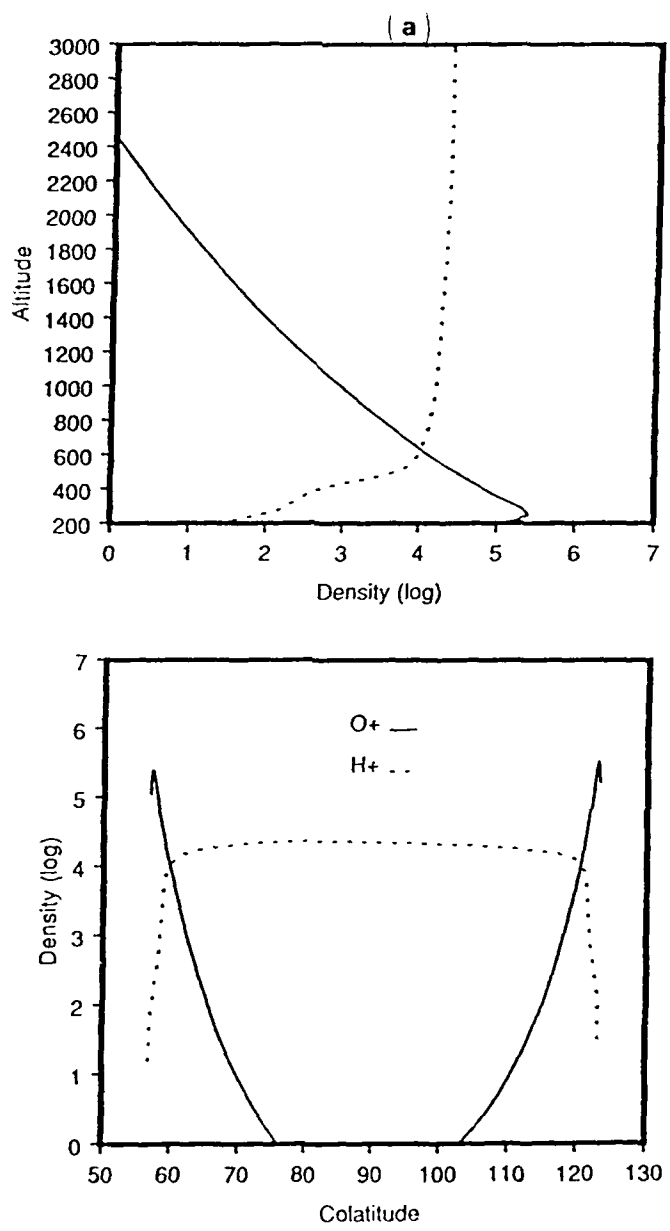


Figure 13. Plasma (a) densities and (b) temperatures along a magnetic field line with an equatorial crossing altitude of 3000 km for solstice and solar minimum conditions and 0° magnetic longitude. Electrodynamic, neutral wind, and adiabatic effects are neglected.

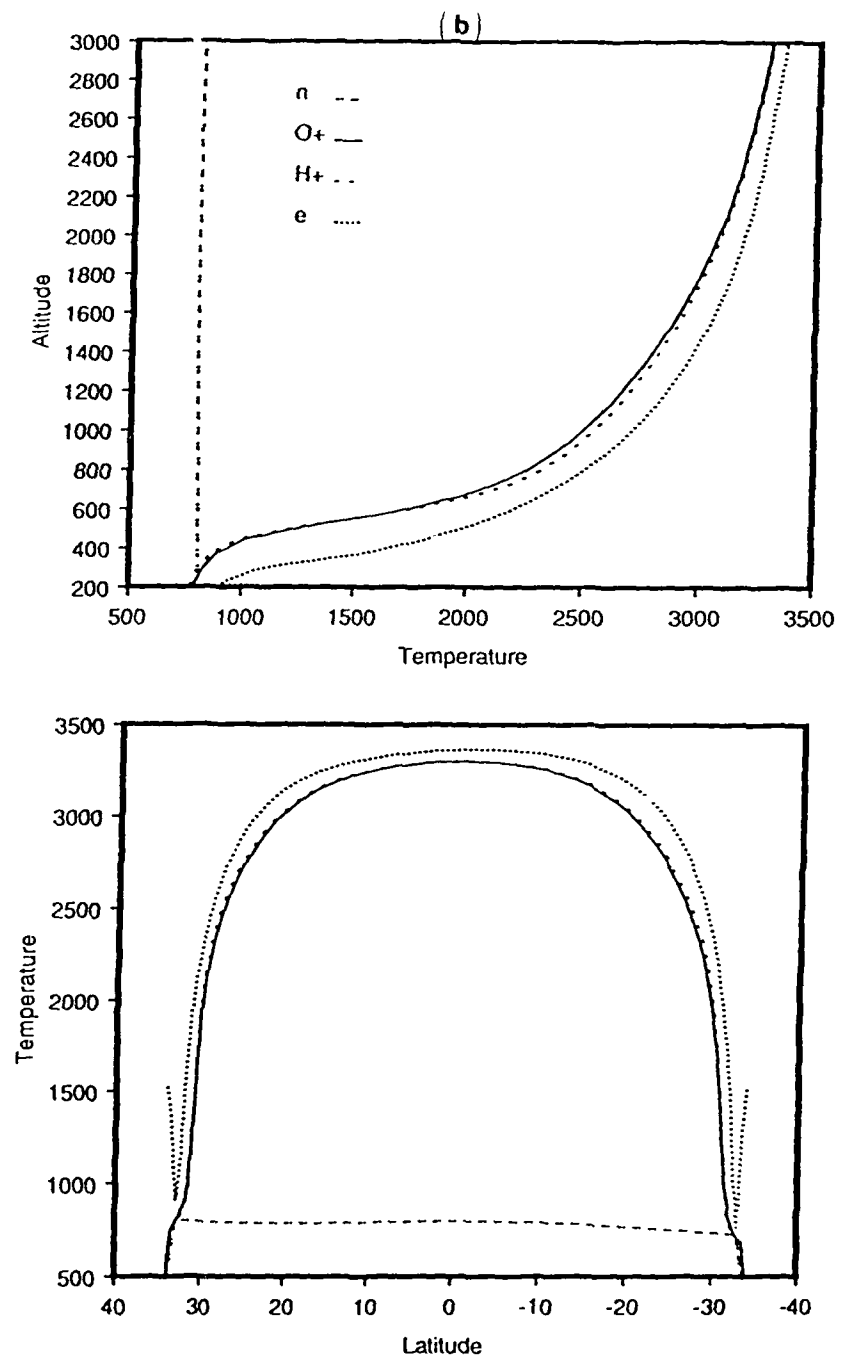


Figure 13. (cont.)

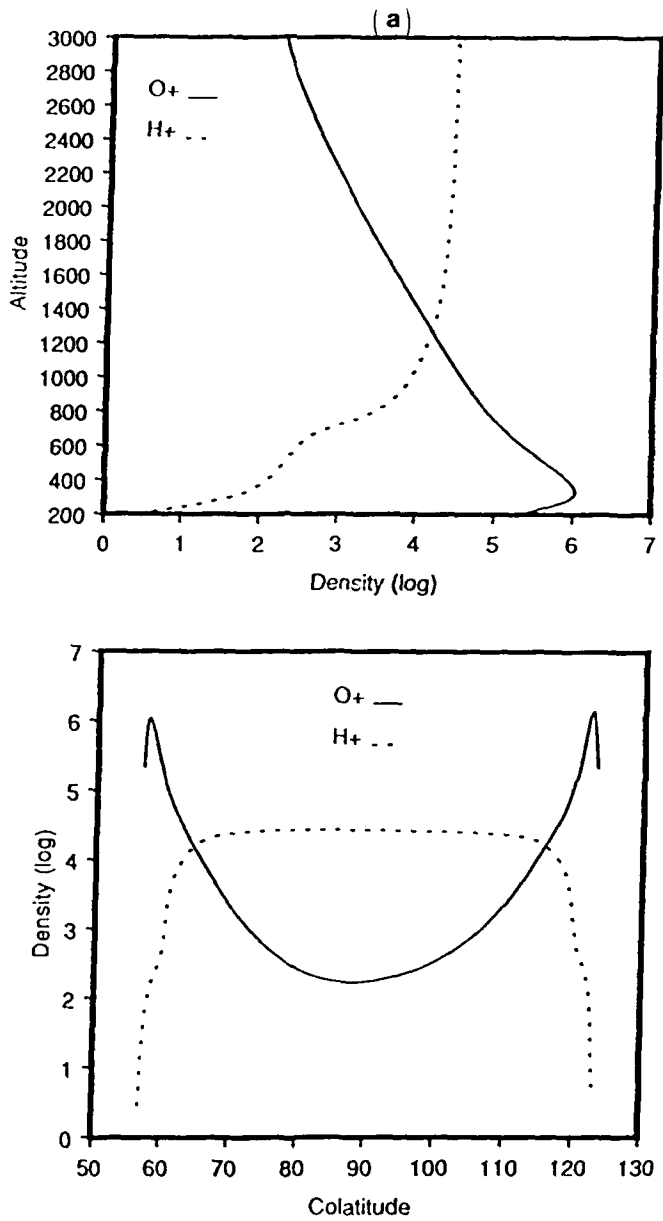


Figure 14. Plasma (a) densities and (b) temperatures along a magnetic field line with an equatorial crossing altitude of 3000 km for solstice and solar maximum conditions and 0° magnetic longitude. Electrodynamic, neutral wind, and adiabatic effects are neglected.

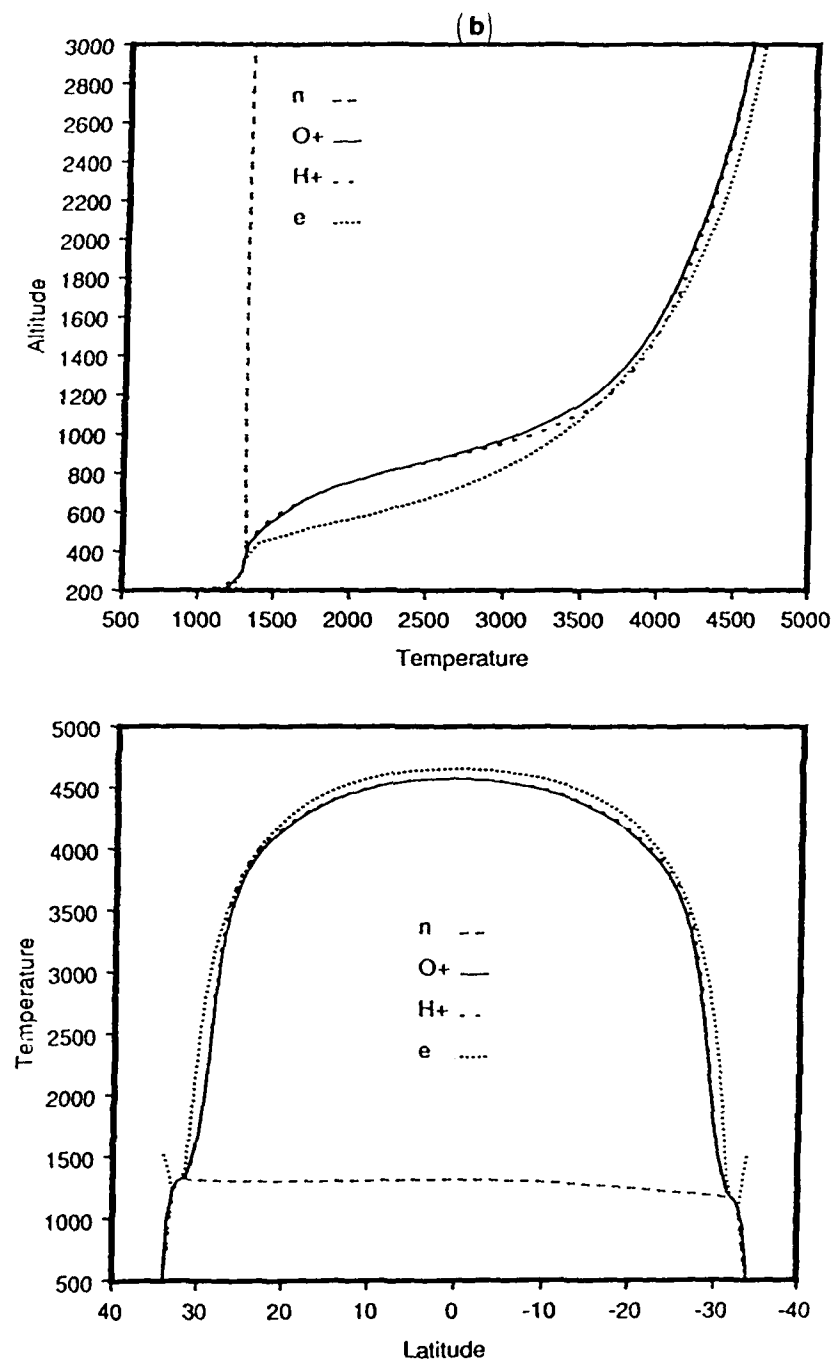


Figure 14. (cont.)

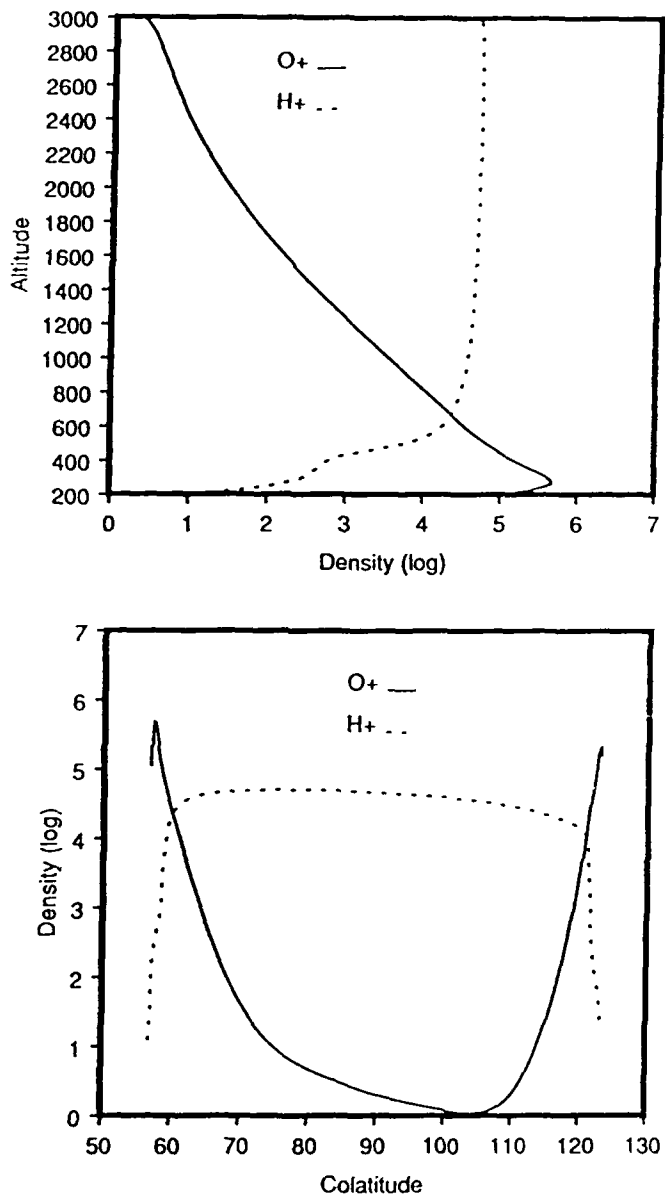


Figure 15. Plasma densities along a magnetic field line with an equatorial crossing altitude of 3000 km for solstice and solar minimum conditions and 0° magnetic longitude. Electrodynamic and adiabatic effects are neglected. Neutral wind effects on densities are included.

plasma in the southern hemisphere, likewise, pushes the plasma into regions of higher chemical recombination rates and plasma densities along the field line are reduced.

CHAPTER V

SUMMARY AND CONCLUSIONS

A number of unique transport effects occur in the low-latitude ionosphere in the height range 200 – 3000 km. These transport effects include the formation of the Appleton anomaly, which is due to upward electrodynamic drift of the plasma at the magnetic equator and downward diffusion of this plasma along magnetic field lines during the day. Because the field lines are inclined to the vertical, meridional neutral winds can cause a transport of ionospheric plasma parallel to \mathbf{B} and produce asymmetries in the F -region densities and temperatures between conjugate hemispheres. Longitudinal asymmetries in the F -region can arise due to the offset in the magnetic and geographic coordinate systems. Nighttime F -region densities are maintained at much higher densities than can be explained by recombination. This maintenance of the nighttime F -region can be explained by upward transport of plasma into regions of lower recombination rates.

Our model provides time-dependent, self-consistent solutions for the coupled continuity-momentum and energy equations for O^+ , H^+ , and electrons. It assumes an ionosphere composed of two primary ion species (H^+ and O^+) and electrons for the range of altitudes under consideration. Additionally, we assume the plasma behaves as a displaced Maxwellian and, therefore, the fluid equations apply.

The basis for our continuity-momentum equation is the work of *Sterling et al.* [1969]. *Sterling et al.* [1969] developed a set of diffusion coefficients appropriate for curved, dipole field lines for a coordinate system which $\mathbf{E} \times \mathbf{B}$ drifts with the field line. As a result, in this frame of reference, all motions are field-aligned and the problem becomes one-dimensional (parallel to \mathbf{B}). Unfortunately, their model suffers from overly simplistic assumptions concerning low-latitude electric

fields and meridional, neutral wind speeds. The energy equation follows the basic approach of *Bailey et al.* [1973].

The linearized, continuity-momentum equation presented couples calculations of H⁺ and O⁺ densities and diffusion velocities. To solve the continuity-momentum equation and the energy equations, we adopt an orthogonal, curvilinear coordinate system in which the dipole field lines are lines of constant p and the potentials are lines of constant q . Any point can now be uniquely defined in terms of p and q . If we calculate along a field line ($p = \text{constant}$), then all variations can be expressed in terms of q .

Dominant chemistry in the 200 – 3000 km height range is included. These reactions involve the photoionization of neutral O and the charge exchange reactions between O⁺ and H⁺. Although only important at the lowest heights being considered, the loss of O⁺ in reactions with N₂ and O₂ are also included. Calculations of the photoionization of O use the Chapman grazing incidence function [*Smith and Smith*, 1972].

Flow velocities are obtained from the momentum equation. To solve for these flow velocities, we assume steady state, that viscous and nonlinear terms can be neglected, and that all flow is parallel to B. The electric field in the momentum equation for each ion species is calculated from the electron momentum equation by assuming the flow of the electrons is determined by a balance between electrostatic and pressure gradient forces. The appropriate collision frequencies are obtained from *Schunk* [1983]. These flow velocities are then substituted into the continuity equation.

Next, the continuity equation is evaluated to yield ion densities along the field line. The velocity of each ion species is separated into its parallel and perpendicular components. The perpendicular component of drift is incorporated with the local time derivative to yield the convective derivative (fixing the coordinate system on the field line). Divergences and diffusion coefficients are then evaluated using *Sterling et al's* [1969] methods, except we chose to finite

difference some derivatives as opposed to expanding each term (as *Sterling et al.* [1969] did). Once these divergences are substituted back into the continuity equation, a nonlinear, second-order partial differential equation results. To solve this equation numerically, it must first be linearized. This is accomplished by performing a time-varying Taylor's expansion on all nonlinear terms.

The methods and assumptions used in deriving a linearized energy equation for each species are much the same as those for the continuity-momentum equation. Our derivation begins with the general form of the energy equation found in *Schunk* [1983]. Using the assumption that the plasma approximates a displaced Maxwellian, the 5-moment approach can be used to calculate the rate of energy exchange due to collisions. Next, the form of the continuity equation valid in a diffusive region is used in conjunction with the definition of the heat flow vector to obtain the time rate of change of the temperature of a given species. Within the energy equation, account is taken of the frictional heating/cooling of the ion species due to relative motion between the ion gas and the neutral gas, adiabatic expansion and compression, conduction along the field lines, and collisional heat exchange. In general, the O^+ ions gain heat through collisions with the electron and H^+ gases, and lose heat through inelastic interactions (charge exchange reactions) with H and elastic collisions with the neutrals. The H^+ ions gain heat from collisions with the electrons, and lose heat through collisions with O^+ , the neutrals, and O . The ambient electron gas loses heat through collisions with O^+ , H^+ , and the fine structure excitation of O .

Bailey et al. [1973] only consider the nighttime case. Since we were interested in modelling a variety of local times, a heating rate due to interaction of the photoelectrons with the ambient electron gas had to be adopted for daytime conditions. An empirical relation was developed from the results of *Swartz et al.* [1975]. Initially, the steady state electron temperatures obtained using this empirical model were much higher than previous calculations and observations. The heating factors were, therefore, scaled to obtain results more consistent

previously reported values.

Once the divergences are evaluated in the energy equations, a second-order, partial differential equation for each species results. Linearization is accomplished by converting the temperatures to an independent variable, γ . The equations are then linearized in terms of γ using time-varying Taylor's expansion.

A chief criticism of previous modelling efforts is that they employ very simplistic electric fields or neutral wind distributions. While these techniques may produce more accurate results in an isolated case, they are useless in general modelling applications where large errors would certainly occur. We attempt to improve upon previous efforts by incorporating average neutral wind speeds obtained from the Thermospheric Global Circulation Model (TGCM) [*Roble et al.*, 1977] for solar maximum and minimum conditions at equinox and solstice. Daily variations were introduced by interpolating wind speeds between equinox and solstice conditions based on the solar declination angle. When mapped into geomagnetic coordinates, longitudinal variations in the mean neutral wind speeds are introduced because of the tilt in the dipole field relative to the earth's rotational axis.

To estimate electric fields responsible for the electrodynamic drift of ionospheric plasma, we adopt the empirical model of *Richmond et al* [1980]. Developed for solar minimum conditions, the incorporation of this model allows for much more realistic estimates of the electric fields and the electrodynamic drifts than previously possible. With the help of *Richmond* [1988], a method was devised to calculate variations of this electrodynamic drift with height. Previous authors [*Anderson*, 1973a, 1973b; *Chan and Walker*, 1984a, 1984b] had assumed an electric field or electrodynamic drift velocity, and assumed it was independent of altitude. Our calculations for solar minimum, June solstice, 0° magnetic longitude, and local noon show that the variation of the drift velocity with height for the field line crossing the magnetic equator at 1000 km is approximately

one-half the vertical drift velocity. Since they are of the same order of magnitude, it is not clear that neglecting this variation of vertical drift velocity with altitude is a valid assumption. The east-west drift has generally been ignored based on the results of *Sterling et al.* [1969]; but since his electric fields were very simplistic, the importance of east-west electrodynamic drifts needs to be re-evaluated. Since we ran only cases for local noon, evaluation of the east-west electrodynamic drift will be undertaken in future tests of the model.

The prime focus of this research is the development of a low-latitude ionospheric model. Results were, therefore, aimed at demonstrating that the model could reproduce physical processes in the low-latitude ionosphere. Steady state profiles of density and temperature were created for the magnetic prime meridian for solar minimum, March equinox, and local noon. Electrodynamic, neutral wind, and adiabatic effects were not included in the model computations. This case served as a reference for the test cases to follow. When this case was repeated for solstice conditions, very little asymmetry was exhibited between hemispheres, but then there was little asymmetry in the neutral atmosphere. This test shows that the asymmetry between the *F*-region densities that has been observed during solstice conditions is not solely due to asymmetric solar input.

A second test involved the inclusion of electrodynamic drifts for equinox and solstice conditions. Density profiles showed the expected depletions of plasma at the magnetic equator and an increase in plasma density at $\pm 18^\circ$ near 300 km. Plasma temperatures decreased along the field line in response to the adiabatic expansion of the plasma as it was being forced upwards. Therefore, expected adiabatic effects were also reproduced correctly.

When strong north-to-south neutral winds were introduced, the model once again reproduced the correct trends. This effect is consistent with increased transport of plasma to greater heights where recombination rates are lower. For the southern hemisphere, the winds resulted in lower plasma densities because

more plasma was being forced into regions of higher recombination rates.

In summary, our model seems to reproduce the important physical processes in the low-latitude ionosphere in a manner consistent with theory and observations. We have achieved significant improvements over previous modelling efforts by including more realistic estimates of neutral winds and electric fields. In the process, we have increased the general applicability of our model to a wide variety of seasons, levels of solar activity, longitudes, and local times. An area of further improvement for this model would be to include a more physical treatment of the photoelectrons.

REFERENCES

- Abur-Robb, M.F.K. and D.W. Windle, On the day and night reversal in $N_m F_2$ north-south asymmetry, *Planet. Space Sci.*, 17, 97-106, 1969.
- Anderson, D.N., A theoretical study of the ionospheric *F* region equatorial anomaly — I. Theory, *Planet. Space Sci.*, 21, 409-419, 1973a.
- Anderson, D.N., A theoretical study of the ionospheric *F* region equatorial anomaly — II. Results in the American and Asian sectors, *Planet. Space Sci.*, 21, 421-442, 1973b.
- Anderson, D.N. and D.W. Rusch, Composition of the nighttime ionospheric *F*₁ region near the magnetic equator, *J. Geophys. Res.*, 85, 569-574, 1980.
- Anderson, David F., Michael Mendillo, and Bruce Herniter, A semi-empirical low-latitude ionospheric model, *Radio Sci.*, 22, 292-306, 1987.
- Bailey, G.J., The topside ionosphere above Arecibo at equinox during sunspot minimum, *Planet. Space Sci.*, 28, 47-59, 1980.
- Bailey, G.J., The effect of a meridional $E \times B$ drift on the thermal plasma at $L = 1.4$, *Planet. Space Sci.*, 31, 389-409, 1983.
- Bailey, G.J. and R.A. Heelis, Ion temperature troughs induced by a meridional neutral air wind in the night-time equatorial topside ionosphere, *Planet. Space Sci.*, 28, 895-906, 1980.
- Bailey, G.J. and R.J. Moffett, The topside equatorial ionosphere during daytime: elevated plasma temperatures, the transequatorial O^+ breeze and the dynamics of minor ions, *Planet. Space Sci.*, 27, 1075-1085, 1979.
- Bailey, G.J., R.J. Moffett, W.B. Hanson, and S. Sanatani, Effects of interhemispheric transport on plasma temperatures at low latitudes, *J. Geophys. Res.*, 78, 5597-5610, 1973.
- Bailey, G.J., R.J. Moffett, and W.E. Swartz, Effects of photoelectron heating and interhemispheric transport on day-time plasma temperatures at low latitudes, *Planet. Space Sci.*, 23, 599-610, 1975.
- Bailey, G.J., R.J. Moffett, and J.A. Murphy, Relative flow of H^+ and O^+ ions in the topside ionosphere at mid-latitudes, *Planet. Space Sci.*, 25, 967-972, 1977a.
- Bailey, G.J., R.J. Moffett, and J.A. Murphy, A theoretical study of night-time field-aligned O^+ and H^+ fluxes in a mid-latitude magnetic field tube at equinox under sunspot maximum conditions, *J. Atmos. Terr. Phys.*, 39, 105-110, 1977b.
- Banks, P.M. and G. Kockarts, *Aeronomy, Part B*, Academic Press, 1973.

- Banks, P.M., R.W. Schunk, and W.J. Raitt, The topside ionosphere: A region of dynamic transition, *Annl. Rev. Earth & Planet. Sci.*, **4**, 381-440, 1976.
- Baxter, Roger G., On the theoretical effects of electrodynamic drift in the equatorial F_2 -layer, *J. Atmos. Terr. Phys.*, **26**, 711-120, 1964.
- Baxter, Roger G., A numerical solution of the time-varying diffusion equation for the F_2 -layer, *Planet. Space Sci.*, **15**, 701-713, 1967.
- Baxter, R.G. and P.C. Kendall, A theoretical technique for evaluating the time-dependent effects of general electrodynamic drifts in the F_2 layer of the ionosphere, *Proc. Roy. Soc. London, A904*, 171-185, 1968.
- Bittencourt, J.A. and Y. Sahai, F -region neutral winds from ionosonde measurements of HmF_2 at low latitude conjugate regions, *J. Atmos. Terr. Phys.*, **40**, 669-676, 1978.
- Bramley, E.N. and M. Peart, Diffusion and electromagnetic drift in the equatorial F_2 -region, *J. Atmos. Terr. Phys.*, **27**, 1201-1211, 1965.
- Bramley, E.N. and Margaret Young, Winds and electromagnetic drifts in the equatorial F_2 -region, *J. Atmos. Terr. Phys.*, **30**, 99-111, 1968.
- Chan, H.F. and G.O. Walker, Computer simulations of the ionospheric equatorial anomaly in East Asia for equinoctial, solar minimum conditions. Part I — Formulation of the model, *J. Atmos. Terr. Phys.*, **46**, 1103-1112, 1984a.
- Chan, H.F. and G.O. Walker, Computer simulations of the ionospheric equatorial anomaly in East Asia for equinoctial, solar minimum conditions. Part II — Results and discussion of wind effects, *J. Atmos. Terr. Phys.*, **46**, 1103-1112, 1984b.
- Chen, Francis F., *Introduction to Plasma Physics and Controlled Fusion, Volume 1: Plasma Physics*, Plenum Press, 1984.
- Chi, Y.T., An improved phenomenological model of ionospheric density, *J. Atmos. Terr. Phys.*, **37**, 1563-1570, 1975.
- Evans, J.V. and J.M. Holt, Nighttime proton fluxes at Millstone Hill, *Planet. Space Sci.*, **26**, 727-744, 1978.
- Hanson, W.B. and T.N.L. Patterson, The maintenance of the night-time F -layer, *Planet. Space Sci.*, **12**, 979-997, 1964.
- Hargreaves, J.K., *The Upper Atmosphere and Solar-Terrestrial Relations: An Introduction to the Aerospace Environment*, Van Nostrand Reinhold Co., 1979.
- Hedin, Alan E., MSIS-86 thermospheric model, *J. Geophys. Res.*, **92**, 4649-4662, 1987.
- Kendall, P.C., Geomagnetic control of diffusion in the F_2 -region of the ionosphere — I, *J. Atmos. Terr. Phys.*, **24**, 805-811, 1962.

- Kendall, P.C. and W.M. Pickering, Magnetoplasma diffusion at F_2 -region altitudes, *Planet. Space Sci.*, 15, 825-833, 1967.
- Kroehl, H.W., private communication, 1987.
- Moffett, R.J. and W.B. Hanson, Calculated distributions of hydrogen and helium ions in the low-latitude ionosphere, *J. Atmos. Terr. Phys.*, 35, 207-222, 1973.
- Moffett, R.J., G.J. Bailey, and P.A. Simmons, Field-aligned plasmaspheric flows at moderate latitudes, *Adv. Space Res.*, 6, 153-156, 1986.
- Murphy, J.A., G.J. Bailey, and R.J. Moffett, calculated daily variations of O^+ and H^+ at mid-latitudes — I. Protonospheric replenishment and F -region behaviour at sunspot minimum, *J. Atmos. Terr. Phys.*, 38, 351-164, 1976.
- Raitt, W.J., private communication, 1988.
- Raitt, W.J., R.W. Schunk, and P.M. Banks, A comparison of the temperature and density structure in high and low speed thermal proton flows, *Planet. Space Sci.*, 23, 1103, 1975.
- Richards, P.G., R.W. Schunk, and J.J. Sojka, Large-scale counterstreaming of H^+ and He^+ along plasmaspheric flux tubes, *J. Geophys. Res.*, 88, 7879-7886, 1983.
- Richmond, A.D., private communication, 1988.
- Richmond, A.D., M. Blanc, B.A. Emery, R.H. Wand, B.G. Fejer, R.F. Woodman, S. Ganguly, P. Amayenc, R.A. Behnke, C. Calderon, and J.V. Evans, An empirical model of quiet-day ionospheric electric fields at middle and low latitudes, *J. Geophys. Res.*, 85, 4658-4664, 1980.
- Rishbeth, H., A time-varying model of the ionospheric F_2 -layer, *J. Atmos. Terr. Phys.*, 26, 657-685, 1964.
- Rishbeth, H., F_2 -layer rates at sunspot minimum, *J. Atmos. Terr. Phys.*, 28, 911-918, 1966.
- Rishbeth, H. and O.K. Garriott, *Introduction to Ionospheric Physics*, Academic Press, 1969.
- Rishbeth, H., A.J. Lyon, and Margaret Peart, Diffusion in the equatorial F layer, *J. Geophys. Res.*, 68, 2559-2569, 1963.
- Roble, R.G., R.E. Dickinson, and E.C. Ridley, Seasonal and solar cycle variations of the zonal mean circulation in the thermosphere, *J. Geophys. Res.*, 82, 5493-5504, 1977.
- Schunk, R.W., Transport equations for aeronomy, *Planet. Space Sci.*, 23, 437-485, 1975.
- Schunk, R.W., "The Terrestrial Ionosphere", *Solar-Terrestrial Physics*, edited by R.L. Carovillano and J.M. Forbes, D. Reidel Publishing Company, 1983.

- Schunk, R.W., private communication, 1988.
- Schunk, R.W. and Andrew F. Nagy, Electron Temperatures in the F region of the ionosphere: Theory and observations, *Rev. Geophys. Space Phys.*, **16**, 355–399, 1978.
- Schunk, R.W. and J.C.G. Walker, Theoretical ion densities in the lower ionosphere, *Planet. Space Sci.*, **21**, 1875–1896, 1973.
- Sheikh, N., K. Rebstock, and D. Bilitza, *Computer programs related with numerical mapping after CCIR-Report 340, IPW-WB9*, Institut f. Physikalische Weltraumforschung, Freiburg, F.R.G., 1978.
- Smith III, F.L. and Cody Smith, Numerical evaluation of Chapman's grazing incidence integral $\text{ch}(\chi, \chi_p)$, *J. Geophys. Res.*, **77**, 3592–3597, 1972.
- Sterling, D.L., W.B. Hanson, R.J. Moffett, and R.G. Baxter, Influence of electromagnetic drifts and neutral air winds on some features of the F_2 region, *Radio Sci.*, **4**, 1005–1023, 1969.
- Swartz, W.E., G.J. Bailey, and R.J. Moffett, Electron heating resulting from interhemispherical transport of photoelectrons, *Planet. Space Sci.*, **23**, 589–598, 1975.
- Thomas, Lance, Electron density distributions in the daytime F_2 layer and their dependence on neutral gas, ion, and electron temperatures, *J. Geophys. Res.*, **71**, 1357–1366, 1966.
- Thomas, G.R. and F.H. Venables, The effect of diurnal temperature changes on the F_2 -layer, *J. Atmos. Terr. Phys.*, **29**, 621–640, 1967.
- Young, E.R., D.G. Torr, and P.G. Richards, Counterstreaming of O^+ and H^+ ions in the plasmasphere, *Geophys. Res. Lett.*, **6**, 925–928, 1979.
- Young, E.R., D.G. Torr, P.G. Richards, and A.F. Nagy, A computer simulation of the midlatitude plasmasphere and ionosphere, *Planet. Space Sci.*, **28**, 881–893, 1980.

APPENDICES

Appendix A: Neutral Wind Model

The neutral wind model used in this study allows for variations of the north-south component of the neutral wind speed with magnetic latitude, magnetic longitude, altitude, day of the year, and local time. To accomplish this, the analytic expressions for the diurnal, V24 (A1), semi-diurnal, V12 (A2), terdiurnal, V8 (A3) variations, and the total wind speed, U (A5), were taken from *Anderson et al.*, [1987] except that θ_{24} (A4) has been redefined.

$$V24 = 2\theta_{24} \cos \left[\frac{2\pi}{24} \left(t - 18 - \frac{|\theta_{24}|}{7} \right) \right] \quad (A1)$$

$$V12 = 50 \sin \left(\frac{\pi}{180} \frac{10\alpha}{3} \right) \cos \left[\frac{2\pi}{12} \left(t - 9 - \frac{|\alpha|}{12} \right) \right] \quad (A2)$$

$$V8 = 0.38\alpha \cos \left[\frac{2\pi}{8} (t - 8.2 + 0.079 |\alpha|) \right] \quad (A3)$$

$$\theta_{24} = \alpha + 10\eta \frac{|\delta|}{23.5} \quad (A4)$$

$$U = V0 + V8 + V12 + V24 \quad (A5)$$

$$\delta = \arcsin [23.5 \sin(R)] \quad (A6)$$

$$R = 360 \left(\frac{DD - 80}{365} \right) \quad (A7)$$

$$\eta = \left(\frac{-\delta}{|\delta|} \right) \quad (A8)$$

where α is the geographic latitude, t is the local time, δ is the solar declination angle, DD is the Julian date, R is the number of days after March equinox converted to degrees, and U is the resulting meridional wind speed in meters per second defined positive from north to south.

The mean wind speed, V_0 , was obtained from the results of *Roble et al.* [1977] in which they give mean values for the zonal and meridional components of the neutral wind for equinox and solstice conditions for solar minimum and solar maximum in geographic coordinates. Estimates of these values for every 10° latitude from $40^\circ S$ to $40^\circ N$ and every 50 km from 200 km to 600 km are shown in Tables 1 - 6. Since the results of *Roble et al.* [1977] did not extend to 600 km in all cases, winds are assumed to be constant above the maximum height presented in their paper. This maximum height varies from 400 km for solstice, solar minimum conditions to 600 km for equinox, solar maximum conditions. For points outside this range of altitudes or geographic latitudes, the winds are assumed constant and equal to the value for the mean wind at the nearest point inside the array. Since our model requires the component of the neutral wind speed along the magnetic field line, the components of the neutral wind speed in geographic coordinates are converted to magnetic coordinates using equations (A9) and (A10) given below.

$$U_{eq} = U_{zonal,e} \sin(\Delta) + U_{mer,e} \cos(\Delta) \quad (A9)$$

$$U_{sol} = U_{zonal,s} \sin(\Delta) + U_{mer,s} \cos(\Delta) \quad (A10)$$

where Δ is the magnetic declination angle, $U_{zonal,e}$ is the zonal component of the neutral wind speed at equinox, $U_{mer,e}$ is the meridional component of neutral wind speed at equinox, $U_{zonal,s}$ is the zonal component of the neutral wind speed at solstice, and $U_{mer,s}$ is the meridional component of the neutral wind speed at solstice. Now, the mean, meridional component of the neutral wind speed, V_0 (A11), can be determined by interpolating between the solstice and equinox values based on the solar declination angle.

$$V_0 = U_{eq} - \left((U_{eq} - U_{sol}) \frac{|\delta|}{23.5} \right) \quad (A11)$$

TABLE 1. Zonal Neutral Wind Speeds for Equinox
and Solar Maximum Conditions. Speeds are in
Meters/Second and Eastward Winds are
Defined as Positive.

Altitude (km)	Latitude									
	-40	-30	-20	-10	0	10	20	30	40	
200	20	40	40	25	18	25	40	40	20	
250	15	23	20	18	16	18	20	23	15	
300	8	17	18	15	14	15	18	17	8	
350	3	10	13	12	13	12	13	10	3	
400	0	7	8	9	11	9	8	7	0	
450	-5	3	3	6	8	6	3	3	-5	
500	-8	0	0	3	5	3	0	0	-8	
550	-8	-5	-2	2	3	2	-2	-5	-8	
600	-8	-5	-2	2	3	2	-2	-5	-8	

TABLE 2. Meridional Neutral Wind Speeds for Equinox
and Solar Maximum Conditions. Speeds are in
Meters/Second and Southward Winds are
Defined as Positive.

Altitude (km)	Latitude									
	-40	-30	-20	-10	0	10	20	30	40	
200	12	8	3	0	0	0	-3	-8	-12	
250	15	8	5	2	0	-2	-5	-8	-15	
300	11	7	5	2	0	-2	-5	-7	-11	
350	10	6	4	2	0	-2	-4	-6	-10	
400	10	1	1	2	0	-2	-1	-1	-10	
450	10	0	-1	1	0	-1	1	0	-10	
500	10	-1	-3	-1	0	1	3	1	-10	
550	10	-1	-3	-2	0	2	3	1	-10	
600	10	-1	-3	-2	0	2	3	1	-10	

TABLE 3. Zonal Neutral Wind Speeds for Winter Solstice and Solar Maximum Conditions.
Speeds are in Meters/Second and Eastward Winds are Defined as Positive

Altitude (km)	Latitude								
	-40	-30	-20	-10	0	10	20	30	40
200	-10	15	20	12	15	25	40	40	35
250	-25	0	5	0	5	20	23	28	35
300	-35	-15	-10	-5	5	20	23	28	40
350	-40	-20	-12	-5	5	20	23	28	40
400	-45	-25	-15	-5	5	20	23	28	40
450	-45	-30	-15	-5	5	20	23	28	40
500	-45	-30	-15	-5	5	20	23	28	40
550	-45	-30	-15	-5	5	20	23	28	40
600	-45	-30	-15	-5	5	20	23	28	40

TABLE 4. Meridional Neutral Wind Speeds for Winter Solstice and Solar Maximum Conditions. Speeds are in Meters/Second and Southward Winds are Defined as Positive.

Altitude (km)	Latitude								
	-40	-30	-20	-10	0	10	20	30	40
200	55	45	45	45	50	45	40	30	20
250	70	55	55	65	70	60	53	40	30
300	85	70	70	80	80	73	63	50	40
350	100	80	80	88	88	78	68	60	40
400	110	88	88	91	90	80	70	61	48
450	115	94	92	93	91	81	71	62	50
500	120	97	95	93	91	82	73	65	50
550	120	97	95	93	91	82	73	65	50
600	120	97	95	93	91	82	73	65	50

TABLE 5. Zonal Neutral Wind Speeds for Winter Solstice and Solar Minimum Conditions.
 Speeds are in Meters/Second and Eastward Winds are Defined as Positive.

Altitude (km)	Latitude								
	-40	-30	-20	-10	0	10	20	30	40
200	-18	-15	-10	-5	5	15	35	55	70
250	-25	-18	-12	-6	0	18	40	65	80
300	-30	-20	-14	-8	0	20	40	65	80
350	-33	-25	-15	-10	0	20	40	65	80
400	-33	-25	-15	-10	0	20	40	65	80
450	-33	-25	-15	-10	0	20	40	65	80
500	-33	-25	-15	-10	0	20	40	65	80
550	-33	-25	-15	-10	0	20	40	65	80
600	-33	-25	-15	-10	0	20	40	65	80

TABLE 6. Meridional Neutral Wind Speeds for Winter Solstice and Solar Maximum Conditions. Speeds are in Meters/Second and Southward Winds are Defined as Positive.

Altitude (km)	Latitude								
	-40	-30	-20	-10	0	10	20	30	40
200	35	30	32	37	40	40	35	33	29
250	50	45	45	52	55	53	48	44	40
300	65	55	55	60	61	58	53	49	45
350	70	60	60	62	62	60	57	53	49
400	70	68	66	64	62	60	57	54	51
450	70	68	66	64	62	60	57	54	52
500	70	68	66	64	62	60	57	54	52
550	70	68	66	64	62	60	57	54	52
600	70	68	66	64	62	60	57	54	52

Finally, the total meridional component of the neutral wind speed is the sum of the mean wind speed (A11), the diurnal variation (A1), the semi-diurnal variation (A2), and the terdiurnal variation (A3) as given by equation (A5).

The results for a variety of input conditions are shown in Figures 16 - 22. Figure 16 shows the variation of the north-south component of the neutral wind for solar maximum, equinox conditions along 97° geomagnetic longitude at midnight. Since magnetic latitudes and geographic latitudes approximately coincide at this magnetic longitude, the winds along this magnetic meridian are fairly symmetric about the equator as might be expected for equinox. Winds in both magnetic hemispheres are directed toward the magnetic equator with maximum winds exceeding 90 meters/second at $\pm 30^{\circ}$ magnetic latitude, and are nearly constant with height.

Figure 17 shows winds for local noon, but is otherwise valid for the same conditions as Figure 16. As in Figure 16, the wind pattern is fairly symmetric about the equator. However, unlike Figure 16, there is now considerable variation of wind speed with height up to 500 km (Winds are assumed constant above 600 km.), and maximum wind speeds in the northern hemisphere are approximately double those in the southern hemisphere.

Figure 18 is an example of how neutral winds can vary with geomagnetic longitude due to the offset in the geographic and geomagnetic poles. Conditions in this case are the same as in Figure 16 except the magnetic longitude is now $179.8^{\circ} E$. This corresponds to the magnetic longitude where the magnetic latitudes and geographic latitudes are offset by about 11.4° . This offset results in a shifting of the entire wind pattern 11.4° towards the south and, hence, the symmetry between hemispheres is lost. For this case, winds do not reverse until $11.4^{\circ} S$ and maximum wind speeds in the northern hemisphere reach 100 meters/second; whereas, maximum wind speeds in the southern hemisphere only reach 50 meters/second. Therefore, the variation in wind speed with magnetic longitude for a fixed local time is solely determined by the offset in the two coordinate systems.

When compared with Figure 16, Figure 19 gives an example of seasonal variations of neutral wind speeds along a magnetic field line. Figure 19 is valid for essentially the same conditions as Figure 16 except the season is now June solstice. For this case, winds are generally directed from the summer hemisphere to the winter hemisphere, but they do reverse near $15^{\circ} S$. Wind speeds

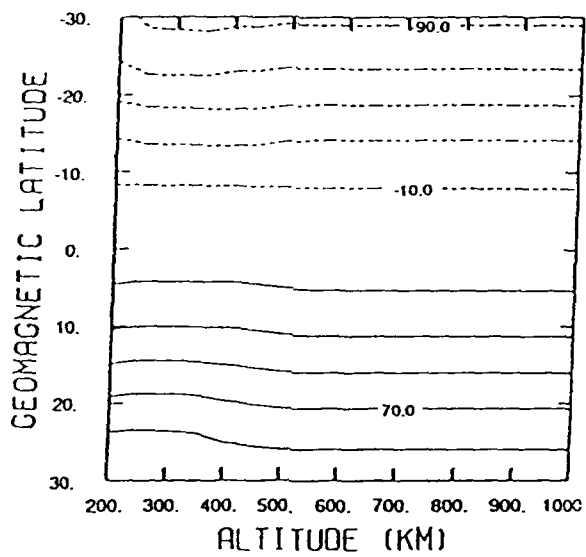


Figure 16. Meridional component of the neutral winds in meters/second along a magnetic field line. Winds are positive from north to south and the contour interval is 20 meters/second. The winds are valid for $97^{\circ}E$ magnetic longitude, equinox, solar maximum, and midnight local time.

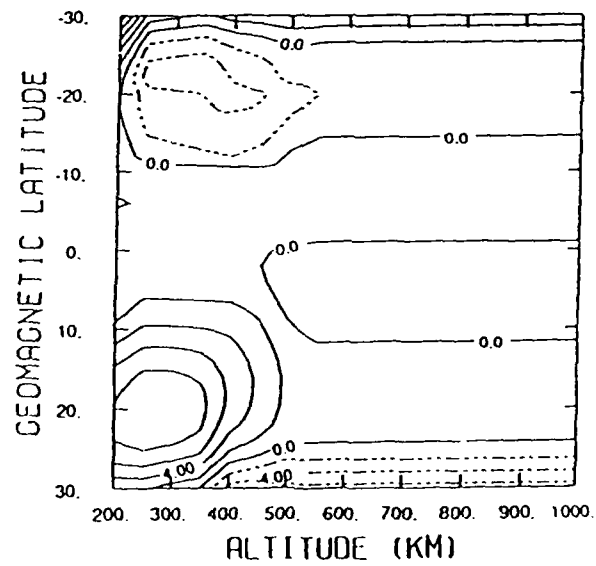


Figure 17. Meridional component of the neutral winds in meters/second along a magnetic field line. Same as Figure 16 except the local time is 1200. Winds are positive from north to south.

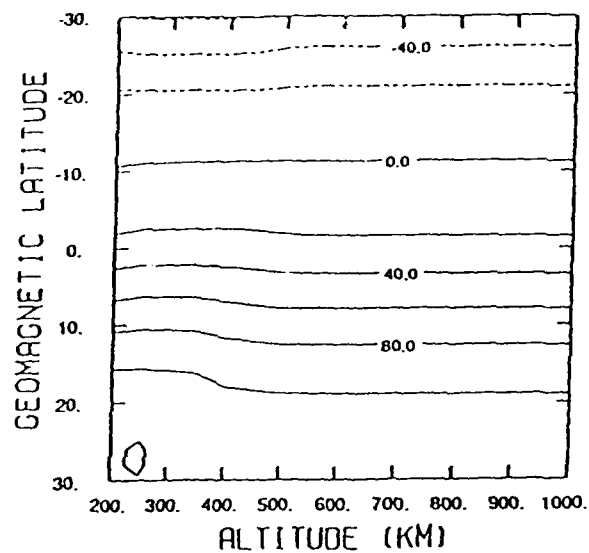


Figure 18. Meridional component of the neutral winds in meters/second along a magnetic field line. Winds are positive from north to south and the contour interval is 20 meters/second. The winds are valid for $179.8^{\circ} E$ magnetic longitude, equinox, solar maximum, and midnight local time.

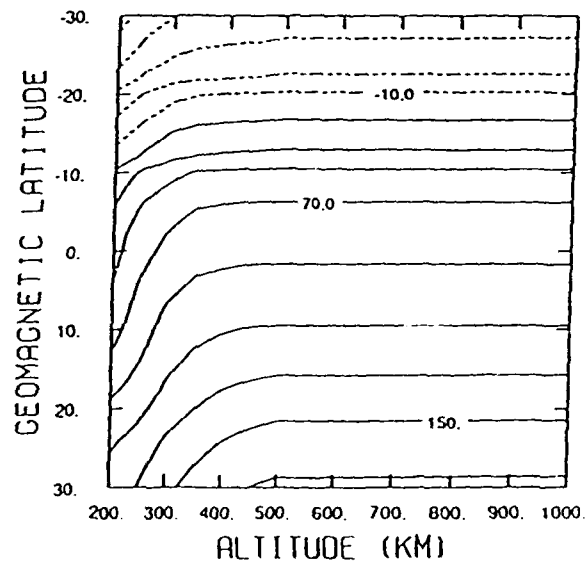


Figure 19. Meridional component of the neutral winds in meters/second along a magnetic field line. Winds are positive from north to south. The winds are valid for $97^{\circ} E$ magnetic longitude, solar maximum, June solstice, and midnight local time. Contour intervals are 20 meters/second.

have increased considerably from the Equinox case in the northern hemisphere with a maximum in excess of 170 meters/second, and decreased to about 60 meters/second in the southern hemisphere. For the midnight case at solstice, the winds increase with altitude up to 500 km above which they are assumed to be constant, and show considerable asymmetry as would be expected.

Figure 20 gives some typical neutral winds at 1200 LT for the same conditions as Figure 19. Winds in this case are directed from the summer to the winter hemisphere with the maximum in the wind speeds above 300 km occurring at the latitude corresponding to the subsolar point. Therefore, wind speeds generally decrease away from the latitude of the subsolar point at these altitudes. Below 300 km, the winds are nearly constant with latitude. The increase in wind speed with altitude at a given latitude is maintained from the midnight case (Winds are assumed constant above 500 km). Wind speeds for the local noon case at solstice are much stronger than for the equinox case shown in Figure 16, and the region of maximum winds has shifted from the lower levels for equinox to the upper levels for solstice.

Figure 21 shows estimated wind speeds for June solstice, solar maximum, $179.8^\circ E$, and midnight local time. This figure shows the effects of the offset of the magnetic and geographic axes for the solstice case. Once again, the entire wind pattern has shifted in accordance with the offset between the two coordinate systems for the chosen magnetic longitude. Maximum wind speeds for the northern hemisphere have increased to over 200 meters/second and the winds are now almost exclusively from the summer to winter hemisphere. The increase in wind speeds with altitude have become more pronounced for the summer hemisphere.

Figure 22 gives estimated winds for solar minimum, June solstice, $358.6^\circ E$ magnetic longitude, and midnight local time. At $358.6^\circ E$, the overall wind pattern is shifted about 11.4° northward due to the offset in the coordinate systems, and is, therefore, opposite to the case presented in Figure 21 with the added effect of decreased solar activity. One of the most noticeable results is the nearly symmetric pattern the winds now exhibit which would normally be associated with equinox type conditions if the magnetic and geographic poles were assumed to coincide. When the effects due to shifting the wind pattern are removed (by comparing with Figure 19), the effect due to decreasing solar activity on the wind speeds is to decrease them about ~ -30 meters/second.

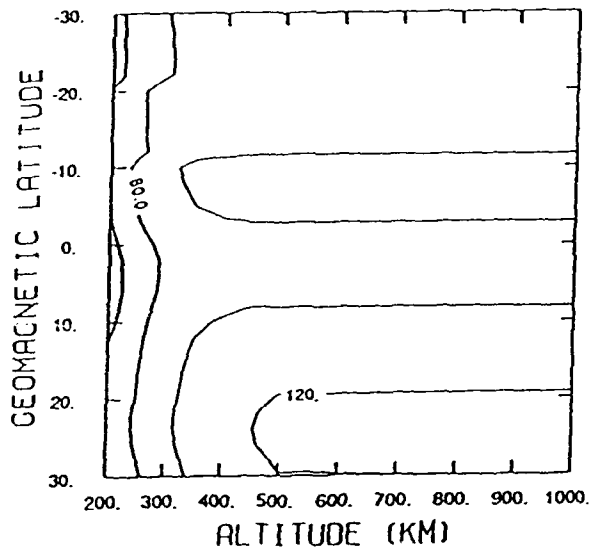


Figure 20. Meridional component of the neutral winds in meters/second along a magnetic field line. Winds are positive from north to south and the contour interval is 20 meters/second. The winds are valid for 97°E magnetic longitude, June solstice, solar maximum, and 1200 LT.

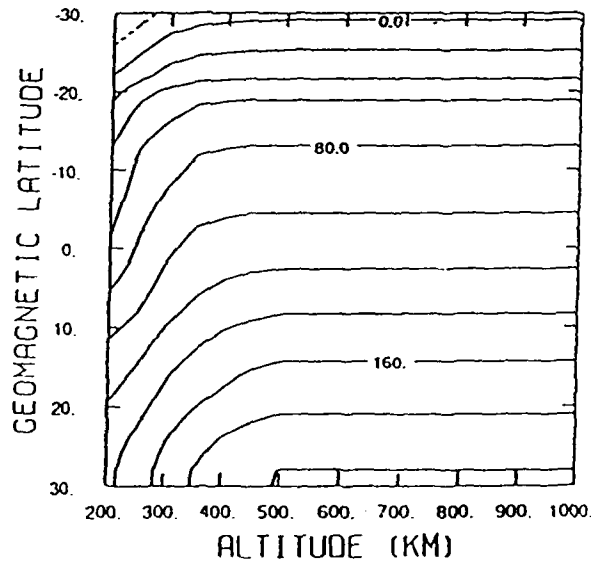


Figure 21. Meridional component of the neutral winds in meters/second along a magnetic field line. Winds are positive from north to south. The winds are valid for 179.8°E magnetic longitude, solar maximum, June solstice, and midnight local time. Contour intervals are 20 meters/second.

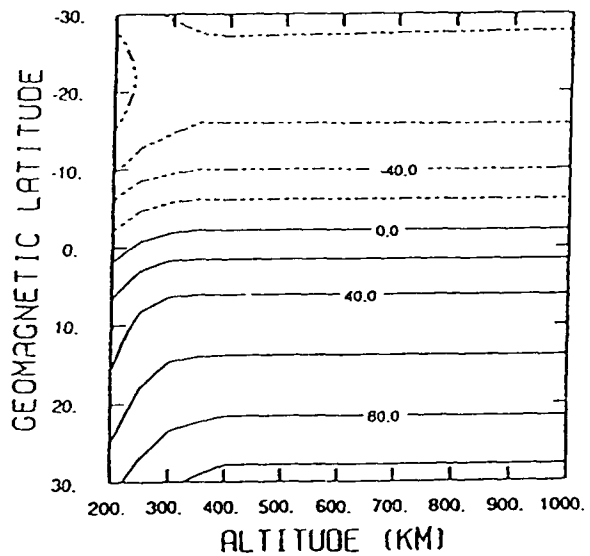


Figure 22. Meridional component of the neutral winds in meters/second along a magnetic field line. Winds are positive from north to south. The winds are valid for $358.6^{\circ}E$ magnetic longitude, solar maximum, June solstice, and midnight local time. Contour intervals are 20 meters/second.

Since the induced, parallel (to B) drift of the ions due to the neutral winds can have significant effects on ionospheric densities by moving ions into regions of faster or slower recombination or on ion temperatures due to adiabatic heating or cooling, accurately modelling seasonal, local time, solar cycle, and longitudinal variations of the neutral winds becomes critical. Although this model only gives crude estimates of these variations, it will extend previous modelling efforts [Bailey *et al.* 1973, Bailey and Heelis, 1980] over a wider range of conditions.

*Appendix B: An Empirical Model of
the Magnetic Field*

The magnetic field model, FIELDG, incorporated into this study was taken from the IRI-86 empirical model of the ionosphere. According to the documentation accompanying the subroutine in IRI, FIELDG is a special version of the POGO 68/10 magnetic field, Legendre model. FIELDG uses transformation coefficients valid for 1973 (*Sheikh et al., 1978*).

Figure 23 shows the magnetic field strength at 200 km using FIELDG.

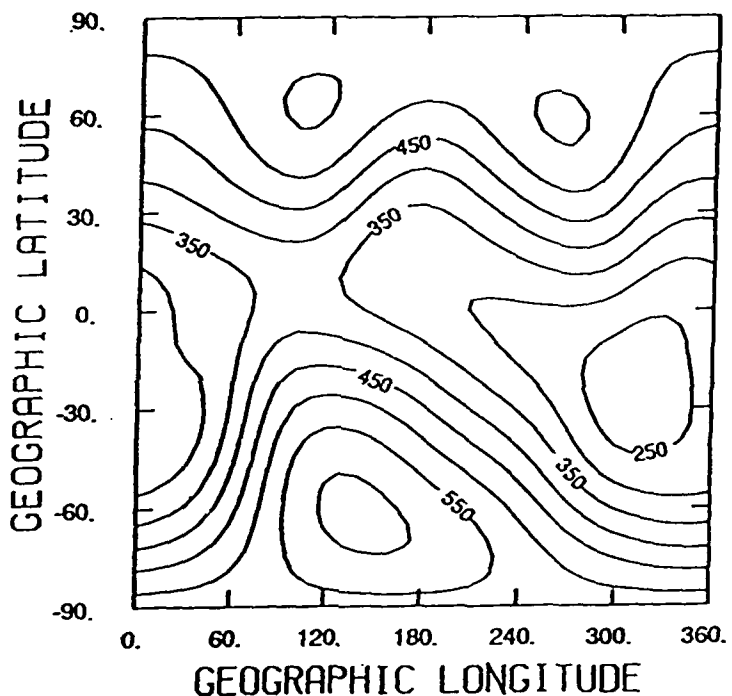


Figure 23. Global magnetic field strengths from FIELDG for 200 km. The contour labels are 10^{-7} Teslas and the contour interval is 5×10^{-6} Teslas.

FIELDG reproduces the South Atlantic anomaly and the relative maximum in field strength near $70^\circ N$, $110^\circ E$. Estimating from Figure 23, the magnetic poles appear to be located near $60^\circ N$, $270^\circ E$ and $60^\circ S$, $140^\circ E$.

*Appendix C: An Empirical Model of
Electric Fields at Low Latitudes*

Determination of the electrodynamic drift velocities along magnetic field lines requires the electric field be specified. Therefore, the empirical electric field model of *Richmond et al.* [1980] was adopted. This model gives values for electrodynamic drift and the "pseudo electrostatic potential" (as defined by *Richmond et al.* [1980]) at 300 km for $\pm 65^\circ$ magnetic latitude, universal time, and day of the year. The model was constructed using data from incoherent radars located at Millstone Hill ($42.6^\circ N$, $288.5^\circ E$), St. Santin ($44.1^\circ N$, $2^\circ E$), Arecibo ($18.5^\circ N$, $293.2^\circ E$), and Jicamarca ($12^\circ S$, $283.1^\circ E$) for quiet magnetic conditions during solar minimum. These pseudopotentials are assumed to be essentially constant along the field lines. This final point is important to our study because it allows estimation of the electrodynamic drift velocities for heights other than 300 km.

The estimation process begins by assuming the electrodynamic drifts are constant between 200 km and 300 km because for field lines crossing the magnetic equator below 300 km, pseudopotentials cannot be extrapolated from model calculations. For points above 300 km, the electrodynamic drift velocities are calculated by assuming the magnetic field lines are equipotential and by using the equations for electrodynamic drift. These equations are

$$V_\perp = \frac{-1}{Br \sin \theta} \frac{\partial \Phi}{\partial \varphi} \quad (C1)$$

and

$$V_\varphi = \frac{-1}{Br \cos \theta} \left(\frac{\partial \Phi}{\partial \theta} \frac{1}{\cos I} + \frac{\partial \Phi}{\partial r} \frac{1}{\sin I} \right) \quad (C2)$$

where Φ is the pseudo electrostatic potential,

V_\perp is the vertical component of the electrodynamic drift,

V_φ is the azimuthal component of the electrodynamic drift,

I is the inclination angle,

θ is the colatitude, and

B is the magnetic field strength.

Equation (C1) is taken directly from *Richmond et al.*, [1980]; however, equation (C2) had to be modified to take into account the total electric field since $\frac{\partial \Phi}{\partial \theta}$ goes to zero at the magnetic equator [*Richmond*, 1988]. Using these assumptions, the variation of the pseudopotential with magnetic longitude, altitude, and colatitude can be determined; and since the field lines are assumed to be of constant potential, the variation of pseudopotential with longitude is also constant. Therefore, to calculate the vertical drift it only becomes necessary to find the magnetic latitude where the field line intersects 300 km to determine $\frac{\partial \Phi}{\partial \varphi}$ along the entire field line. Once this value is obtained, the vertical drift at any point along the field line can be calculated from equation (C1).

To obtain values for the eastward electrodynamic drift, the variation of pseudopotential with altitude and colatitude must be determined. Figure 24 shows a schematic of how the variation with colatitude can be estimated for any point, P, along the field line. The process begins by holding the radius constant and locating the field lines that lie $\pm \frac{\Delta\theta}{2}$ from point P. These points of intersection are indicated as points A and B in Figure 24. Once determined, the field lines are traced down to their points, C and D, of intersection with 300 km. Using the electric field model, the pseudopotentials at points C and D can next be determined and the variation in pseudopotential can be obtained by dividing the difference in pseudopotential by the chosen value for $\Delta\theta$. The variation of pseudopotential is determined in a like manner. The magnitude of the azimuthal drift is now computed from equation (C2). Since the magnitude of the electrodynamic drifts is a function of the magnetic field strength at any given point, B is calculated as a function of latitude, longitude, and altitude by the subroutine FIELDG described in Appendix B. Finally, although the model allows for various averages in universal time and season, none were used in our calculations.

Figure 25 shows the vertical electrodynamic drift at 300 km as a function of magnetic latitude and universal time for equinox and 0° magnetic longitude. For these conditions, the vertical drift is downward for virtually all magnetic latitudes from 0000 UT until 1000 UT, and is upward from 1000 UT to 1800 UT. After 1800 UT, the vertical drifts are upward within 10° of the equator and downward elsewhere. Upward drifts peak near 1500 UT with a velocity of 20 meters/second; the downward velocities peak near 0600 UT with a velocity of 16 meters/second.

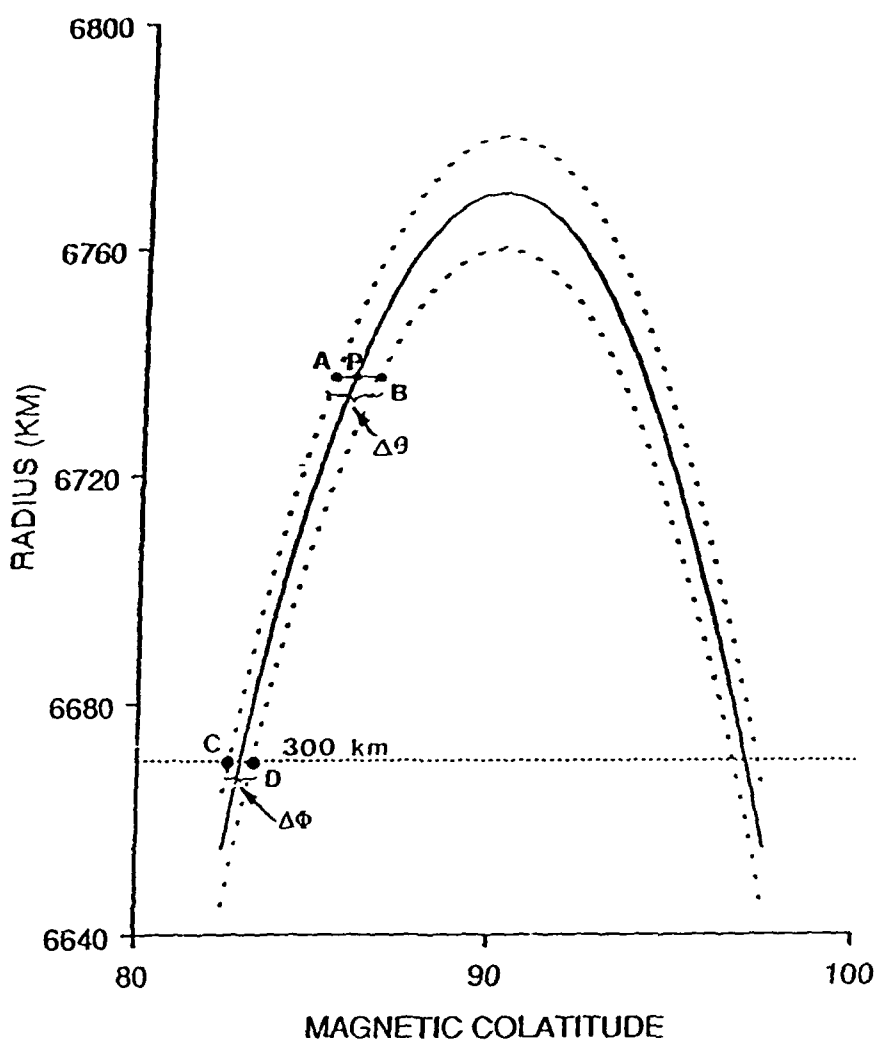


Figure 24. Schematic representation of how the variation of pseudopotential with colatitude is determined for any point, P, along the magnetic field line. $\Delta\theta$ is defined at point, P and $\Delta\Phi$ is calculated as the difference in the pseudopotentials given by the model at points, C and D.

Figure 26 is valid for the same conditions as Figure 25 except that the drifts are now for 1000 km. The pattern of drifts is essentially the same as for the 300 km case except that the magnitude has been reduced about 25%. This is to be expected owing to the method in which the variations with altitude are calculated. The method essentially brings the winds valid at 300 km for a given field line up to the altitude of the point in question and reduces them in an amount given by the variations of B and r .

Figure 27 is valid for June solstice at 300 km; all other conditions remain the

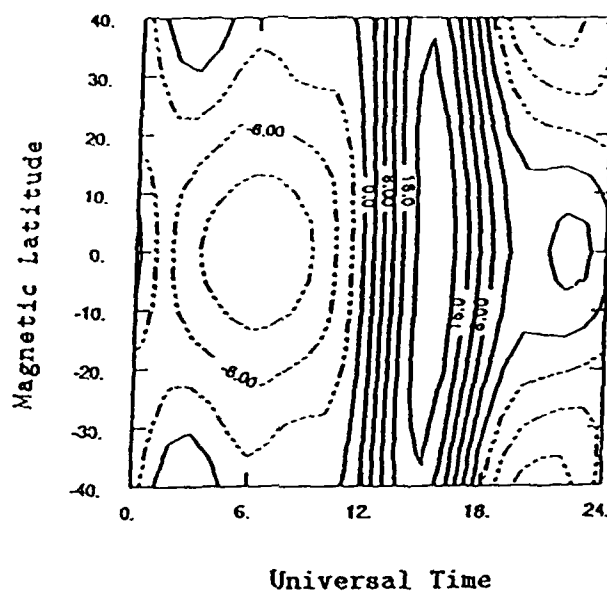


Figure 25. Vertical component of the electrodynamic winds in meters/second at 300 km for equinox and 0° magnetic longitude as a function of magnetic latitude and universal time. Contours intervals are 20 meters/second. Upward winds are defined to be positive.

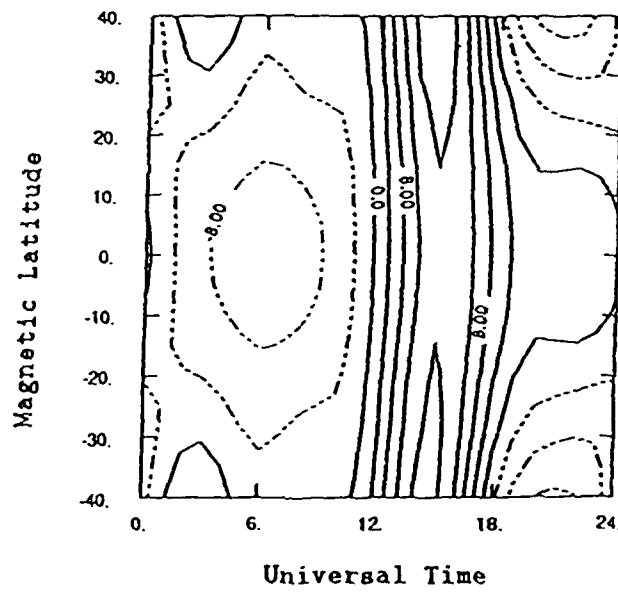


Figure 26. Vertical component of the electrodynamic winds in meters/second at 1000 km for equinox and 0° magnetic longitude as a function of magnetic latitude and universal time. Contours intervals are 20 meters/second. Upward winds are defined to be positive.

same. Peak drift velocities are somewhat reduced from the equinox case and an eastward bulge is introduced into the overall drift pattern. Near the magnetic equator, the drift is downward from 2300 UT until 1200 UT; but near $\pm 30^\circ$ magnetic latitude the drifts shift directions several times during the course of a day.

Figure 28 shows the vertical drift velocities for June solstice conditions at 1000 km. As in Figure 26, the pattern of drifts changes little with altitudes and the magnitudes of the drifts are reduced about 25%.

Even though of greater magnitude, azimuthal drifts are generally of much less importance and have been ignored in calculations of diffusion along magnetic field lines [Sterling *et al.*, 1969]. However, near sunrise and sunset horizontal variations in the ionosphere do become significant [Richmond, 1988] and the azimuthal component is, therefore, retained in this study.

Figure 29 shows the east-west component of the electrodynamic drift at 300 km for equinox and 0° magnetic longitude. Westward winds peak near 1600 UT at 50 meters/second. There is an eastward bulge in the wind pattern that is centered on the magnetic equator; perhaps, due to solar zenith angle effects.

Figure 30 is valid for the same conditions as Figure 29 except that the altitude is now 1000 km. As in the case of the vertical winds, the east-west winds essentially exhibit the same pattern at 300 km and 1000 km and the magnitude of the winds decrease 20 - 30% from 300 km to 1000 km. Peak winds at 1000 km are 60 meters/second in the eastward direction and 30 meters/second in the westward direction. Variations of the wind speed and direction with universal time are nearly the same as those at 300 km except as already noted.

Figure 31 shows the azimuthal component of the electrodynamic drift velocities at 300 km for June solstice and 0° magnetic longitude. For the solstice case, winds are predominantly eastward along this magnetic meridian and reach a peak of over 80 meters/second at 0200 UT. The drift is westward only between 1000 and 1800 UT. Peak westward winds are 40 meters/second and occur near 1500 UT.

Figure 32 is the same as Figure 31 except the winds are valid for 1000 km versus 300 km. Once again, windspeeds decrease 20 - 30% from 300 to 1000 km; and because of this decrease, westward drifts in excess of 20 meters/second are confined to a band of only 3 hours in universal time. At 1000 km, the peak

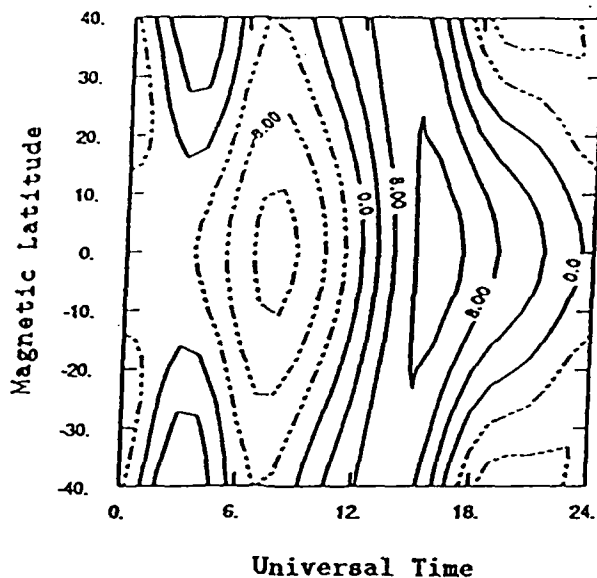


Figure 27. Vertical component of the electrodynamic winds in meters/second at 300 km for June solstice and 0° magnetic longitude as a function of magnetic latitude and universal time. Contours intervals are 20 meters/second. Upward winds are defined to be positive.

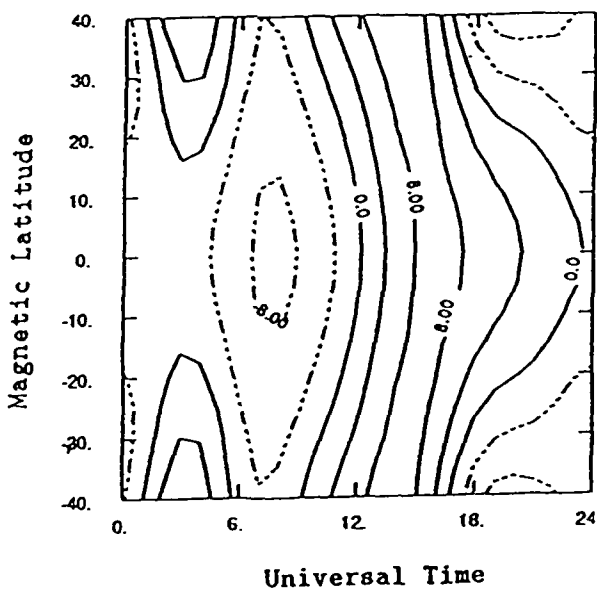


Figure 28. Vertical component of the electrodynamic winds in meters/second at 1000 km for June solstice and 0° magnetic longitude as a function of magnetic latitude and universal time. Contours intervals are 20 meters/second. Upward winds are defined to be positive.

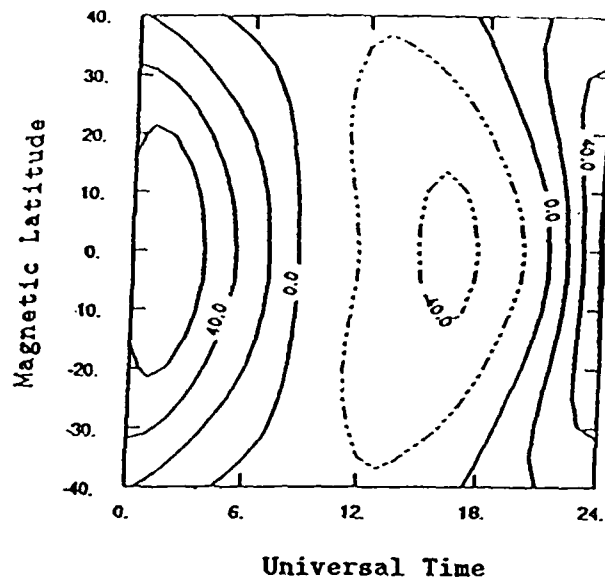


Figure 29. Azimuthal component of the electrodynamic winds in meters/second at 300 km for equinox and 0° magnetic longitude as a function of magnetic latitude and universal time. Contours intervals are 20 meters/second. Eastward winds are defined to be positive.

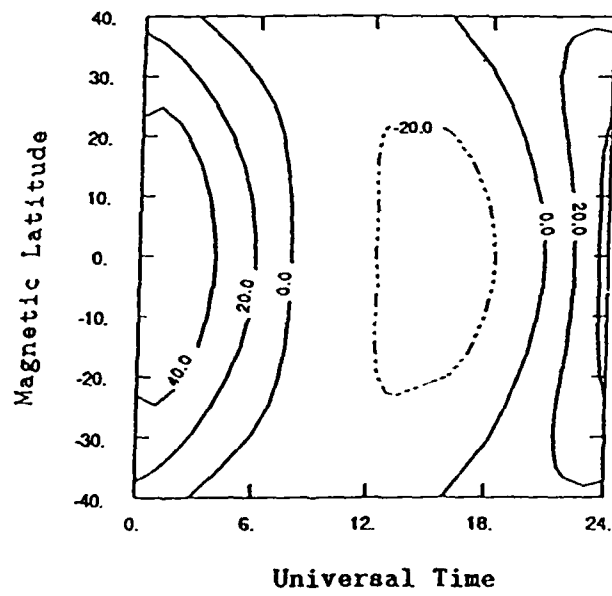


Figure 30. Azimuthal component of the electrodynamic winds in meters/second at 1000 km for equinox and 0° magnetic longitude as a function of magnetic latitude and universal time. Contours intervals are 20 meters/second. Eastward winds are defined to be positive.

westward winds only reach about 25 meters/second, whereas, the eastward drift exceeds 65 meters/second.

In summary, azimuthal wind speeds are considerably greater than the vertical drifts, but owing to the nearly horizontally homogeneous nature of the ionosphere throughout much of the day, they are generally less significant to the consideration of diffusion of ionospheric plasma along magnetic field lines. Upward vertical drifts tend to be greater for equinox than for June solstice, whereas, downward drifts vary little with season for the case considered. In the case of the azimuthal drifts, this pattern is reversed with the faster drifts occurring for solstice rather than equinox conditions. While winds are symmetric about the magnetic equator in all cases, the vertical drift component exhibits more latitudinal variation than the azimuthal component. Finally, it is worth noting again that the cases presented are meant to be representative of quiet magnetic conditions and low solar activity along the magnetic prime meridian.

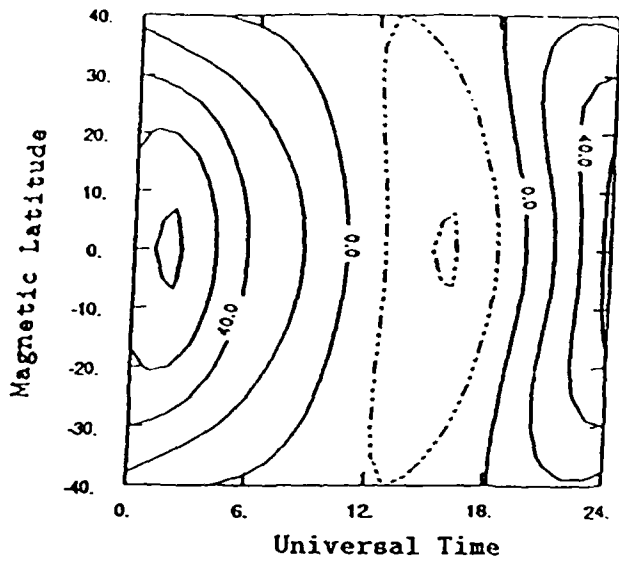


Figure 31. Azimuthal component of the electrodynamic winds in meters/second at 300 km for June solstice and 0° magnetic longitude as a function of magnetic latitude and universal time. Contours intervals are 20 meters/second. Eastward winds are defined to be positive.

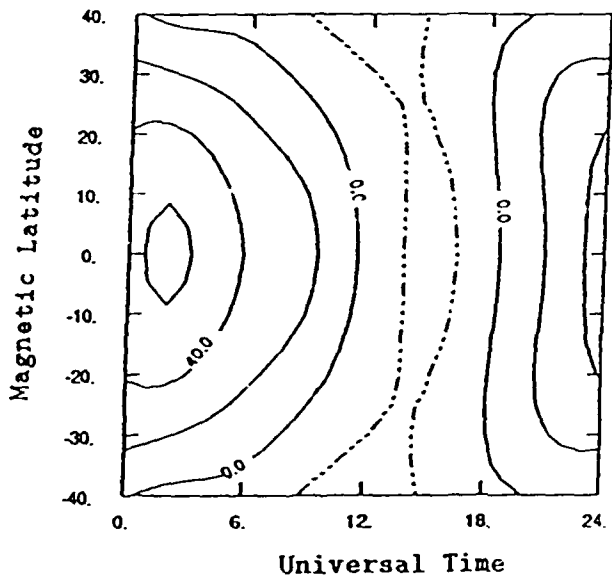


Figure 32. Azimuthal component of the electrodynamic winds in meters/second at 1000 km for June solstice and 0° magnetic longitude as a function of magnetic latitude and universal time. Contours intervals are 20 meters/second. Eastward winds are defined to be positive.

Appendix D: A Comparison of the IRI, Chiu, and SLIM Models

A prime motivation for the development of this model for the low-latitude, topside ionosphere was to improve current ionospheric modelling capabilities within the U.S. Air Force's Air Weather Service (AWS). Since the Semi-Empirical Low-Latitude Ionospheric Model (SLIM) [Anderson *et al.*, 1987] was being considered for incorporation into the Ionospheric Conductivity and Electron Density (ICED) model [Kroehl, 1987] and ICED is the primary operational model for specifying ionospheric parameters within the AWS, the SLIM approach was reviewed and its results were compared to other readily available empirical models and known ionospheric conditions.

For this comparison, two dip latitudes (0° and 14°N) and four local times (00, 06, 13, and 19 LT) were chosen as test cases. In the case of the IRI and Chiu models, the conversion subroutine included in IRI was used to convert these dip latitudes into geographic coordinates. Since there are no longitudinal variations in the SLIM [Anderson *et al.*, 1987] or Chiu [Chiu, 1975] models, the choice of 255°E was arbitrary. In addition, equinox and a sunspot number of 100 (moderate solar activity for SLIM) were used in the model calculations. Figures 33 – 36 show the results of this comparison. Each figure shows the electron density profile from 200 km to 1000 km as a function of local time and dip latitude. While a number of comparisons could be made using these figures, the one of primary interest was the radically different trends between IRI and SLIM that occur around 800 km. The SLIM profile shows an apparent exponential decrease in electron density with height above the peak in the F region; whereas, IRI shows an apparent exponential decrease and then a much less rapid decrease in electron density with height starting between 600 – 800 km. IRI has been found to underestimate daytime, total electron content (TEC) at low latitudes by as much as 50%, and SLIM, because it includes modelling of the vertical $\mathbf{E} \times \mathbf{B}$ drift, has produced significant improvements in TEC prediction. However, the SLIM model only computes O^+ densities [Anderson *et al.*, 1987], and H^+ can become a significant, if not the major, ion species by 1000 km. Since the AWS has requirements for modelling of the electron density at least up to 1000 km, development of a model which includes both ion species was undertaken to further improve ionospheric prediction for altitudes between 500 and 1000 km.

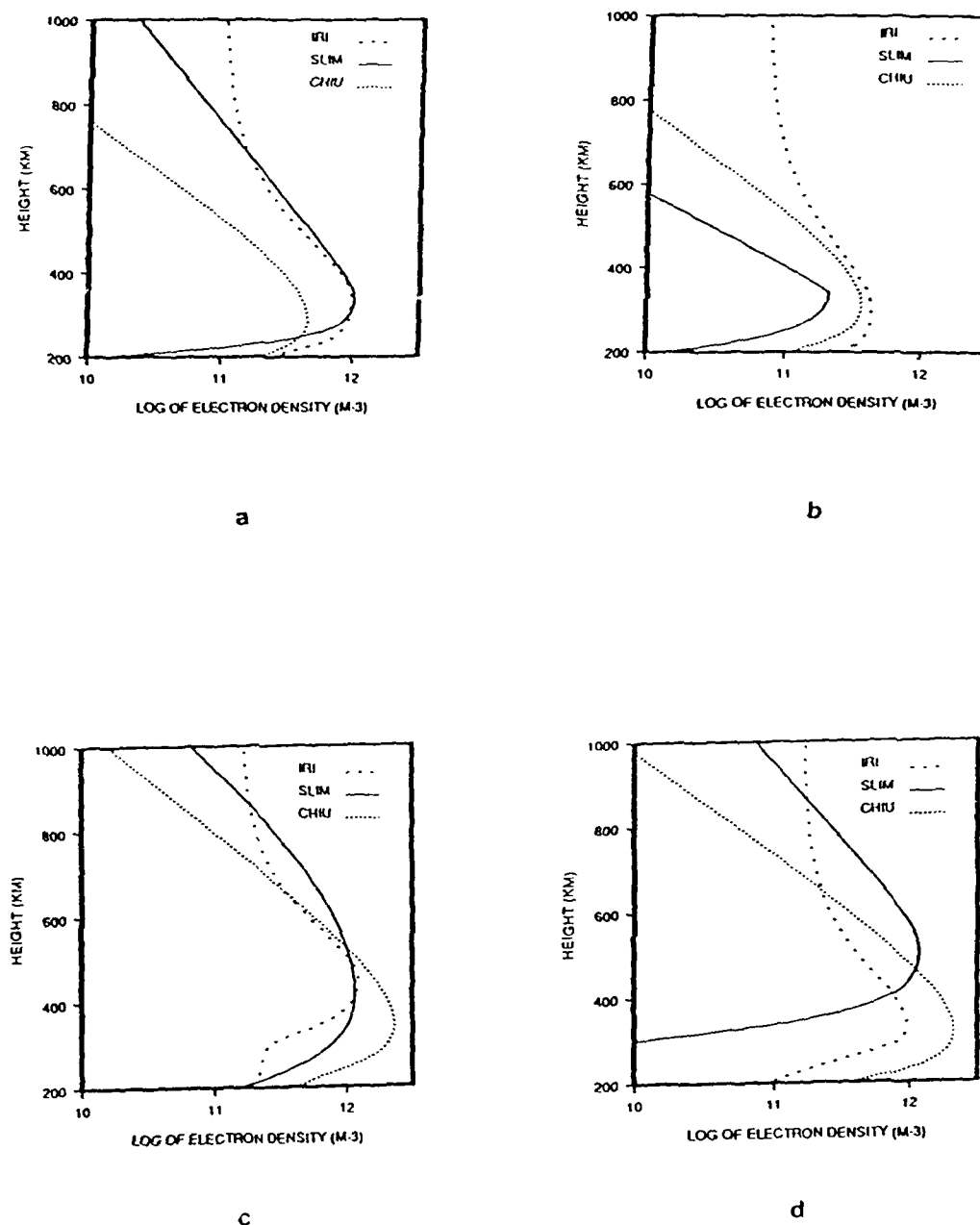


Figure 33. A comparison of electron density profiles produced by the SLIM, Chiu, and IRI empirical models for 0° dip latitude and 324° magnetic longitude for equinox and moderate solar activity. (a) 0000 LT (b) 0600 LT (c) 1300 LT (d) 1900 LT.

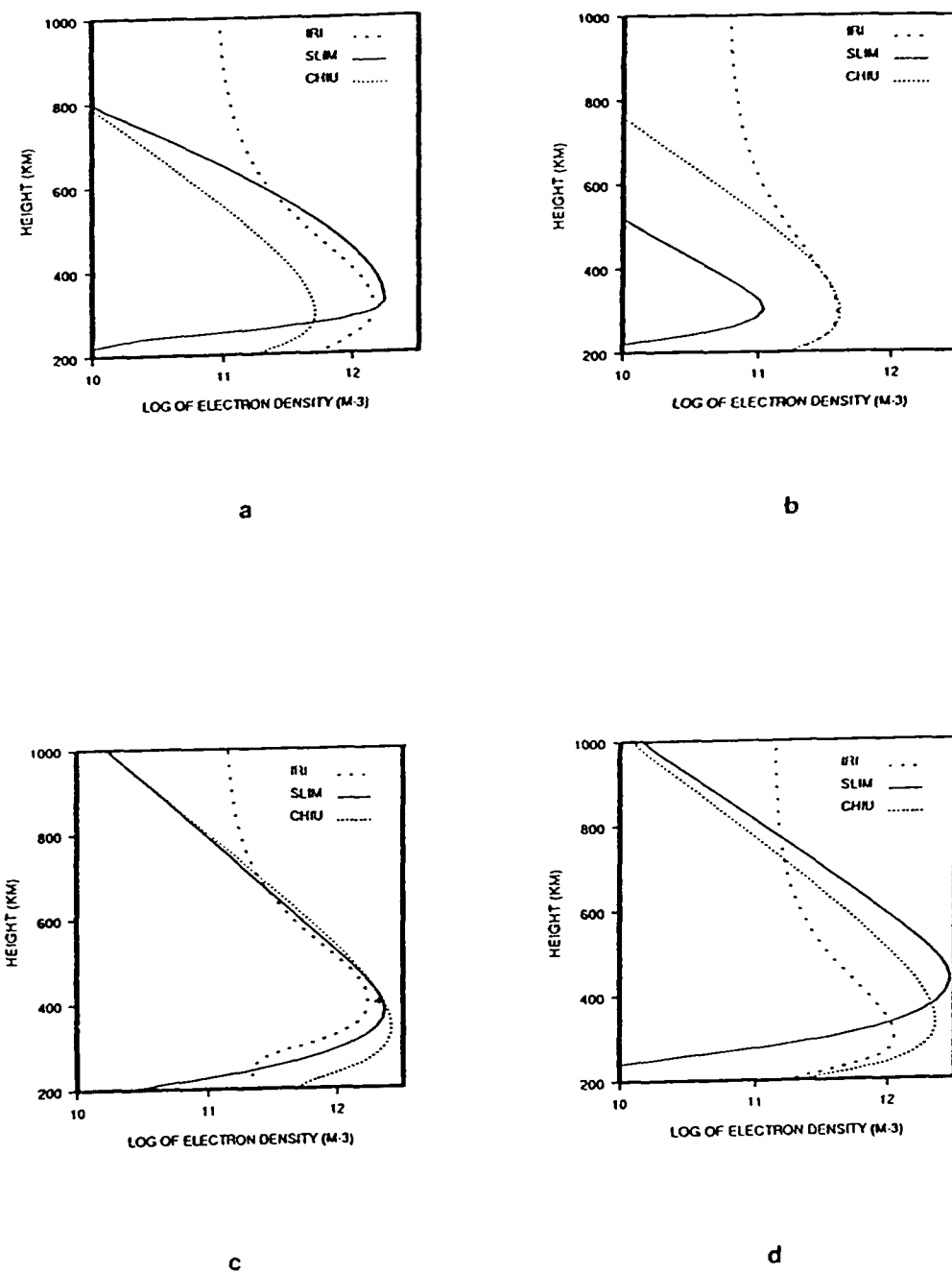


Figure 34. A comparison of electron density profiles produced by the SLIM, Chiu, and IRI empirical models for 14° dip latitude and 324° magnetic longitude for equinox and moderate solar activity. (a) 0000 LT (b) 0600 LT (c) 1300 LT (d) 1900 LT.

Appendix E: Permission Letters

May 2, 1988

Gary D. Wells
1235 E. 900 North
Logan, UT 84321
(801) 752-0792

D. Reidel Publishing Company
P.O. Box 17
3300 AA Dordrecht
HOLLAND

To Whom It May Concern:

I am in the process of preparing my thesis in the Soil Science and Biometeorology Department at Utah State University. I hope to complete all requirements by early June 1988.

I am requesting your permission to include the attached material as shown. I will include acknowledgements and/or appropriate citations to your work as shown and copyright and reprint rights information in a special appendix. The bibliographical citation will appear at the end of the manuscript as shown. Please advise me of any changes you require.

Please indicate your approval of this request by signing in the space provided, attaching any other form or instruction necessary to confirm permission. If you charge a reprint fee for use of your material, please indicate that as well. If you have any questions, please call me at the number above.

I hope you will be able to reply immediately. If you are not the copyright holder, please forward my request to the appropriate person or institution.

Thank you for your cooperation,

Gary D. Wells

I hereby give permission to Gary D. Wells to reprint the following material from *Solar-Terrestrial Physics* in his thesis.

Bibliographical Reference

Schunk, R.W., *The terrestrial ionosphere*, *Solar-Terrestrial Physics*, D. Reidel Publishing Company, 609-676, 1983.

Figures

- | | |
|-----------|----------|
| Figure 8 | page 617 |
| Figure 10 | page 618 |
| Figure 11 | page 619 |
| Figure 12 | page 619 |

(Fee)

(Signed)

ABSTRACT

Title of Thesis: Origin of Tropospheric Ozone over Central US

Donna P. McNamara, Master of Science, 1988

Thesis Directed by: Russell R. Dickerson
Associate Professor
Dept. of Meteorology

Aircraft data from two flights during June 1985, over Oklahoma and Arkansas, are analyzed to explain the observed concentrations of tropospheric ozone. Concurrent vertical profiles and time series of ozone with carbon monoxide, odd nitrogen and moisture are presented. Unique features on this day included pollutant concentrations typical of the planetary boundary layer extending to nearly 5 km altitude, a highly disturbed troposphere over a large area (about 500 km) immediately following passage of a squall line, and a sharp 100 ppb gradient in ozone in the upper troposphere remote from convection. Correlations between ozone and other trace gases are studied to determine if the elevated ozone came from stratospheric injection or tropospheric production. A simple photochemical model finds significant tropospheric ozone production possible under the conditions observed, suggesting that in summer over the Central US, tropospheric ozone production greatly contributes to the observed ozone concentrations.